REDOX INTERCALATION AND ELECTROCHEMICAL REACTIONS OF METAL-ORGANIC FRAMEWORKS AND A MIXED TRANSITION METAL OXIDE WITH APPLICATIONS IN LITHIUM AND MAGNESIUM BATTERIES

A Dissertation

Presented to

the Faculty of the Department of Chemistry

University of Houston

In Partial Fulfillment

of the Requirements for the Degree

Doctor of Philosophy

By

Watchareeya Kaveevivitchai

August 2014

REDOX INTERCALATION AND ELECTROCHEMICAL REACTIONS OF METAL-ORGANIC FRAMEWORKS AND A MIXED TRANSITION METAL OXIDE WITH APPLICATIONS IN LITHIUM AND MAGNESIUM BATTERIES

Watchareeya Kaveevivitchai

APPROVED:

Dr. Allan J. Jacobson, Chairman

Dr. Arnold M. Guloy

Dr. P. Shiv Halasyamani

Dr. T. Randall Lee

Dr. Haleh Ardebili

Dean, College of Natural Sciences and Mathematics

Acknowledgments

Over the past five years, I have received support and encouragement from a great number of individuals. I am greatly indebted to them and would like to sincerely acknowledge all those people who have been involved in this incredible journey. First and foremost, I would like to express my deep appreciation and gratitude to my doctoral advisor, Dr. Allan Jacobson, for imparting his knowledge and for the guidance and mentorship that he has provided to me, all the way from day one through to completion of this degree. His patience and enthusiasm have always been admirable, and I am truly fortunate to have had the opportunity to work with him. I am also very grateful to my dissertation committee members, Dr. Arnold Guloy, Dr. Shiv Halasyamani, Dr. Randall Lee, Dr. Angela Moeller, and Dr. Haleh Ardebili for the valuable and constructive suggestions. Their willingness to take time and effort to review my work has been very much appreciated.

I wish to express my appreciation to the past and present members of the Jacobson's research group. I would like to thank my mentor in crystallography, Dr. Xiqu Wang. He spent hours and hours teaching and helping me with the crystallographic work. I thank Tatyana (and Dr. Boris Makarenko) for their assistance with TGA and whatever else in the lab that I needed. Dr. Wenquan Gong who has taught and helped me on many occasions whenever I asked is also acknowledged. I thank the former students, Marlon Conato, who has answered my countless questions on research and graduate studies, Sang Ho Lee, who gave me fun lab experiences, and Paola Gil-Mateo for her kind heart,

together with the postdoctoral researchers, Qiang Gao, Susan Wang, and Chengfei Yu. I acknowledge the present members of the group, Sam (my great neighbor and benchmate), Dmitry, Julie, Kannika, and Parastou. My completion of this research could not have been accomplished without the support of Ellen Lee, our lab manager, who has always been there to provide us with whatever assistance that we need. I am deeply grateful to her.

I am indebted to several people who shared their valuable time and research expertise. I wish to express my great appreciation to Dr. Jim Meen (SEM), Dr. James Korp (XRD), Dr. David Hoffman and Ann Soriaga (glovebox), Dr. Steven Baldelli (laser), Dr. Ognjen Miljanić, Dr. Angela Moeller (PPMS), and Dr. Zhongjia Tang for providing valuable advice and assistance on solid state compounds. I also thank Dr. Arnold Guloy for giving me access to his facilities, and his student Sean for training and helping me with single crystals. I would like to offer my special thanks to Dr. Haleh Ardebili and Dr. Yan Yao for allowing me to learn and use their battery fabrication set-ups. Assistance provided by their lab members, Qin and Mejdi (Ardebili's group), as well as Len, Yan Jing, Yifei, and Jian (Yao's lab) was greatly appreciated. My grateful thanks are also extended to the staff in and out of the chemistry department, including, but not limited to, Mark (machine work), Mike (building management), Roger (glass work), Jerry (computer work), Ed (chemical orders), and Hans (electronics). I also cannot express enough thanks to my classmate, Teng-Hao Chen, who has helped me countlessly over the course of my graduate study.

My experience in Houston would have been less enjoyable without the hospitality of Saeng and Prasert Sananikone and their family. I owe them a great deal, especially with the assistance provided when I first moved to Houston.

Last, but definitely not least, my deepest gratitude goes to my parents, Weerachai and Jintana, my aunt Jarinee, and my big brother Nattawut, who have always been there for me every step of the way, not only for this final degree, but since the beginning of my education. I am gratefully indebted for their unwavering support and encouragement over the years. This dissertation is dedicated to them.

REDOX INTERCALATION AND ELECTROCHEMICAL REACTIONS OF METAL-ORGANIC FRAMEWORKS AND A MIXED TRANSITION METAL OXIDE WITH APPLICATIONS IN LITHIUM AND MAGNESIUM BATTERIES

An Abstract of a Dissertation

Presented to

the Faculty of the Department of Chemistry

University of Houston

In Partial Fulfillment

of the Requirements for the Degree

Doctor of Philosophy

By

Watchareeya Kaveevivitchai

August 2014

Abstract

This dissertation focuses on the redox properties of metal-organic frameworks and a microporous mixed transition metal oxide. The study is divided into two main areas: an intercalation of a redox active molecular guest into host single crystals, and an intercalation of reactive alkali and alkaline earth metals, Li and Mg, by solid state electrochemical reactions into the microporous compounds with applications in lithium and magnesium rechargeable batteries.

A metal-organic framework $[V^{IV}(O)(bdc)](H_2bdc)_{0.71}$ (**1**) was synthesized. This solid was activated to remove the guest molecules, and an empty framework of $[V^{IV}(O)(bdc)]$ (**2**) was obtained. **2** was used as a host to undergo a vapor-phase redox intercalation of an electroactive organic guest, hydroquinone. In ambient atmosphere, $[V^{III}(OH)(bdc)]\cdot\{(O\text{-}C_6H_4\text{-}O)(HO\text{-}C_6H_4\text{-}OH)\}_{0.76}\cdot(H_2O)_{0.48}$ (**3**) was formed, whereas under anhydrous conditions, the product was $[V^{III}(O\text{-}C_6H_4\text{-}O)(bdc)]$ (**4**). Structural deformations as a function of temperature of **2** and **4** were also studied.

$[V^{IV}(O)(bdc)]$ (**2**) was used in solid state electrochemical reaction with lithium. The Li cells with **2** as the cathode material were reversibly cycled with good rate capability and specific capacity. The cell performance and electrochemical profiles at various current conditions were discussed. Structural evolution associated with the electrochemical lithiation was characterized.

A metal-organic framework, $[NH_2(CH_3)_2][Fe^{III}Fe^{II}(HCOO)_6]$ (**FeFOR**), was used as cathode in secondary lithium batteries. The electrochemical profiles suggested that **FeFOR** reacted reversibly with Li. The mechanism involved in the electrochemical reaction was proposed to be intercalation-based and conversion-based with LiHCOO being the matrix involved.

A microporous molybdenum-vanadium oxide with large open 1D channels, $Mo_{2.5+y}VO_{9+\delta}$, was used as an intercalation positive electrode material in lithium batteries. The electrochemical profiles showed good specific capacity at high current densities. The cells were found to be reversible even without conducting additives. The structural changes taking place during Li-ion insertion were described, and the chemical deintercalation of lithium was also performed to demonstrate the reversibility.

$Mo_{2.5+y}VO_{9+\delta}$ was found to reversibly undergo not only lithium insertion in Li-based batteries, but also magnesium intercalation. The compound was used as cathode material, and reversibly cycled with magnesium as the counter electrode with good specific capacity. The effect of varying current densities on the discharge profiles was included.

Table of Contents

List of Figures

List of Schemes

List of Tables

List of Abbreviations and Acronyms

4,4′-bpy	4,4′-bipyridine
bdc	1,4-benzenedicarboxylate
DMC	dimethyl carbonate
dmf	dimethylformamide
EC	ethylene carbonate
EPR	electron paramagnetic resonance
EVs	electric vehicles
HEVs	hybrid electric vehicles
HOMO	highest occupied molecular orbital
IR	infrared
LIBs	Li-ion batteries
LUMO	lowest unoccupied molecular orbital
MOFs	metal-organic frameworks
NMP	N-methyl-2-pyrrolidinone
PBAs	Prussian blue analogs
PHEVs	plug-in hybrid electric vehicles
PVdF	polyvinylidene fluoride
PXRD	powder X-ray diffraction
py	pyridine
SEM	scanning electron microscopy

SHE	standard hydrogen electrode
tfbdc	2,3,5,6-tetrafluoroterephthalate
TGA	thermogravimetric analysis
THF	tetrahydrofuran
TM	transition metal
TTF-TC	tetrathiafulvalene tetracarboxylate

List of Symbols

C	number of components
D	gravimetric or volumetric energy density
E	voltage of the cell or electromotive force (emf)
E_g	energy difference between HOMO and LUMO
F	(a) the Faraday's constant
	(b) number of degrees of freedom
ΔG	Gibbs free energy change
I	current
m	number of moles of electrons which is equal to number of moles of cation species (Li^+)
n	number of electrons transferred per mole of reactants
P	number of phases present
Q	(a) amount of charge
	(b) capacity
t	time
V	average cell potential
V_{oc}	open circuit voltage or voltage at equilibrium
x	number of electroactive species per formula unit
μ_A	electrochemical potential of an anode
μ_C	electrochemical potential of a cathode

$\mu_{Li(A)}$	lithium chemical potential in an anode
$\mu_{Li(C)}$	lithium chemical potential in a cathode

Chapter 1

Introduction

1.1 Objectives of the Study

The general objective of this research is to investigate the redox properties of metal-organic hybrid frameworks and mixed transition metal oxides (in particular, porous compounds) based on transition metals, namely, vanadium, iron, and molybdenum. This study focuses on the redox intercalation of a redox active guest and the electrochemical reactions of lithium and magnesium with the compounds. The main characterization technique used is structure identification by X-ray crystallography, and the electrochemical studies were performed using galvanostatic and potentiostatic techniques.

1.2 Background of the Study

Among the numerous properties which can be possessed by solid compounds, the redox (defined as being involved with electron transfer) and electrical properties have received significant attention over the years due to their practical applications in our everyday lives. For example, redox activities of solids help enhance electronic conductivity, and redox active compounds can be used as electrodes for lithium-ion batteries, fuel cells, and capacitors.[1–27] This is evident from the several excellent review articles over the last five years.[3,4,20,21,28–33] This research is focused on porous materials, namely, metal-organic frameworks (MOFs) and microporous mixed transition metal

oxides. More details on MOFs which form a relatively new class of materials are given below.

1.2.1 Metal-Organic Frameworks

A fascinating group of porous crystalline materials, metal-organic frameworks (MOFs) or sometimes referred to as coordination polymers, has attracted tremendous attention in the past two decades.[34–40] MOFs have extended connectivity with backbones assembled from inorganic building units (metal ions or clusters) as 'nodes' and organic polydentate ligands as 'linkers'. The various combinations of the two primary building components allow the formation of the structures with different dimensionalities, such as 1D chains, 2D layers, and 3D frameworks.[41,42] Due to their structural novelty, high surface areas, and the design and synthesis flexibility inherent in MOFs, many efforts have been made to address technological applications using these materials in categories, such as gas storage, selective molecular adsorption, separations, ion exchange, catalysis, magnetic and photoluminescence responses, optoelectronics, and drug delivery.[37,43–45] A large number of MOFs are known to be sufficiently robust even after the removal of solvent molecules or organic templates from the channels, resulting in framework structures with high porosity.[34,36] To take advantage of MOF porous character, one way is to control the chemical nature of the pores by the use of post-synthetic modification.[46] The ability to store a desired compound is a typical property of porous materials. The physical and chemical properties of MOFs can be fine-tuned by incorporating or intercalating functional guest molecules inside the pores of the network (Figure 1.1).[47]

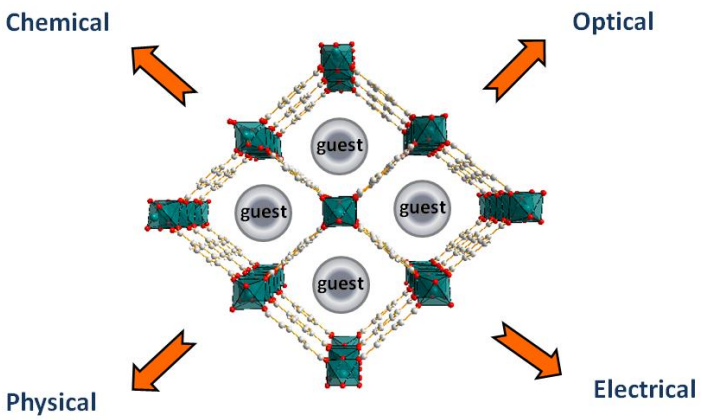

Figure 1.1 Schematic representation of fine-tuning MOF properties by intercalating functional guest molecules inside the pores.

1.2.2 Intercalation Chemistry

Intercalation or insertion compounds are solids made of host and guest species. The host provides a lattice or framework, while the guests occupy sites within the framework. Therefore, intercalation is the process of inserting a guest atom/molecule/species (or ion with its charge compensating electrons) into normally unoccupied sites in the crystal structure of an existing stable host solid. Reactions of this type are most likely to occur when the host has an open framework or a layered type of crystal structure, so that there is space available for the presence of additional small species. Though the chemical composition of the host phase initially present can be substantially changed, this reaction does not lead to a change in its identity or of the basic crystal structure. In most cases, the addition of species to previously unoccupied locations in the structure causes a change in volume. As a consequence, the chemical or physical

properties of the intercalated guest species directly affect the overall properties of the resulting intercalation compounds.[48]

These properties have gained great technological interest, and are exploited when intercalation compounds are used as electrodes in electrochemical cells. In terms of solid state electrochemistry, two properties distinguish intercalation compounds from other solids: (1) the guests are mobile (moving between sites in the host lattice); (2) the guests can be added to the host or removed from it, so the concentration of the guests can change. Reactions where the chemical composition of an existing phase is changed by the incorporation of guest species can also be thought of as the solution of the guest into the host material. Such processes are also sometimes referred to as *solid solution reactions*. At the positive electrode, reversibility is a consequence of the use of an insertion electrode material, which can incorporate the electroactive species into a solid solution phase with a wide stoichiometric range of composition. The electrode undergoes a reversible topotactic redox reaction; that is, the electrode material acts as a host structure which accommodates guest ions and electrons without destruction of the lattice. Guest species tend to be present at specific (low energy) locations inside the crystal structure of the host species, and not randomly distributed. This involves mechanical stress and mechanical energy of the crystal lattice. The energy related to insertion and extraction of guest species plays a significant role in the hysteresis, and subsequent energy loss, observed in a number of reversible battery electrode reactions. An example is the insertion of Li between layers of graphite, which is the process used as the anode in

today's Li-ion batteries. This particular insertion process was developed as a replacement for lithium metal anodes in rechargeable lithium batteries.[49–55]

There are several types of insertion reactions. In one type, the mobile guest species randomly occupy sites within all the pores and channels of the host. As the guest concentration increases, the species gradually fill up all the available space. When this happens, the variation of the electrochemical potential with composition indicates a single-phase solid solution reaction. On the other hand, if there are two or more types of available sites in the lattice with different energies, the guest species can occupy an ordered array of sites, rather than all of them. If this is the case, changes in the overall concentration of mobile species require the translation of the interface separating the occupied regions from those that are not occupied. This phenomenon where selective occupation of particular sites in an ordered fashion is involved, especially in a material with a layered crystal structure, is described as "staging".[48,50,51]

1.2.3 Definitions[51,52,56,57]

Battery: one or more electrically connected electrochemical cells.

Primary battery: a cell or group of cells intended to be used and then discarded when the energy stored is exhausted. Primary batteries are assembled in the charged state and discharge is the primary process during battery operation.

Secondary battery: a cell or group of cells for generating energy where the cell, after discharge, can be restored to its original charged state by an electric current flowing

in the direction opposite to the flow of current when the cell was discharged. A secondary battery is also known as a *rechargeable battery*. A secondary battery is usually assembled in the discharged state, and it has to be charged before undergoing discharge which is a secondary process.

Discharge: an operation where a battery gives useful electrical energy to an external load.

Charge: an operation where a battery is restored to its original charged state by applying an external potential to reverse the current flow.

Anode: the negative electrode of an electrochemical cell at which oxidation reactions occur and release electrons into the external circuit.

Cathode: the positive electrode of an electrochemical cell at which reduction reactions occur and accept electrons from the external circuit.

Active material: the material that generates electrical energy by a chemical reaction inside a battery.

Electrolyte: a material that provides pure ionic conductivity between the anode and the cathode, but not electronic conductivity.

Separator: a physical barrier between the positive and negative electrodes which prevents electrical shorting. An example of a separator is microporous polymer film or other porous materials filled with electrolyte. Separators must be permeable to the ions and chemically inert to other components in the battery environment.

Open circuit voltage: the voltage across the positive and negative terminals of a cell when there is no external current flow. It is the thermodynamic voltage for the system.

Closed circuit voltage: the voltage of a cell or battery when there is current flow and the battery is producing current into the external circuit.

Faraday's constant, F: the amount of charge that transfers when one equivalent of active material reacts or the amount of electric charge per mole of electrons, which is equal to 96500 coulombs per mole (C/mol).

1.2.4 Battery Design

In batteries, electrical energy is generated by conversion of chemical energy via redox reactions at the anode and cathode. Because reactions at the anode usually occur at lower potentials than at the cathode, the terms negative and positive electrode (indicated as minus and plus poles) are used. The more negative electrode is designated the anode, and the more positive one is the cathode.[51,52] Batteries are closed systems, with the anode and cathode taking an active role in the redox reactions as "active materials". That is, energy storage and conversion occur in the same compartment. In contrast, in fuel cells which are open systems, the anode and cathode are charge-transfer media and the active materials undergoing the redox reaction are delivered from outside the cell.[52]

A schematic diagram of a single cell of a rechargeable lithium battery is shown in Figure 1.2. Each cell consists of a cathode (oxidant) and an anode (reductant), separated

by an electronic insulator (the separator), but they are in electrical contact through a conductor of positive ions that is also electronic insulator (the electrolyte).[58] The chemical reaction between the two electrodes has two components, namely, positively charged ions and negatively charged electrons, which during discharge, pass from the anode to the cathode where they neutralize one another. The electrolyte enables the transfer of the positive ions, but the electrons are forced to pass through the external circuit with a release of energy to be tapped by the user.[52,59] Collection of the electrons from the anode to a negative post for delivery to the external circuit and their delivery to the cathode from a positive post during discharge is performed by metallic conductors (the current collectors).[60] When the battery is charged, the load is replaced with an energy source that imposes a reverse voltage larger than the open circuit voltage of the cell. The opposite reaction occurs and the flow of electrons is reversed.[61,62]

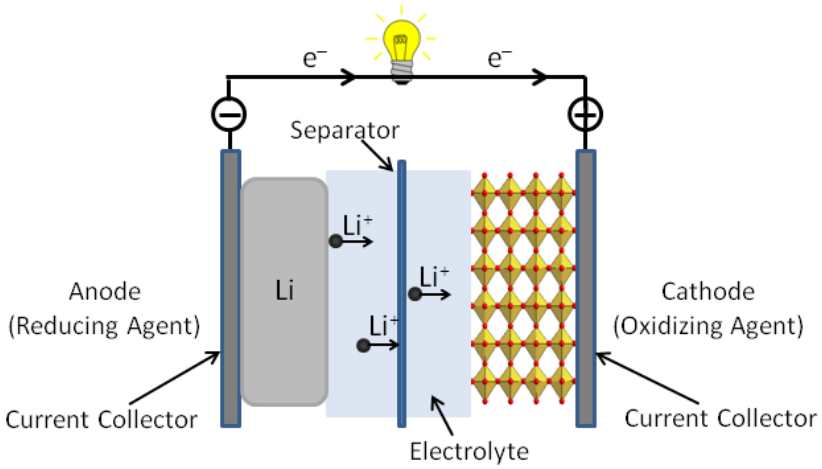

Figure 1.2 Schematic representation of a rechargeable lithium battery after reference 91.

1.2.5 Thermodynamics

The electrochemical energy storage systems directly follow the thermodynamic and kinetic formulations for chemical reactions.[51] Because ΔG represents the net useful energy available from a given reaction, in electrochemical terms, the net available electrical energy from a reaction in a cell is given by

$$\Delta G = -nFE \tag{1.1}$$

where ΔG is the change in Gibbs free energy or the energy of a reaction available (= free) for useful work. For the material in the standard state (25 °C and unit activity),

$$\Delta G^\circ = -nFE^\circ \tag{1.2}$$

where n is the number of electrons transferred per mole of reactants, F is the Faraday's constant (equal to the charge per 1 mole of electrons), and E is the voltage of the cell; in other words, E is the electromotive force (emf) of the cell reaction. The voltage of the cell is unique for the specific chemical reaction. The amount of electricity produced, nF, is determined by the total amount of materials available for reaction. Spontaneous processes have a negative free energy and a positive emf. The potential difference created by the reaction couple drives current flow when the cell is in closed circuit.[51,52,57]

The free energy change associated with the transfer of electrons between the cathode and the anode is equivalent to the difference in the chemical potential of the two electrodes,

$$V_{oc} = (\mu_A - \mu_C)/(-nF) \tag{1.3}$$

where V_{oc} is the open circuit voltage of the cell, $\mu_A - \mu_C$ is the difference in the electrochemical potential of the anode and the cathode, n is the number of electrons involved in the chemical reaction of the cell, and F is the Faraday's constant.[62–65]

The amount of electrical energy, expressed either per unit weight or per unit volume, that a battery is able to deliver is a function of the average cell potential and capacity (both of which are linked directly to the chemistry of the system), and can be expressed as

$$D = VQ \tag{1.4}$$

where D is the gravimetric or volumetric energy density, V is the average cell potential (V), and Q is the charge stored per unit mass or volume of the compound or capacity, conventionally expressed in terms of Ah/kg or Ah/L (or more commonly mAh/g).[51,65]

The "gravimetric" (per kilogram) or "volumetric" (per liter) energy density is used to compare the energy contents of a system and is also referred to as "specific energy" expressed in watt-hours per kilogram (Wh/kg) and "energy density" in watt-hours per liter (Wh/L), whereas the rate capability is expressed as "specific power" (in W/kg) and "power density" (in W/L). These terms are used to determine the period of useful use before recharge is required. An expected lifetime of a battery is usually defined in terms of the cycle number, i.e., the total number of charge-discharge cycles which may be obtained before a significant degradation occurs in the energy and power values.[52,66]

For lithium batteries, the cathode is usually composed of an intercalation compound, such as a transition metal oxide, while the anode is lithium metal.[51] The motivation for using a battery technology based on Li metal as anode is based on the fact that Li is the most electropositive (–3.04 V vs SHE) as well as the lightest (atomic weight = 6.94 g/mol and density = 0.53 g/cm^3) metal, thus facilitating the design of storage systems with high energy density. The combination of these two characteristics gives the element a particularly favorable energy content.[67–69]

On discharge, Li is transferred from a state of high lithium chemical potential (high energy), $\mu_{Li(A)}$, in the negative electrode to that of low lithium chemical potential (low energy), $\mu_{Li(C)}$, in the positive electrode. This electrochemical insertion reaction also referred to as solid state redox reaction involves insertion of mobile guest ions (in this case Li^+ ions) from an electrolyte into the structure of a solid intercalation compound, coupled with charge-transfer (their charge-compensating electrons; lithium donates its outer s electron to the host's electronic energy levels).[50] On inserting electrons into an intercalation host, they will enter at the Fermi level which is set by the position of the d-levels of the transition metal ions.[70] In a transition metal oxide, Li^+ ions occupy sites surrounded by negative oxygen ions, and distance themselves as far as possible from the positive transition metal ions. Since Li^+ has a filled outer core of electrons, the geometry of the site is not important as long as the anions are distributed evenly around the site. For example, Li^+ surrounded by four anions would prefer the anions to form a tetrahedron rather than a square. Compounds made by insertion at room temperature are usually metastable. If heated, they change their structure or decompose into other compounds.[51,59]

A prerequisite for a good insertion cathode is mixed electronic and ionic conductor. Ionic conductivity occurs by means of ions hopping from site to site through a crystal structure. However, in materials with poor electronic conductivity, good battery operation is possible. In this case, highly conductive additives, such as carbon are incorporated in the electrode mixture, and small host particles must be electronically connected to the current collector by being embedded in a Li-permeable conductive matrix. The insertion compound should also have a high electrochemical potential to maximize the cell voltage. This implies that the transition metal ion M^{n+} should have a high oxidation state.[63,71–77]

The stored energy content of a battery can be maximized by having a large chemical potential difference between the two electrodes, by making the mass (or volume) of the reactants per exchanged electron as small as possible, and by ensuring that the electrolyte is not consumed in the chemistry of the battery.[52]

A thermodynamically stable cell has the electrochemical potentials, μ_A of the anode and μ_C of the cathode within the electrolyte "window" (Figure 1.3). The window, E_g, of a liquid electrolyte is the energy difference between its lowest unoccupied and highest occupied molecular orbitals, its LUMO and HOMO (in the case of a solid electrolyte, it is the energy gap between the conduction and valence bands). If μ_A is above the LUMO, the electrolyte is reduced by electrons from the anode and if μ_C is below the HOMO, the electrolyte is oxidized by transferring electrons to the cathode.[65,78,79]

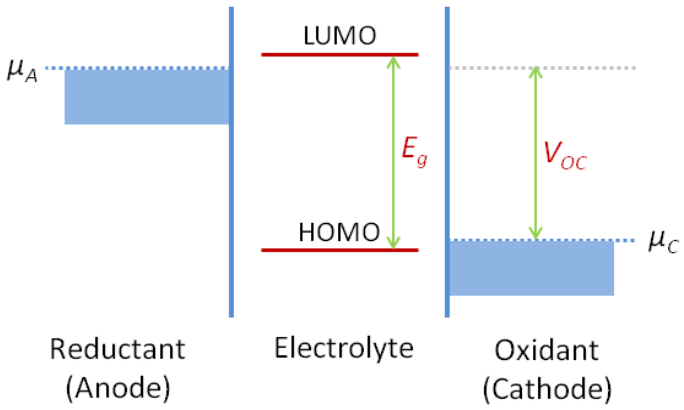

Figure 1.3 Schematic energy diagram of the electrolyte window E_g and the electrode electrochemical potentials μ_A and μ_C of liquid electrolyte with solid electrodes after references 64 and 65.

Generally, battery electrolytes can be categorized into aqueous, non-aqueous, and solid electrolytes. Aqueous electrolytes are commonly salts of strong acids and bases, and are completely dissociated into positive and negative ions in solution. The electrolyte provides an ionic conduction path as well as a physical barrier between the positive and negative electrodes. In aqueous systems, conductivities of the order of 1 S/cm are common. The high conductivity of aqueous solvent-based electrolytes is due to their dielectric constants, which favor stable ionic species, and the high solvating power.[52] In the non-aqueous organic solvent-based systems used in lithium batteries, most organic solvents have a lower solvating power and a lower dielectric constant. This favors ion pair formation, even at low salt concentration. Ion pair formation lowers the conductivity as the ions are no longer free and bind to each other. However, in some solvents, such as organic liquid carbonates or ethers, it is known that separation of Li^+ from a lithium salt

is sufficient to give a Li^+ conductivity in the order of 10^{-2}–10^{-3} S/cm which is adequate for battery operation.[52,63] Each electrolyte is stable only within certain voltage ranges. Organic solvent-based electrolytes with the help of kinetics are limited to ~4.6 V. Exceeding the electrochemical stability window in the organic electrolytes leads to polymerization or decomposition of the solvent system.[80,81]

1.2.6 Kinetics

Thermodynamics describe reactions at equilibrium and the maximum energy release for a given reaction. Apart from the voltage at equilibrium (or open circuit voltage, V_{oc}), when current is drawn from the battery, the voltage drops off (= electrode polarization or overvoltage) must occur to produce current flow during operation due to kinetic limitations.[52] Electrochemical reaction kinetics follow the same general considerations as those for bulk chemical reactions.[51] However, electrode kinetics differ from bulk reaction kinetics in two aspects: the influence of the potential drop in the electrical double layer at an electrode interface, and the fact that reactions at electrode interfaces proceed in a two-dimensional, not three-dimensional manner.[57] The mechanism of battery electrode reactions involves a series of physical, chemical, and electrochemical steps. The rates of these individual steps determine the kinetics of the electrode and the battery. Basically, three different kinetic effects for polarization (or overvoltage)[51,52,57] have to be considered:

Activation polarization is related to the kinetic hindrances of the electrochemical redox or charge-transfer reactions taking place at the electrode/electrolyte interfaces of the anode and cathode.[51,52]

Ohmic polarization (IR drop) arises from the resistance of individual cell components and from the resistance due to contact problems between the cell components (the electrolyte, the conductive diluents, materials of construction of the electrodes, current collectors, and terminals) as well as contact between particles of the active materials and conductive diluents, or from a resistive film on the surface of the electrode. Ohmic polarization appears and disappears instantaneously ($\leq 10^{-6}$ s) when current flows and ceases.[52,57]

Concentration polarization is due to mass transport limitations during cell operation, caused by the temporary loss in cell potential due to the difference between the surface and the average compositions of the electrodes. As the redox reactions proceed, the availability of the active species at the electrode/electrolyte interface changes. This results from, for example, limited diffusion of active species to and from the electrode surface to replace the reacted material to sustain the reaction. Diffusion limitations are relatively slow, and the buildup and decay take $\geq 10^{-2}$ s to appear.[52] Problems due to concentration gradients within the electrode particles can be alleviated by reducing the particle size.[51,57]

Most battery electrodes are a complex composite of powders composed of small solid particles of active material, a conductive diluent (usually carbon), and a polymer

binder to hold the mixture together and bond to a conductive current collector.[82–84] Typically, a composite battery electrode has ~30% porosity.[52] This yields a much greater available surface area for reaction than the geometric area, shortens the lengths of diffusion path to the reaction sites, lowers current density, and lowers polarization. The pores of the electrode structures are filled with electrolyte. In practice, the influence of the current on the cell voltage is controlled by all three types of polarization.[85–90]

These kinetic limitations lead to the difference between the theoretical and practical energy storage capabilities of batteries, namely, internal resistances within the electrodes and electrolyte, and between other cell components, resulting in internal losses. Moreover, limited utilization of the active materials, for example, passivation of electrodes making them (partially) electrochemically inactive, and inert parts of the system, such as conductive diluents, current collectors, and battery cases/containers, are responsible for the energy storage capabilities.[52,63,91]

1.2.7 The Gibbs Phase Rule

To understand how the voltage across an electrochemical cell varies with the state of charge, the Gibbs Phase Rule is used to describe the shape of the discharge curves and to consider the phase equilibria in connection with the variation of the electrical potential of electrodes with their composition.[51] The *Gibbs Phase Rule* is written as

$$F = C - P + 2 \tag{1.5}$$

where *C* is the number of components (e.g., elements), *P* is the number of phases present in the system, and *F* is the number of degrees of freedom, which is the number of intensive thermodynamic parameters (their values are independent of the amount of material present) that must be specified in order to define the system and all of the electrical and chemical properties associated. In this context, the most useful thermodynamic parameters are temperature, pressure, and electrical potential (chemical potential).[51,52] To illustrate the concept of the Gibbs Phase Rule, an example of the insertion reaction in a Li/V_2O_5 cell is given. Figure 1.4 shows a discharge curve of a Li/V_2O_5 cell.

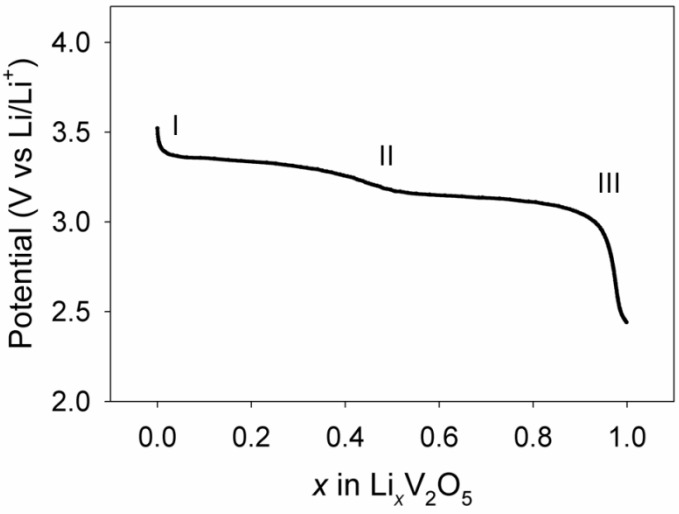

Figure 1.4 Variation of the potential as a function of lithium concentration in $Li_xV_2O_5$.

Starting at the open circuit voltage of ~3.5 V, ~0.1 Li per mole is inserted into the host V_2O_5 phase as a solid solution reaction. The number of components *C* is thus equal to 2. Since in a solid solution, there is only one phase present (phase I in Figure 1.4); therefore, $P = 1$, and *F* is equal to 3. This means that if values of two intensive thermodynamic parameters, such as temperature and pressure, are specified, there is a residual value of *F*, i.e., one. Thus the electrical potential of the system can be a variable and changes during discharge as a function of other parameters, e.g., the amount of lithium in the solid solution.[51,52] As a result, $0 < x < 0.1$ is a single-phase solid solution corresponding to a sloping voltage region.

The introduction of additional lithium ($0.1 < x < 0.35$) causes nucleation and growth of a second phase. When more than 0.1 Li is added, a reconstruction (also known as reconstitution) reaction takes place. This reaction involves two regions within the material with different Li contents. As the reaction proceeds the compositions of the two phases do not change, but the relative amount of the phase with the higher Li content increases, and that of the initial solid solution phase is reduced.[50] This occurs through the movement of the interface between them.[51] In this binary system with one mobile species inside a host structure, $C = 2$ and there are two phases present, thus $P = 2$; the value of *F* is 2. If the temperature and pressure are specified, then there is no degree of freedom left and other parameters of the system, such as voltage, have to be constant.[51,52] Hence, the cell voltage stays constant (voltage plateau) for the two-phase region ($0.1 < x < 0.35$) where phase I and II coexist in equilibrium. The same concept also applies to phase III in Figure 1.4.

1.2.8 Electrochemical Techniques

Electrochemical techniques are based on the fact that galvanic and electrolytic cells translate thermodynamic and kinetic quantities directly into precisely measureable electrical parameters.[57,92] Two electrochemical techniques were performed in this research using a MacPile potentiostat-galvanostat.

Galvanostatic Measurements. In a galvanostatic experiment a constant current is applied to an electrochemical cell, and the voltage is measured as a function of time (Figure 1.5a). During a galvanostatic experiment, a constant flux of intercalating species is maintained at the electrode/electrolyte interface and the applied current densities are usually high; therefore, the reactions are at non-equilibrium conditions.[92] This type of measurement gives an overview of the voltage profile as a function of state of charge (electrode composition) at various current densities, and capacity can also be determined. The extent of the reaction is determined from the total charge. When a constant value of current I is applied for a fixed time t, the amount of charge Q (in coulombs) that is passed across the cell can be expressed as

$$Q = It \tag{1.6}$$

Number of moles of electrons m, which is equal to number of moles of cationic species (Li^+) in the case of a lithium cell is given by

$$m = Q/F \tag{1.7}$$

where *F* is the Faraday's constant and equal to 96500 coulombs/mole of e^-, and therefore the ratio between the number of moles of Li^+ ions intercalated to the number of moles of active cathode material used in the reaction (gram/molecular weight) is equal to *x* in Li_x(host).[51,57]

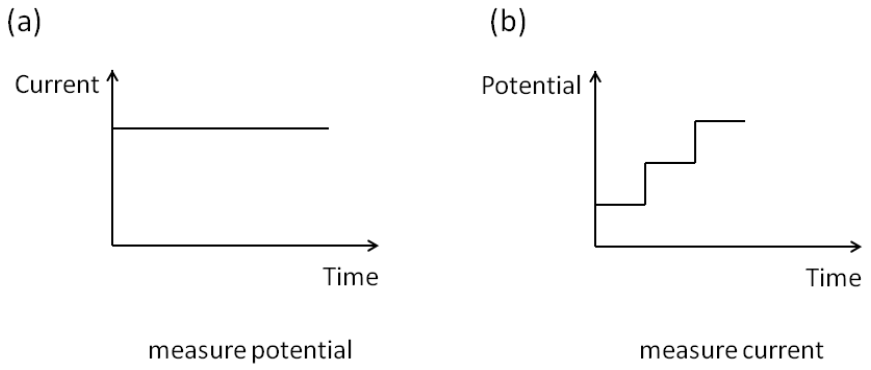

Figure 1.5 (a) Galvanostatic and (b) potentiostatic techniques.

Potentiostatic Measurements. In a potentiostatic mode, the cell potential is stepped and the current response is recorded (Figure 1.5b). Each of the voltage step takes the system to a non-equilibrium state, producing a large initial current. The current then decays to a very small preset current limit, which is a pseudo-equilibrium, before the potential is stepped again. The duration of a potential step depends on the kinetics of the process at that point in the reaction.[92] These techniques are used to determine the basic characteristics of an electroactive intercalation compound, in terms of voltage-composition relation, potential window of electrochemical stability, kinetics, and reversibility of the intercalation process.[57]

1.2.9 Building Better Batteries

Energy storage becomes more crucial today than any other time in the history of mankind. In the past decade, there has been a significantly increasing demand for portable electronic devices worldwide which is motivated by our highly mobile and technologically driven society. Among various possible energy storage systems, electrochemical batteries which can deliver the stored chemical energy as electrical energy are considered to be the most suitable.[93–97] The lithium-ion battery technology was commercially introduced in 1991 by Sony.[30,98] It is based on a graphite anode and a lithium cobalt oxide ($LiCoO_2$) cathode, which is by far the best rechargeable battery system in terms of higher operating voltage and energy density compared to conventional rechargeable batteries, such as lead-acid or Ni-MH battery (Figure 1.6).[99–104] These lithium-ion batteries have been mainly used to power today's small electronics devices, such as cell phones, camcorders, and laptop computers.[97] Billions of lithium-ion cells are produced per year with the dramatic growth in sales close to 10 billion dollars per annum and growing.[105,106]

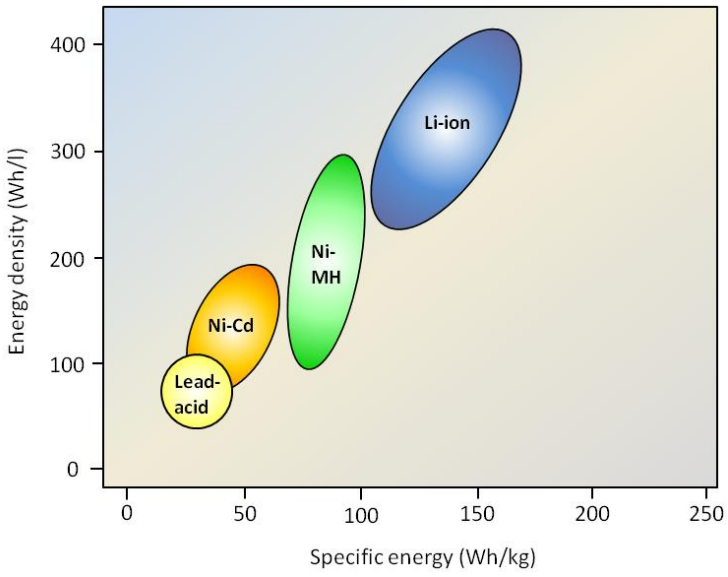

Figure 1.6 Ragone plot of the different rechargeable battery technologies in terms of energy density and specific energy after reference 94.

In light of environmental pollution and concern due to CO_2-related global warming, our present energy policy based on burning fossil fuel with limited availability has to come to an end, or at least we have to transition to a low carbon society. This drives the world to seek alternative renewable energy sources, such as solar and wind power (which require the side support of stationary energy storage units), and replacement of internal combustion engines with electric motors for travel which is one of the most consumptive activities.[30,99,105] In particular, the development of sustainable vehicles, such as hybrid electric vehicles (HEVs), plug-in hybrid electric vehicles (PHEVs), and ultimately full electric vehicles (EVs) is in progress worldwide.[62,107,108] These consequently require large-scale energy storage systems. Due to such attractive properties mentioned earlier, together with its long cycle life and rate capability, the

lithium-ion battery is still regarded as the energy storage system of choice for powering HEVs, PHEVs, and EVs.[62,109,110] Although $LiCoO_2$ is still the most dominant cathode material of today's rechargeable lithium-ion batteries for hand-held devices, because of its superior volumetric energy density, it is not a practical choice for the cathode of a large-scale lithium-ion battery due to several reasons. Firstly, cobalt (Co) is rare. It must be obtained from natural resources, and is found only 20 parts per million of the earth's crust, which makes it too costly and the availability too limited for a mass production.[105,111] Secondly, cobalt is toxic and may be a carcinogen. An overexposure to cobalt may cause irritation, allergy, and may affect lung, heart, thyroid, liver, and kidneys. Thirdly, the reversible extraction of Li from $Li_{1-x}CoO_2$ is limited to $x \approx 0.5$. As a result, it can only give a relatively low specific capacity of about 140 mAh/g. Lastly, under certain operational conditions, such as at the upper limit of the charge process (above 4.6 V) or on overcharging $x > 0.5$, oxygen may be released from the layered $LiCoO_2$ cathode causing O_2 evolution and leading to a high pressure inside a sealed cell.[62,112] Moreover, in the case of local overheating it may react with the flammable organic liquid electrolyte, giving rise to thermal runaway effects or in the worst-case scenario to explosions. These incidents have not considerably affected the consumer's electronic market; nonetheless, they cannot be tolerated in the electric vehicle market.[113]

Therefore, in order to materialize the next-generation large-scale lithium-based rechargeable batteries for HEVs, PHEVs, and EVs, as well as grid energy storage, the pursuit of new cathode materials[114–124] is undoubtedly an urgent need.

1.2.10 Beyond Lithium Systems

An alternative approach to significantly increase the energy density of rechargeable batteries could be to increase the amount of charge stored reversibly per unit weight and volume. This may require identifying new redox couples in the electrode materials.[125] Table 1.1 shows properties of some potential metal electrodes for rechargeable batteries.[126] Increasing needs in energy storage and limited excess to Li resources may alternatively lead to a shift of interest to non-Li-based batteries. Going beyond Li technology requires the exploration of new electrochemistry, and elements, such as Na and Mg are attractive for energy storage applications because of their availability and low cost. At present, Li-based batteries are relatively expensive and still suffer from some safety issues which put a question mark on the possibility of scaling them up and/or replacing the commonly used lead-acid car batteries (which are highly problematic from an environmental point of view because of the lead).[127,128]

Table 1.1 Properties of Some Potential Metals for Rechargeable Batteries

Metal	Atomic weight (g/mol)	Valency change	Specific charge (mAh/g)	Electrode potential* (V)	Terrestrial abundance (%)
Li	6.94	1	3862	–3.04	0.006
Na	22.99	1	1166	–2.71	2.64
Mg	24.31	2	2205	–2.36	1.94
Zn	65.38	2	820	–0.76	0.012
Cd	112.41	2	477	–0.40	0.00003
Pb	207.20	2	259	–0.13	0.0018

* Potential in V vs SHE. It is worth noting that many new rechargeable battery systems currently being considered are not intercalation-based. Metal-O_2 and metal-sulfur batteries are examples.[29,61,93,96,105]

While Na batteries are attractive, they are not very suitable for applications where high energy density is required, such as all-electric vehicles and portable electronics, due to the low rate capability and specific capacity of Na storage electrodes. Mg batteries, on the other hand, are currently emerging as a viable next generation rechargeable battery technology.[127] The main advantages of Mg include: (1) the ability to store up to 2 electrons per Mg atom vs one for Li and Na, resulting in a higher theoretical volumetric capacity compared to that of Li despite being heavier than Li, 3833 Ah/L for Mg and 2046 Ah/L for Li (with specific capacity of 2205 Ah/kg for Mg and 3860 Ah/kg for Li as well as negatively large redox potential of –2.36 V for Mg/Mg^{2+} and –3.04 V for Li/Li^{+} vs SHE)[129]; (2) the low cost of Mg metal compared to Li due to its abundance in the earth's crust (mostly $MgCO_3$)[130]; and (3) the atomic radius of Mg that is smaller than that of Na and is comparable to that of Li (0.76 Å for Li^{+}, 0.72 Å for Mg^{2+}, and 1.02 Å for Na^{+}).[128] As a result, it is difficult to find a suitable host material to accommodate Na^{+} ions with reversible and fast ion insertion/extraction. Moreover, Mg does not have severe dendrite formation problem that plagues Li and Na. Therefore, it promises to be safer. This drives tremendrous research efforts to develop rechargeable Mg batteries. The expected lower energy density of Mg batteries (due to a lower cell voltage) in comparison with Li-based batteries may be compensated by enhanced safety, low prices, and ease in their waste management.[126–128]

Despite several advantages of Mg electrodes, some challenges still remain in developing Mg rechargeable batteries. One of the most challenging aspects is to overcome the formation of passivating layers. Magnesium (also lithium) is a highly

reactive metal. Upon contact with species, such as water, oxygen (even trace amounts in any inert atmosphere), and various organics in conventional electrolyte solutions, passivation layers are rapidly formed on the metal surface (mostly the electrolyte decomposition products due to the reductive power of the metal).[131]

Unlike the passivation layers formed on Li metal that are Li-ion conducting, the surface films formed on Mg are truly passivating and completely block conduction of Mg ions. Therefore, electrochemical Mg dissolution in most commonly used polar aprotic solutions occurs at relatively high overpotential, via a mechanism which involves a breakdown of the surface films, and electrochemical deposition of magnesium on Mg electrodes covered by passivating surface films is impossible. This limits the selection of a suitable electrolyte solution. The solvents and salts must be stable with Mg and create a passivation-free environment to allow reversible Mg deposition and stripping. As a result, it is important to develop unique electrolyte solutions for reversible Mg metal anodes.[132–137]

Furthermore, finding cathode materials that can reversibly insert divalent Mg ions is a great challenge.[138] Compared to Li^+ insertion into the host materials, the intercalation of Mg^{2+} ions needs much higher activation energy. The divalent Mg^{2+} ion tends to coordinate both polar solvent molecules, and anions present in the electrolyte to compensate its charge. Only highly polar solvents give enough solvating power to overcome the dissociation energy necessary to form Mg^{2+} ions from salt molecules. Before Mg^{2+} ions can be inserted into a host structure, the coordinated anions and solvent

molecules have to be stripped off at the surface of the host. Once the Mg^{2+} ion is incorporated in the lattice, it tends to stay close to anionic charges and interact much more strongly than a monovalent ion. Therefore, higher activation energy is needed for hopping from one site to another and leads to slow diffusion of Mg ions.[139,140]

Also, as Mg^{2+} ions diffuse in a solid host, in order to maintain local electro-neutrality, electronic charge redistribution is another obstacle in addition to ion hopping. In intercalation compounds, the insertion is associated with change in the oxidation state of the host transition metal ions. Apparently, not all of the transition metals can undergo redox processes with a charge-transfer of more than one electron per ion. Moreover, the abrupt change in the oxidation state of transition metal cations upon multi-electron redox reactions is most likely to result in the drastic local deformations of the crystal structure.[141,142]

As described above, in order to go beyond lithium technology and develop rechargeable Mg batteries with high energy densities, some strict requirements must be met. Exploration and research efforts are still necessary to find good Mg cathode materials.

1.3 Outline of the Dissertation

This dissertation covers several aspects of the redox properties of two main groups of microporous solid compounds, namely, metal-organic frameworks and mixed transition metal oxides. It illustrates an exploitation of porous features of solid state compounds by means of inserting functional redox active guest species into a host lattice with the ultimate goal to modify or improve its desired properties. It also includes the characterization, structure determination, and investigation of the properties of the products generated. The study was divided into two directions: an intercalation of redox active molecular guest into host single crystals in the vapor phase, and an intercalation of reactive alkali and alkaline earth metals, Li and Mg, by solid state electrochemical reactions into the microporous compounds potentially with applications in lithium and magnesium rechargeable batteries. The metal-organic frameworks and mixed transition metal oxide were based on high oxidation state transition metal ions, such as vanadium, molybdenum, and iron.

Chapter 2 focuses on the synthesis of a metal-organic framework and particularly the vapor-phase redox intercalation of an organic compound under ambient and inert conditions. The structures of the single crystal products are described in detail. The result highlights interesting structures of the compounds which were either intercalated or functionalized by the guest organic molecule depending on the presence/absence of atmospheric moisture. Structural deformations as a function of temperature of the pristine phase are also discussed in comparison with those of the functionalized product.

The use of a vanadium-based metal-organic framework with an aromatic dicarboxylate as organic linkers in solid state electrochemical reaction with lithium is presented in Chapter 3. The high oxidation state (tetravalent) of the transition metal ions was exploited as the redox couple in cathodes for lithium rechargeable batteries. The cell performance and electrochemical profiles at various current conditions are discussed. Structural evolution taking place during lithium intercalation was monitored by powder X-ray diffraction.

In Chapter 4, we show that another metal-organic framework based on iron cations and formate linkers is also capable of acting as cathode material in secondary lithium batteries. The mechanism involved in the electrochemical reaction with lithium is believed to be different from that occurred in the vanadium MOF in Chapter 3. To investigate the reaction in detail, potentiostatic measurements were performed.

Chapter 5 contains the preparation and characterization of a porous mixed transition metal oxide based on molybdenum and vanadium with large open one-dimensional channels. The microcrystalline compound was used as an intercalation positive electrode material in lithium batteries with good specific capacity and rechargeability with and without conducting additives. The structural changes associated with Li-ion insertion by a chemical route are described and the chemical deintercalation of lithium is also included to demonstrate the reversibility.

Additionally, we present in Chapter 6 that the mixed Mo-V oxide is able to reversibly undergo not only lithium insertion in Li-based batteries, but also magnesium intercalation with promising applications in secondary Mg electrochemical cells. The effect of varying current densities on the discharge profiles is included along with the cyclability data. Unit cell dimensions of magnesiated phases prepared by a chemical reaction using a reducing agent were determined and analyzed in comparison with the lithiated Mo-V compound. This chapter also covers a discussion on the unique nature of this mixed metal oxide on the solid state diffusion and intercalation of Mg^{2+} ions.

Last, Chapter 7 is a summary of the results, a discussion of what was learned, some problems encountered, and suggestions for future work.

1.4 References

[1] Férey, G.; Millange, F.; Morcrette, M.; Serre, C.; Doublet, M.-L.; Grenèche, J.-M.; Tarascon, J.-M. *Angew. Chem., Int. Ed.* **2007**, *46*, 3259−3263.

[2] De Combarieu, G.; Morcrette, M.; Millange, F.; Guillou, N.; Cabana, J.; Grey, C. P.; Margiolaki, I.; Ferév, G.; Tarascon, J.-M. *Chem. Mater.* **2009**, *21*, 1602−1611.

[3] Givaja, G.; Amo-Ochoa, P.; Gómez-García, C. J.; Zamora, F. *Chem. Soc. Rev.* **2012**, *41*, 115−147.

[4] Hendon, C. H.; Tiana, D.; Walsh, A. *Phys. Chem. Chem. Phys*. **2012**, *14*, 13120−13132.

[5] Silva, C. G.; Corma, A.; García, H. *J. Mater. Chem*. **2010**, *20*, 3141−3156.

[6] Yoon, S. M.; Warren, S. C.; Grzybowski, B. A. *Angew. Chem., Int. Ed.* **2014**, *53*, 4437−4441.

[7] Meilikhov, M.; Yusenko, K.; Torrisi, A.; Jee, B.; Mellot-Draznieks, C.; Pöppl, A.; Fischer, R. A. *Angew. Chem., Int. Ed.* **2010**, *49*, 6212−6215.

[8] Halls, J. E.; Hernán-Gómez, A.; Burrows, A. D.; Marken, F. *Dalton Trans*. **2012**, *41*, 1475−1480.

[9] Meilikhov, M.; Yusenko, K.; Fischer, R. A. *Dalton Trans*. **2010**, *39*, 10990 − 10999.

[10] Yanai, N.; Uemura, T.; Ohba, M.; Kadowaki, Y.; Maesato, M.; Takenaka, M.; Nishitsuji, S.; Hasegawa, H.; Kitagawa, S. *Angew. Chem., Int. Ed.* **2008**, *47*, 9883−9886.

[11] Meilikhov, M.; Yusenko, K.; Fischer, R. A. *J. Am. Chem. Soc*. **2009**, *131*, 9644−9645.

[12] Himsl, D.; Wallacher D.; Hartmann, M. *Angew. Chem., Int. Ed.* **2009**, *48*, 4639−4642.

[13] Bloch, E. D.; Murray, L. J.; Queen, W. L.; Chavan, S.; Maximoff, S. N.; Bigi, J. P.; Krishna, R.; Peterson, V. K.; Grandjean, F.; Long, G. J.; Smit, B.; Bordiga, S.; Brown, C. M.; Long, J. R. *J. Am. Chem. Soc*. **2011**, *133*, 14814−14822.

[14] Mulfort, K. L.; Hupp, J. T. *J. Am. Chem. Soc*. **2007**, *129*, 9604−9605.

[15] Mulfort, K. L.; Wilson, T. M.; Wasielewski, M. R.; Hupp, J. T. *Langmuir* **2009**, *25*, 503−508.

[16] Bureekaew, S.; Horike, S.; Higuchi, M.; Mizuno, M.; Kawamura, T.; Tanaka, D.; Yanai, N.; Kitagawa, S. *Nat. Mater.* **2009**, *8*, 831−836.

[17] Talin, A. A.; Centrone, A.; Ford, A. C.; Foster, M. E.; Stavila, V.; Haney, P.; Kinney, R. A.; Szalai, V.; Gabaly, F. E.; Yoon, H. P.; Léonard, F.; Allendorf, M. D. *Science* **2014**, *343*, 66−69.

[18] Fuma, Y.; Ebihara, M.; Kutsumizu, S.; Kawamura, T. *J. Am. Chem. Soc*. **2004**, *126*, 12238−12239.

[19] Nagarathinam, M.; Saravanan, K.; Phua, E. J. H.; Reddy, M. V.; Chowdari, B. V. R.; Vittal, J. J. *Angew. Chem., Int. Ed.* **2012**, *51*, 5866−5870.

[20] Li, S.-L.; Xu, Q. *Energy Environ. Sci.* **2013**, *6*, 1656−1683.

[21] Morozan, A.; Jaouen, F. *Energy Environ. Sci.* **2012**, *5*, 9269−9290.

[22] Ameloot, R.; Aubrey, M.; Wiers, B. M.; Gómora-Figueroa, A. P.; Patel, S. N.; Balsara, N. P.; Long, J. R. *Chem. Eur. J.* **2013**, *19*, 5533−5536.

[23] Meilikhov, M.; Yusenko, K.; Esken, D.; Turner, S.; Tendeloo, G. V.; Fischer, R. A. *Eur. J. Inorg. Chem*. **2010**, *2010*, 3701−3714.

[24] Wade, C. R.; Li, M.; Dincă, M. *Angew. Chem., Int. Ed.* **2013**, *52*, 13377−13381.

[25] Leus, K.; Muylaert, I.; Vandichel, M.; Marin, G. B.; Waroquier, M.; Speybroeck, V. V.; Voort, P. V. D. *Chem. Commun*. **2010**, *46*, 5085−5087.

[26] Choi, H. J.; Suh, M. P. *J. Am. Chem. Soc*. **2004**, *126*, 15844−15851.

[27] Han, J. W.; Hill, C. L. *J. Am. Chem. Soc*. **2007**, *129*, 15094−15095.

[28] Allendorf, M. D.; Schwartzberg, A.; Stavila, V.; Talin, A. A. *Chem. Eur. J.* **2011**, *17*, 11372−11388.

[29] Choi, N.-S.; Chen, Z.; Freunberger, S. A.; Ji, X.; Sun, Y.-K.; Amine, K.; Yushin, G.; Nazar, L. F.; Cho, J.; Bruce, P. G. *Angew. Chem., Int. Ed.* **2012**, *51*, 9994−10024.

[30] Jeong, G.; Kim, Y.-U.; Kim, H.; Kim, Y.-J.; Sohn, H.-J. *Energy Environ. Sci.* **2011**, *4*, 1986−2002.

[31] Melot, B. C.; Tarascon, J.-M. *Acc. Chem. Res.* **2013**, *46*, 1226−1238.

[32] Dunn, B.; Kamath, H.; Tarascon, J.-M. *Science* **2011**, *334*, 928−935.

[33] Liu, C.; Li, F.; Ma, L.-P.; Cheng, H.-M. *Adv. Mater.* **2010**, *22*, E28−E62.

[34] Férey, G. *Chem. Soc. Rev.* **2008**, *37*, 191−214.

[35] Sumida, K.; Rogow, D. L.; Mason, J. A.; McDonald, T. M.; Bloch, E. D.; Herm, Z. R.; Bae, T.-H.; Long, J. R. *Chem. Rev.* **2012**, *112*, 724−781.

[36] Kitagawa, S.; Kitaura, R.; Noro, S. I. *Angew. Chem., Int. Ed.* **2004**, *43*, 2334−2375.

[37] Special issue of *Chem. Soc. Rev*. **2009**, *38*, 1201−1508.

[38] Carné, A.; Carbonell, C.; Imaz, I.; Maspoch, D. *Chem. Soc. Rev.* **2011**, *40*, 291−305.

[39] Kuppler, R. J.; Timmons, D. J.; Fang, Q.-R.; Li, J.-R.; Makal, T. A.; Young, M. D.; Yuan, D.; Zhao, D.; Zhuang, W.; Zhou, H.-C. *Coord. Chem. Rev.* **2009**, *253*, 3042−3066.

[40] Yaghi, O. M.; Li, Q. *MRS Bulletin* **2009**, *34*, 682−690.

[41] Farha, O. K.; Hupp, J. T. *Acc. Chem. Res.* **2010**, *43*, 1166−1175.

[42] Yaghi, O. M.; O'Keeffe, M.; Ockwig, N. W.; Chae, H. K.; Eddaoudi, M.; Kim, J. *Nature* **2003**, *423*, 705−714.

[43] Betard, A.; Fisher, R. A. *Chem. Rev.* **2012**, *112*, 1055−1083.

[44] Dhakshinamoorthy, A.; Alvaro, M.; Garcia, H. *Chem. Commun*. **2012**, *48*, 11275−11288.

[45] Khajavi, H.; Gascon, J.; Schins, J. M.; Siebbeles, L. D. A.; Kapteijn, F. *J. Phys. Chem. C* **2011**, *115*, 12487−12493.

[46] Wang, Z.; Cohen, S. M. *Chem. Soc. Rev.* **2009**, *38*, 1315−1329.

[47] Kim, H.; Chun, H.; Kim, G.-H.; Lee, H.-S.; Kim, K. *Chem. Commun*. **2006**, 2759−2761.

[48] Whittingham, M. S., Jacobson, A. J., Eds.; *Intercalation Chemistry;* Academic Press: New York, 1982.

[49] Lerf, A. *Dalton Trans.* **2014**, *43*, 10276−10291.

[50] Bruce, P. G., Ed. *Solid State Electrochemistry;* Cambridge University Press: Cambridge, U.K., 1995.

[51] Huggins, R. A. *Advanced Batteries: Materials Science Aspects;* Springer: New York, 2009.

[52] Winter, M.; Brodd, R. J. *Chem. Rev.* **2004**, *104*, 4245−4269.

[53] Murphy, D. W.; Christian, P. A. *Science* **1979**, *205*, 651−656.

[54] Whittingham, M. S.; Chianelli, R. R. *J. Chem. Edu.* **1980**, *57*, 569−574.

[55] Winter, M.; Besenhard, J. O.; Spahr, M. E.; Novák, P. *Adv. Mater.* **1998**, *10*, 725−763.

[56] Davies, C. W.; James, A. M. *A Dictionary of Electrochemistry;* Macmillan Press: Norfolk, U.K., 1976.

[57] Bard, A. J.; Faulkner, L. R. *Electrochemical Methods: Fundamentals and Applications,* 2nd ed.; Wiley: Hoboken, NJ, 2001.

[58] Goodenough, J. B.; Kim, Y. *J. Power Sources* **2011**, *196*, 6688−6694.

[59] Bruce, P. G. *Chem. Commun.* **1997**, 1817−1824.

[60] Whitehead, A. H.; Schreiber, M. *J. Electrochem. Soc.* **2005**, *152*, A2105−A2113.

[61] Goodenough, J. B. *Energy Environ. Sci.* **2014**, *7*, 14−18.

[62] Yuan, L.-X.; Wang, Z.-H.; Zhang, W.-X.; Hu, X.-L.; Chen, J.-T.; Huang, Y.-H.; Goodenough, J. B. *Energy Environ. Sci.* **2011**, *4*, 269−284.

[63] Narzi, G.-A., Pistoia, G., Eds.; *Lithium Battery: Science and Technology;* Springer: New York, 2009.

[64] Goodenough, J. B. *Solid State Ionics* **1994**, *69*, 184−198.

[65] Goodenough, J. B.; Park, K.-S. *J. Am. Chem. Soc.* **2013**, *135*, 1167−1176.

[66] Owen, J. R. *Chem. Soc. Rev.* **1997**, *26*, 259−267.

[67] Xu, W.; Wang, J.; Ding, F.; Chen, X.; Nasybulin, E.; Zhang, Y.; Zhang, J.-G. *Energy Environ. Sci.* **2014**, *7*, 513−537.

[68] Skundin, A. M.; Efimov, O. N.; Yarmolenko, O. V. *Russ. Chem. Rev.* **2002**, *71*, 329−346.

[69] Lee, W. W.; Lee, J.-M. *J. Mater. Chem. A* **2014**, *2*, 1589−1626.

[70] Molenda, J. *Solid State Ionics* **2005**, *176*, 1687−1694.

[71] Van Der Ven, A.; Bhattacharya, J.; Belak, A. A. *Acc. Chem. Res.* **2013**, *46*, 1216−1225.

[72] Lee, K. T.; Jeong, S.; Cho, J. *Acc. Chem. Res.* **2013**, *46*, 1161−1170.

[73] Park, M.; Zhang, X.; Chung, M.; Less, G. B.; Sastry, A. M. *J. Power Sources* **2010**, *195*, 7904−7929.

[74] Hong, S. Y.; Kim, Y.; Park, Y.; Choi, A.; Choi, N.-S., Lee, K. T. *Energy Environ. Sci.* **2013**, *6*, 2067−2081.

[75] Horike, S.; Umeyama, D.; Kitagawa, S. *Acc. Chem. Res.* **2013**, *46*, 2376−2384.

[76] Krishna, R. *Chem. Soc. Rev.* **2012**, *41*, 3099−3118.

[77] Sebastian, L.; Gopalakrishnan, J. *J. Mater. Chem.* **2003**, *13*, 433−441.

[78] Goodenough, J. B.; Kim, Y. *Chem. Mater.* **2010**, *22*, 587−603.

[79] Goodenough, J. B.; Manthiram, A.; Wnetrzewski, B. *J. Power Sources* **1993**, *43*, 269−275.

[80] Xu, K. *Chem. Rev.* **2004**, *104*, 4303−4417.

[81] Xu, K.; Cresce, A. V. *J. Mater. Chem.* **2011**, *21*, 9849−9864.

[82] Baxter, J.; Bian, Z.; Chen, G.; Danielson, D.; Dresselhaus, M. S.; Fedorov, A. G.; Fisher, T. S.; Jones, C. W.; Maginn, E.; Kortshagen, U.; Manthiram, A.; Nozik, A.; Rolison, D. R.; Sands, T.; Shi, L.; Sholl, D.; Wu, Y. *Energy Environ. Sci.* **2009**, *2*, 559−588.

[83] Guo, Y.-G.; Hu, J.-S.; Wan, L.-J. *Adv. Mater.* **2008**, *20*, 2878−2887.

[84] Xin, S.; Guo, Y.-G.; Wan, L.-J. *Acc. Chem. Res.* **2012**, *45*, 1759−1769.

[85] Roberts, M.; Johns, P.; Owen, J.; Brandell, D.; Edstrom, K.; Enany, G. E.; Guery, C.; Golodnitsky, D.; Lacey, M.; Lecoeur, C.; Mazor, H.; Paled, E.; Perre, E.; Shaijumon, M. M.; Simon, P.; Taberna, P.-L. *J. Mater. Chem.* **2011**, *21*, 9876−9890.

[86] Ji, L.; Lin, Z.; Alcoutlabi, M.; Zhang, X. *Energy Environ. Sci.* **2011**, *4*, 2682−2699.

[87] Song, H.-K.; Lee, K. T.; Kim, M. G.; Nazar, L. F.; Cho, J. *Adv. Funct. Mater.* **2010**, *20*, 3818−3834.

[88] Osiak, M.; Geaney, H.; Armstrong, E.; O'Dwyer, C. *J. Mater. Chem. A* **2014**, *2*, 9433−9460.

[89] Zhang, Q.; Uchaker, E.; Candelaria, S. L.; Cao, G. *Chem. Soc. Rev.* **2013**, *42*, 3127−3171.

[90] Wagemaker, M.; Mulder, F. M. *Acc. Chem. Res.* **2013**, *46*, 1206−1215.

[91] Goodenough, J. B. *Acc. Chem. Res.* **2013**, *46*, 1053−1061.

[92] Markevich, E.; Levi, M. D.; Aurbach, D. *J. Electroanal. Chem.* **2005**, *580*, 231−237.

[93] Scrosati, B.; Hassoun J.; Sun Y.-K. *Energy Environ. Sci.* **2011**, *4*, 3287−3295.

[94] Tarascon, J.-M.; Armand, M. *Nature* **2001**, *414*, 359−367.

[95] Vincent, C. A. *Solid State Ionics* **2000**, *134*, 159−167.

[96] Amine, K.; Kanno, R.; Tzeng, Y. *MRS Bulletin* **2014**, *39*, 395−401.

[97] Bruce, P. G.; Scrosati, B.; Tarascon, J.-M. *Angew. Chem., Int. Ed.* **2008**, *47*, 2930−2946.

[98] Ellis, B. L.; Lee, K. T.; Nazar, L. F. *Chem. Mater.* **2010**, *22*, 691−714.

[99] Wang, Y.; He, P.; Zhou, H. *Energy Environ. Sci.* **2011**, *4*, 805−817.

[100] Scrosati, B.; Garche, J. *J. Power Sources* **2010**, *195*, 2419−2430.

[101] Etacheri, V.; Marom, R.; Elazari, R.; Salitra, G.; Aurbach, D. *Energy Environ. Sci.* **2011**, *4*, 3243−3262.

[102] Hu, M.; Pang, X.; Zhou, Z. *J. Power Sources* **2013**, *237*, 229−242.

[103] Whittingham, M. S. *Chem. Rev.* **2004**, *104*, 4271−4301.

[104] Marom, R.; Amalraj, S. F.; Leifer, N.; Jacob, D.; Aurbach, D. *J. Mater. Chem.* **2011**, *21*, 9938−9954.

[105] Armand, M.; Tarascon, J.-M. *Nature* **2008**, *451*, 652−657.

[106] Special issue of *J. Mater. Chem.* **2011**, *21*, 9793−10220.

[107] Wagner, F. T.; Lakshmanan, B.; Mathias, M. F. *J. Phys. Chem. Lett.* **2010**, *1*, 2204−2219.

[108] Poizot, P.; Dolhem, F. *Energy Environ. Sci.* **2003**, *4*, 2003−2019.

[109] Zaghib, K.; Mauger, A.; Julien, C. M. *J. Solid State Electrochem*. **2012**, *16*, 835−845.

[110] Li, Z.; Zhang, D.; Yang, F. *J. Mater. Sci*. **2009**, *44*, 2435−2443.

[111] Kraytsberg, A.; Ein-Eli, Y. *Adv. Energy Mater.* **2012**, *2*, 922−939.

[112] Whittingham, M. S. *MRS Bulletin* **2008**, *33*, 411−419.

[113] Fletcher, S. *Bottled Lightning: Superbatteries, Electric Cars, and the New Lithium Economy;* Hill and Wang: New York, 2011.

[114] Gong, Z.; Yang, Y. *Energy Environ. Sci.* **2011**, *4*, 3223−3242.

[115] Meng, Y. S.; Arroyo-De Dompablo, M. E. *Acc. Chem. Res.* **2013**, *46*, 1171−1180.

[116] Islam, M. S.; Fisher, C. A. J. *Chem. Soc. Rev.* **2014**, *43*, 185−204.

[117] Yu, H.-C.; Ling, C.; Bhattacharya, J.; Thomas, J. C.; Thornton, K.; Van der Ven, A. *Energy Environ. Sci.* **2014**, *7*, 1760−1768.

[118] Goodenough, J. B. *J. Power Sources* **2007**, *174*, 996−1000.

[119] Goodenough, J. B. *Chem. Mater.* **2014**, *26*, 820−829.

[120] Wu, C.; Feng, F.; Xie, Y. *Chem. Soc. Rev.* **2013**, *42*, 5157−5183.

[121] Yuan, C.; Wu, H. B.; Xie, Y.; Lou, X. W. *Angew. Chem., Int. Ed.* **2014**, *53*, 1488−1504.

[122] Robert, R.; Villevieille, C.; Novák, P. *J. Mater. Chem. A* **2014**, *2*, 8589−8598.

[123] Hahn, B. P.; Long, J. W.; Rolison, D. R. *Acc. Chem. Res.* **2013**, *46*, 1181−1191.

[124] Chernova, N. A.; Roppolo, M.; Dillon, A. C.; Whittingham, M. S. *J. Mater. Chem.* **2009**, *19*, 2526−2552.

[125] Yoo, H. D.; Shterenberg, I.; Gofer, Y.; Gershinsky, G.; Pour, N.; Aurbach, D. *Energy Environ. Sci.* **2013**, *6*, 2265−2279.

[126] Besenhard, J. O.; Winter, M. *ChemPhysChem* **2002**, *3*, 155−159.

[127] Malyi, O. I.; Tan, T. L.; Manzhos, S. *J. Power Sources* **2013**, *233*, 341−345.

[128] Shterenberg, I.; Salama, M.; Gofer, Y.; Levi, E.; Aurbach, D. *MRS Bulletin* **2014**, *39*, 453−459.

[129] Ichitsubo, T.; Adachi, T.; Yagi, S.; Doi, T. *J. Mater. Chem.* **2011**, *21*, 11764−11772.

[130] Aurbach, D.; Gofer, Y.; Lu, Z.; Schechter, A.; Chusid, O.; Gizbar, H.; Cohen, Y.; Ashkenazi, V.; Moshkovich, M.; Turgeman, R.; Levi, E. *J. Power Sources* **2001**, *97*, 28−32.

[131] Muldoon, J.; Bucur, C. B.; Oliver, A. G.; Sugimoto, T.; Matsui, M.; Kim, H. S.; Allred, G. D.; Zajicek, J.; Kotani, Y. *Energy Environ. Sci.* **2012**, *5*, 5941−5950.

[132] Verma, P.; Maire, P.; Navák, P. *Electrochim. Acta* **2010**, *55*, 6332−6341.

[133] Shao, Y.; Gu, M.; Li, X.; Nie, Z.; Zuo, P.; Li, G.; Liu, T.; Xiao, J.; Cheng, Y.; Wang, C.; Zhang, J.-G.; Liu, J. *Nano Lett.* **2014**, *14*, 255−260.

[134] Aurbach, D.; Gofer, Y.; Schechter, A.; Chusid, O.; Gizbar, H.; Cohen, Y.; Moshkovich, M.; Turgeman, R. *J. Power Sources* **2001**, *97*, 269−273.

[135] Amalraj, S. F.; Aurbach, D. *J. Solid State Electrochem.* **2011**, *15*, 877−890.

[136] Levi, E.; Lancry, E.; Gofer, Y.; Aurbach, D. *J. Solid State Electrochem.* **2006**, *10*, 176−184.

[137] Lu, Z.; Schechter, A.; Moshkovich, M.; Aurbach, D. *J. Electroanal. Chem.* **1999**, *466*, 203−217.

[138] Levi, E.; Gofer, Y.; Aurbach, D. *Chem. Mater.* **2010**, *22*, 860−868.

[139] Kohler, J.; Imanaka, N.; Adachi, G. *Chem. Mater.* **1998**, *10*, 3790−3812.

[140] Navák, P.; Imhof, R.; Hass, O. *Electrochim. Acta* **1999**, *45*, 351−367.

[141] Levi, M. D.; Lancri, E.; Levi, E.; Gizbar, H.; Gofer, Y.; Aurbach, D. *Solid State Ionics* **2005**, *176*, 1695−1699.

[142] Levi, E.; Levi, M. D.; Chasid, O.; Aurbach, D. *J. Electroceram.* **2009**, *22*, 13−19.

Chapter 2

Redox Intercalation of Hydroquinone into a Flexible Metal-Organic Framework

2.1 Introduction

Emerging as a new class of porous crystalline materials, metal-organic frameworks (MOFs), assembled from inorganic building units (metal ions or clusters) and organic linkers, have attracted tremendous attention in the past two decades.[1–3] Due to the design and synthesis flexibility inherent in MOFs, many efforts have been made to address technological applications using these materials in categories, such as gas storage, selective molecular adsorption, separations, ion exchange, catalysis, magnetic and photoluminescence responses, optoelectronics, and drug delivery.[4–9] In contrast to conventional rigid inorganic porous solids, such as zeolites,[10] some of the hybrid organic-inorganic porous frameworks can demonstrate significant structural flexibility (dynamic frameworks) upon loading/unloading of guest species or in response to external stimuli, such as the guest concentration, pressure, and temperature with retention of single crystallinity.[11–16] These porous materials have the potential to be applied as advanced adsorbents and sensors, in particular.[17–20]

Examples of framework flexibility have been found in a number of MOFs.[11–16] Among them, a group of compounds with the general framework formula MX(bdc), first reported by Férey and co-workers, are based on chains of *trans* corner-sharing MX_2O_4 (M = V,[21,22] Cr,[23] Al,[24,25] Fe,[26–28] In,[29] Ga,[30] Mn,[31] Sc,[32,33] and X = O, OH, F) octahedra cross-linked by 1,4-benzenedicarboxylate (bdc). The three-dimensional framework that

results consists of one-dimensional rhombic channels. The first member of the group $[V^{III}(OH)(bdc)](H_2bdc)_x$, known as MIL-47as, loses the guest acid on heating in air and at the same time the framework V^{3+} ions are oxidized to V^{4+} forming $[V^{IV}(O)(bdc)]$ or MIL-47, without changing the topology of the framework, thus providing the first evidence of chemically induced redox reactions within this system.[21] We have previously reported the direct synthesis of large single crystals of $[V^{IV}(O)(bdc)](H_2bdc)_{0.71}$.[22] After removal of the guest acid molecules by heating the crystals of $[V^{IV}(O)(bdc)](H_2bdc)_{0.71}$ in air, we have shown that the $[V^{IV}(O)(bdc)]$ structure is sufficiently flexible to undergo single-crystal-to-single-crystal transformations upon adsorption of organic molecules, such as aniline, thiophene, and acetone, enabling the details of the guest structures, framework-guest interactions, and framework deformations upon removal or adsorption of guest species to be determined.[22,34]

In addition to the oxidative removal of the H_2bdc template from MIL-47as, Jacobson and co-workers synthesized two iron members of the family, namely, $[Fe^{III}(OH)(bdc)](py)_{0.85}$ and $[Fe^{II}(bdc)(dmf)]$ (py = pyridine and dmf = dimethylformamide), where the change in the iron oxidation state is brought about by replacing the OH^- bridging species by the neutral oxygen atom in dmf.[27] Moreover, Férey and co-workers investigated the electrochemical reactivity of MIL-53(Fe), another iron analog of the compound series formulated as $[Fe^{III}(OH)_{0.8}F_{0.2}(bdc)](H_2O)$, with lithium. The result suggests that Li^+ ions can be reversibly intercalated/deintercalated into the channels, accompanied by reduction/oxidation of Fe^{3+} and Fe^{2+}.[35] An attempt to increase

the electrochemical capacity was also made by the adsorption of an electroactive molecule, 1,4-benzoquinone.[36]

One particular feature of $[V^{IV}(O)(bdc)]$, MIL-47, is its lack of affinity for water. As a result, by removing H_2bdc guest molecules, the empty framework is obtained and stable under ambient conditions.[21,22] This is in contrast to the behavior of, for example, the aluminum analog in the series $[Al^{III}(OH)(bdc)]$, also designated as MIL-53(Al), which readily adsorbs water from the atmosphere, accompanied by a substantial decrease in channel aperture referred to by Férey as "breathing".[24] MIL-53(Al) has also been found to exhibit a reversible structural transition between the open- and closed-pored structures as a function of temperature in the absence of any guest molecules.[37] Other examples of structural flexibility among this compound series particularly in response to external stimuli, such as temperature and pressure, have also been reported.[28,33,38–43]

One of the enticing features of MOFs is the potential to control the chemical nature of the pores through post-synthetic modification, whereby a preformed MOF undergoes further reaction.[44] One way to fine tune the physical and chemical properties of MOFs is to incorporate functional guest molecules inside the pores of the network.[45] As mentioned above, the $[V^{IV}(O)(bdc)]$ framework can be completely evacuated at ambient atmosphere due to the absence of bridging –OH group. Once the channels are empty, other species may be reversibly intercalated.

Among the numerous properties which can be hosted by porous organic-inorganic frameworks, the redox and electrical properties have received relatively limited attention.[46–48] MOFs still face a number of challenges in this area, particularly with regard to their insulating nature.[49] The incorporation of redox active guest molecules represents one strategy toward improving the charge transport properties of the materials.[50,51] The host-guest chemistry of MOFs which exhibits redox active frameworks and shows charge-transfer between the framework and the adsorbed molecules, is an underdeveloped, but very promising and challenging area of research.[52] The changes in the redox state are usually accompanied by changes in the coordination number of the metal ion, which can lead to a non-reversible degradation of the MOF structure.[53,54] Nevertheless, compounds stable upon redox reactions could lead to enhanced gas storage, electronic conductivity, or open new perspectives, such as the use of MOFs as porous electrodes for lithium-ion batteries, fuel cells, capacitors, and as active molds for the preparation of metallic nanoparticles, as well as in the areas of solid state sensing and electrocatalysis.[35,36,46–70]

Hydroquinone (H_2Q), or benzene-1,4-diol, is well-known as key building block in many biological proton-electron transfer reactions. In particular, hydroquinone can reversibly undergo a 2 e^-, 2 H^+ transfer to give *p*-benzoquinone (Q): $H_2Q = Q + 2H^+ + 2e^-$. Hydroquinone/*p*-benzoquinone system is perhaps the most well-studied and considered as the classical organic redox reaction.[71,72] This motivated us to investigate the intercalation of the redox active guest, hydroquinone into the [V^{IV}(O)(bdc)] host framework. The temperature dependence of the framework structures is also discussed.

2.2 Experimental Section

2.2.1 Materials and Measurements

All chemicals used during this work were reagent grade and used as received from commercial sources without further purification. Infrared (IR) measurements were carried out on a PerkinElmer Spectrum 100 FT-IR spectrometer in the range 400−4000 cm^{-1}. Thermogravimetric analysis (TGA) measurements were carried out using a TA Instruments Hi-Res 2950 system with a heating rate of 2 °C/min. Elemental analyses were performed by Galbraith Laboratories (Knoxville, TN). Powder X-ray diffraction (PXRD) patterns were collected at room temperature on a Phillips PANalytical X'Pert PRO diffractometer with Cu Kα radiation (λ = 1.54046 Å). X-band EPR measurements were performed on a Bruker BioSpin instrument.

2.2.2 Synthesis of $[V^{IV}(O)(bdc)](H_2bdc)_{0.71}$ (1)

Compound **1** was synthesized by hydrothermal reaction as previously reported.[22] A reaction mixture of VO_2, HCl, H_2bdc, and H_2O (molar ratio = 1:2:0.5:77) was heated in a 23 mL Teflon-lined Parr stainless steel autoclave at 220 °C for 3 d under autogenous pressure. Red brown prisms of **1** were recovered as a major phase by vacuum filtration and drying in air, together with a minor dark green impurity, which was easily removed by washing with methanol.

2.2.3 Activation of $[V^{IV}(O)(bdc)](H_2bdc)_{0.71}$ (1)

To obtain $[V^{IV}(O)(bdc)]$ (**2**), red crystals of **1** were heated at 380 °C for 4 h in air to remove H_2bdc from the channels. After cooling to room temperature, the crystals were transferred to a quartz tube, evacuated to a pressure less than 10^{-2} mTorr, and heated to 350 °C for 2 h under vacuum to sublime any remaining H_2bdc.

2.2.4 Redox Intercalation of Hydroquinone

Hydroquinone (H_2Q) was loaded into reaction vessels by two different methods as follows:

Ambient Air Method. The activated MOF (**2**) was placed together with hydroquinone in a 23 mL Teflon-lined Parr stainless steel autoclave in separate small glass vessels with the molar ratio **2**:H_2Q = 1:47 in air. The autoclave was heated to 220 °C for 24 h and then cooled to room temperature. The dark red crystals of **2** turned black after the intercalation. The final product was determined to be $[V^{III}(OH)(bdc)]\cdot\{(O\text{-}C_6H_4\text{-}O)(HO\text{-}C_6H_4\text{-}OH)\}_{0.76}\cdot(H_2O)_{0.48}$ (**3**). Anal. Calcd.: V, 12.53; C, 50.58; H, 3.36. Found: V, 13.16; C, 50.93; H, 2.98 wt%.

Anhydrous Atmosphere Method. The reactants were loaded inside an argon-filled glovebox and all manipulations were carried out under an inert atmosphere. The activated MOF (**2**) and hydroquinone with the molar ratio **2**:H_2Q = 1:47 were used. Hydroquinone which had been dried in vacuum at 110 °C overnight was placed on the bottom of a quartz tube. Crystals of **2** were wrapped in gold mesh and placed above

hydroquinone using a gold wire. The quartz tube was then evacuated to a pressure less than 10^{-2} mTorr at room temperature overnight before it was sealed under vacuum. The tube was heated to 150 °C at 10 °C/min and subsequently heated to 290 °C for 30 min with a heating rate of 1 °C/min. The dark red crystals of **2** turned black after the intercalation. The final product was determined to be $[V^{III}(O\text{-}C_6H_4\text{-}O)(bdc)]$ (**4**). Anal. Calcd.: V, 15.76; C, 52.04; H, 2.50. Found: V, 14.99; C, 52.84; H, 2.83 wt%.

2.2.5 Crystallography

Single crystal X-ray analyses were performed at room temperature on a Siemens SMART platform diffractometer outfitted with an APEX II area detector and monochromatized Mo Kα radiation (λ = 0.71073 Å). The structures were solved by direct methods and refined using SHELXTL software package.[73] The hydrogen atoms of the organic species were located geometrically and refined isotropically with position and displacement parameters riding on the non-hydrogen atoms which they are bonded to. Hydrogen atoms of the disordered water molecules were not located. Crystallographic data and structure refinements for compounds **3** and **4** are summarized in Table 2.1.

2.2.6 Structural Transition as a Function of Temperature

Unit cell parameters of **4** were measured as a function of temperature in comparison with those obtained from $[V^{IV}(O)(bdc)]$ (**2**). Single crystals of compounds **2** and **4** with suitable sizes were selected and mounted on the Siemens SMART platform diffractometer as described above. The measurements were performed in the following temperature sequence: 296.2, 233.2, 183.2, 143.2, and 100.0 K under a N_2 cold stream.

2.3 Results and Discussion

2.3.1 Synthesis

$[V^{IV}(O)(bdc)](H_2bdc)_{0.71}$ (**1**) can be prepared by the hydrothermal method previously described. To remove the large amount of H_2bdc guest species from the channels, the activation of **1** is done in two steps. The red crystals of **1** are first heated in air at 380 °C to remove the majority of H_2bdc. After cooling to room temperature, the crystals are transferred to a quartz tube, evacuated to a pressure less than 10^{-2} mTorr, and heated again to 350 °C under vacuum to sublime any remaining H_2bdc. A very small amount of white H_2bdc solid appears on the cold part of the tube and the tube is sealed to separate $[V^{IV}(O)(bdc)]$ (**2**) from the last trace of H_2bdc. This is done to ensure the completeness of framework activation. It was found that the quality of the activated crystals is highly dependent on the heating rate during the activation. As reported previously, the unit cell dimensions change as H_2bdc guest molecules are removed from

the structure: $[V^{IV}(O)(bdc)](H_2bdc)_{0.71}$ (**1**), $P2_12_12_1$, a = 6.8094(3), b = 12.4220(6), c = 17.1733(8) Å, V = 1452.6(1) $Å^3$ and $[V^{IV}(O)(bdc)]$ (**2**) *Pnma*, a = 6.8249(8), b = 16.073(2), c = 13.995(2) Å, V = 1535.2(3) $Å^3$.[22] These changes during the framework activation lead to cracks in the single crystals of **2**. As a result, the lower the heating rate, the better the quality of the activated crystals.

Once the empty framework of **2** is obtained, hydroquinone (H_2Q) is used as guest for redox intercalation by two different methods: in ambient air and under anhydrous conditions. When $[V^{IV}(O)(bdc)]$ (**2**) and hydroquinone are loaded in air, moisture from air is an important factor that drives the intercalation towards the product $[V^{III}(OH)(bdc)]\cdot\{(O\text{-}C_6H_4\text{-}O)(HO\text{-}C_6H_4\text{-}OH)\}_{0.76}\cdot(H_2O)_{0.48}$ (**3**). As hydroquinone molecules are inserted into $[V^{IV}(O)(bdc)]$ framework in the presence of water, quinhydrone[74,75] which is a well-known charge-transfer complex between hydroquinone (H_2Q) and *p*-benzoquinone (Q), is formed inside the channels together with a small amount of water, and simultaneously V^{4+} ions are reduced to V^{3+}. Under anhydrous conditions, hydroquinone molecules are found to functionalize the $[V^{IV}(O)(bdc)]$ framework itself, as V^{4+} ions are reduced to V^{3+} to form $[V^{III}(O\text{-}C_6H_4\text{-}O)(bdc)]$ (**4**). In both methods (in ambient air and under anhydrous atmosphere), the transformations take place via a single-crystal-to-single-crystal fashion (single crystals of **2** to **3**, and **2** to **4**, respectively).

Table 2.1 Crystallographic Data of **3** and **4**

	Compound **3**	Compound **4**
Empirical formula	$VO_{8.52}C_{17.12}H_{13.56}$	$VO_6C_{14}H_8$
Formula weight	322.05	323.14
Temperature	293(2)	296(2)
Crystal system	orthorhombic	orthorhombic
Space group	*Pbcm*	*Imma*
a (Å)	12.6011(13)	18.365(10)
b (Å)	17.2874(18)	6.855(4)
c (Å)	13.7364(14)	10.380(6)
α (deg)	90.00	90.00
β (deg)	90.00	90.00
γ (deg)	90.00	90.00
V (Å^3)	2992.3(5)	1306.7(12)
Z	8	4
Calcd. density (g/cm^3)	1.43	1.643
F_{000}	1303	652
Reflections collected	17496	2984
Unique reflections	3787	831
R_{int}	0.0428	0.0842
Parameters/restraints	224/21	64/0
μ (mm^{-1})	0.689	0.784
θ range for data collection (deg)	1.62−28.29	2.22−28.13
Goodness-of-fit on F^2	1.037	1.272
Final *R* indices [$I > 2\sigma(I)$]	R_1 = 0.0524, wR_2 = 0.1647	R_1 = 0.0972, wR_2 = 0.2315
R indices (all data)	R_1 = 0.0936, wR_2 = 0.2091	R_1 = 0.1064, wR_2 = 0.2363
Largest diff. peak and hole	0.599 and −0.321 e/Å^3	0.805 and −0.774 e/Å^3

2.3.2 Porous Structure of $[V^{IV}(O)(bdc)]$ (2)

The structure of **2** has been described previously.[21,22] Chains of *trans* corner-sharing VO_6 octahedra (Figure 2.1a), which are cross-linked by 1,4-benzenedicarboxylate (bdc) are shown in Figure 2.1b. The octahedral chains have a −O=V−O=V− backbone with alternating short (1.612(1) Å) and long (2.189(2) Å) V−O apical bonds of the VO_6 octahedra, indicating that the vanadium ions are in the tetravalent oxidation state, and a V−O−V angle of 128.7°. The equatorial corners of the VO_6 octahedra are shared with the bdc ligands. The one-dimensional channels parallel to the octahedral chains have a diamond-shaped cross-section with an aperture of ~7.6 x 7.7 Å (Figure 2.1c). The structure has a space group symmetry of *Pnma* with the octahedral chains parallel to the *a*-axis and the (010) plane running through the zigzag −O=V−O=V− backbone. The bdc ligands are flat with their benzene ring plane almost parallel to the channel axis. The angle between the bdc benzene ring and the channel axis is only 3.7°. This small inclination of bdc toward the channel axis causes a slight fluctuation of the channel aperture along the channel axis and makes the individual channels polar. However, the polarities of neighboring channels are in opposite directions, causing the structure as a whole to be non-polar. The angle between the long axis of the bdc ligand and the octahedral chain is 86.6°, which is less than the 90° angle found in the closely related M(OH)(bdc) structures. Presumably, the deviation is caused by the polar feature of individual octahedral chains of **2**, originating from alternating short and long V− O bonds.[22]

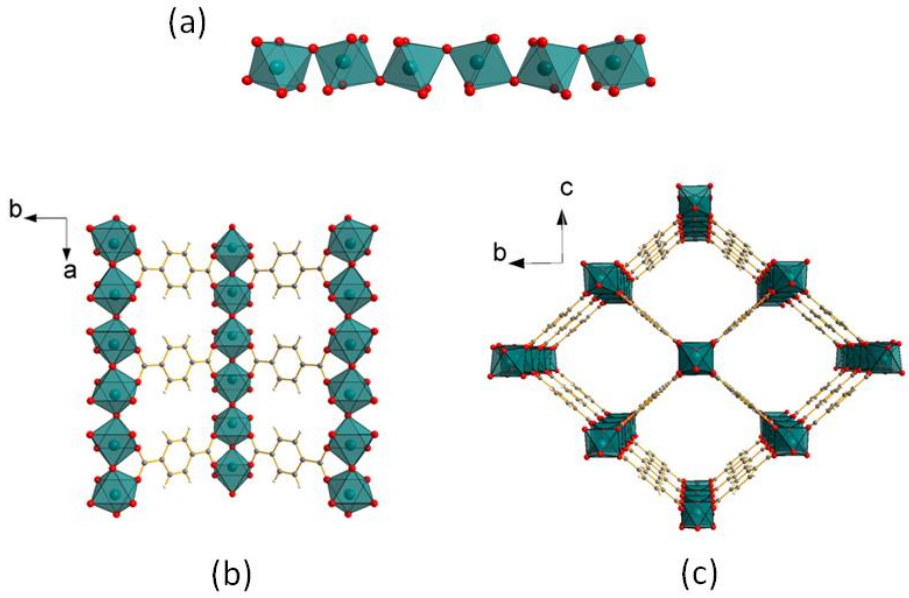

Figure 2.1 Structure of $[V^{IV}(O)(bdc)]$ framework (**2**): (a) Chain of *trans* corner-sharing VO_6 octahedra. (b) VO_6 chains cross-linked by 1,4-benzenedicarboxylate (bdc). (c) Projection of the framework along the *a*-axis showing one-dimensional diamond-shaped channels with an aperture of ~7.6 x 7.7 Å. (Illustrated in blue, V^{IV}; red, O; grey, C; white, H.)

2.3.3 Structure of $[V^{III}(OH)(bdc)]\cdot\{(O\text{-}C_6H_4\text{-}O)(HO\text{-}C_6H_4\text{-}OH)\}_{0.76}\cdot(H_2O)_{0.48}$ (3)

During redox intercalation in ambient air at 220 °C under autogenous pressure, some of the hydroquinone (H_2Q) (Figure 2.2a) first undergoes oxidation to form *p*-benzoquinone (Q) in a two-electron process: $H_2Q \rightarrow Q + 2H^+ + 2e^-$.[71] Once *p*-benzoquinone (Q) is produced, it can combine with the excess hydroquinone to form the quinhydrone complex[74] (Figure 2.2b). Simultaneously, V^{4+} ions in the $[V^{IV}(O)(bdc)]$

framework (**2**) are reduced by the electrons generated to V^{3+} and the protons attach to the bridging oxygen atom; thus, μ_2-oxo becomes μ_2-OH.

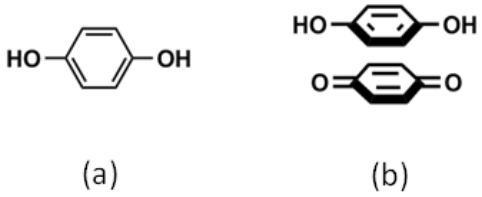

Figure 2.2 (a) Hydroquinone molecule. (b) Quinhydrone charge-transfer complex between *p*-benzoquinone (Q) and hydroquinone (H_2Q).

The three-dimensional structure of **3** is illustrated in Figure 2.3. The host framework is closely similar to that of the previously reported MIL-47as which is based on V^{III}.[21] The six V−O distances in **3** lie in the range of 1.938(1) − 2.012(2) Å, which is typical for V^{III} −O bonds. The vanadium oxygen octahedron is slightly compressed with axial V−O bond lengths of 1.938(1) and 1.941(1) Å, and equatorial V−O bond lengths of 2.003(2) − 2.012(2) Å. The axial oxygen atoms are shared by neighboring octahedra to form a zigzag ···OH −V− OH −V−··· backbone with alternating V−OH−V angles of 124.7 and 124.4°. The equatorial oxygen atoms are shared with the dicarboxylate anions that cross-link the octahedral chains into a 3D framework. The bond valence sum calculated for the V ion is 3.13 v.u. in agreement with the V^{3+} assignment.[76]

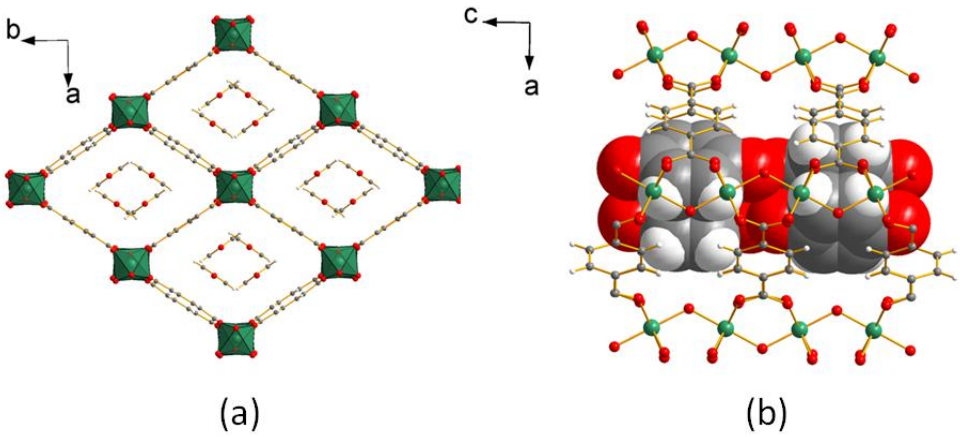

Figure 2.3 Structure of $[V^{III}(OH)(bdc)]\cdot\{(O\text{-}C_6H_4\text{-}O)(HO\text{-}C_6H_4\text{-}OH)\}_{0.76}\cdot(H_2O)_{0.48}$ (**3**): (a) View of the three-dimensional structure of **3** along the *c*-axis showing intercalated quinhydrone complexes in the channels. (b) A portion of the channel system of **3** displaying two quinhydrone complexes in space-filling representation. (Illustrated in green, V^{III}; red, O; grey, C; white, H; water molecules are omitted for clarity.)

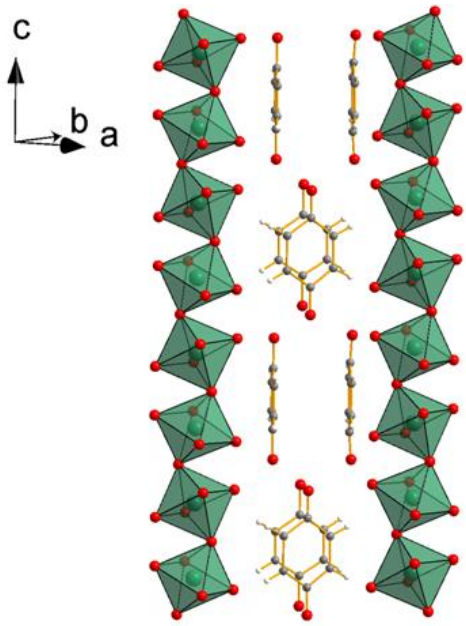

Figure 2.4 Projection of the structure of **3**, $[V^{III}(OH)(bdc)]\cdot\{(O\text{-}C_6H_4\text{-}O)(HO\text{-}C_6H_4\text{-}OH)\}_{0.76}\cdot(H_2O)_{0.48}$, showing a column of quinhydrone complexes along with corner-sharing VO_6 octahedral chains. (Illustrated in green, V^{III}; red, O; grey, C; white, H; water molecules are omitted for clarity.)

The rhombic-shaped channels of the framework of **3** are filled with guest quinhydrone complexes. Intercalated into the empty channels of **2** in the vapor phase, the quinhydrone complex, composed of equimolar *p*-benzoquinone (Q) and hydroquinone (H_2Q), is held together by π-π charge-transfer interactions. The electron-withdrawing carbonyl groups on *p*-benzoquinone make the aromatic ring relatively poor in π electron density; as a result, *p*-benzoquinone behaves as an electron acceptor. On the other hand, the electron-donating hydroxyl groups on hydroquinone make the aromatic ring relatively electron rich, and make hydroquinone a good electron donor.[75] The hydroquinone and *p*-

benzoquinone in **3** are separated by the π-π stacking distance of 3.784 Å (measured between the two parallel planes), which indicates a π-π interaction with substantial ring-ring offset (shifted ca. 1.4 Å from the ideal onset position along the axis perpendicular to the axis that runs through the ···O − benzene ring − O···).

The intercalated complexes form a column along the *c*-axis parallel to the corner-sharing VO_6 octahedral chains as shown in Figure 2.4, with the quinhydrones in neighboring tunnels oriented perpendicular to each other. The guest quinhydrone complexes in **3** lie parallel to the tunnel axis and the bdc ligands of the framework, which maximizes packing efficiency and facilitates π-π interactions with the framework bdc molecules. This pattern allows all columns of guest molecules to have favorable π-π interactions with the framework bdc linkers, with the distances of 3.387− 3.466 Å between the benzene-ring center of hydroquinone or *p*-benzoquinone and the bdc benzene rings. This primary π-π interaction between the quinhydrone and the framework bdc molecule seems to play a major role in dictating the quinhydrone orientation.

The π-π interactions between hydroquinone and *p*-benzoquinone in the quinhydrone are complemented by fairly strong hydrogen bonds (OH···O: 2.70(2)− 2.79(1) Å) between adjacent hydroquinone and *p*-benzoquinone molecules in an alternating fashion as shown in Figure 2.5 to form an infinite chain. *p*-Benzoquinone is found to be randomly disordered over two positions, laterally shifted 0.91(2) Å apart approximately along [110]. The disorder of *p*-benzoquinone is related to the incorporation of the water molecules that are also randomly disordered over two positions 1.12(3) Å apart.

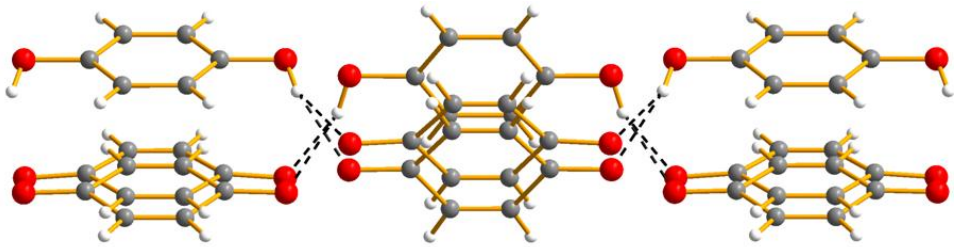

Figure 2.5 Quinhydrone complex column in compound **3**: Each complex contains 1 hydroquinone: 1 *p*-benzoquinone held together by π-π interactions. (*p*-benzoquinone is disordered over two positions.) Each pair of complex is linked to one another by hydrogen bonding (dashed line) to form a chain. (red, O; grey, C; white, H.)

The packing of the intercalated quinhydrone complex in **3** differs from that found in the triclinic and monoclinic forms of quinhydrone previously reported.[77,78] In the intercalation compound **3**, adjacent pairs of hydroquinone and *p*-benzoquinone are rotated by 70.4°, while in triclinic and monoclinic structures the adjacent pairs of molecules are located on the same plane forming flat sheets of infinite hydrogen bonded quinhydrone complexes with π-π stacking distance of 3.221 Å and hydrogen bonding distance OH···O between adjacent hydroquinone and *p*-benzoquinone molecules of 2.739 and 2.738 Å for the triclinic and monoclinic structures, respectively.[77,78] In the triclinic and monoclinic modifications, the π-π charge-transfer between the electron donor (hydroquinone) and the electron acceptor (*p*-benzoquinone) is found to be the primary source for complex stabilization due to the short π-π distance which indicates a strong π-π interaction, while the hydrogen bonds provide additional stability.[75]

The occupancy of the quinhydrone complex was refined to approximately 0.76 in good agreement with the elemental analysis and TGA results. In addition to the intercalated quinhydrone, water molecules were also located in the channels of **3**. Each water molecule is weakly hydrogen bonded to an μ_2-OH group of the octahedral chain and −C=O of *p*-benzoquinone with the O···O distance of 3.08(2) and 3.04(4) Å, respectively. Upon intercalation of the guest molecules, the tunnel openings in [V(O)(bdc)] systematically shrink because of the interactions between the guest molecules and the host framework. This behavior is illustrated by the ratio of the two diagonals of the tunnel section, which changes from 14.00:16.07 (0.87) in **2** to 12.60:17.29 (0.73) in **3**. The deformations are realized mainly through changes of the torsion angle V−O=C−C, which is the most flexible component of the framework.[21,22]

Cooperative proton and electron transfer (PET) phenomena have been well-observed in quinhydrones and many biological systems experimentally and theoretically.[74] Quinhydrone complexes have been shown to undergo an intermolecular proton-electron transfer reaction through the combined π-π interactions and hydrogen bonding as illustrated in Scheme 2.1.[79] These phenomena in the quinhydrone itself may lead to interesting electrical properties of compound **3**, in addition to the conductivity that could take place along the ···OH −V− OH −V−··· chain.

Scheme 2.1 Proton-Electron Transfer Phenomena in Quinhydrone Complexes

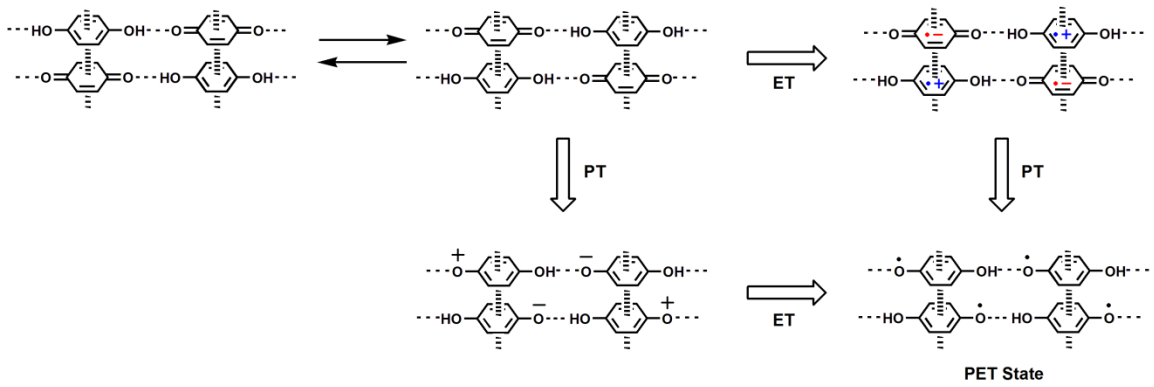

2.3.4 Structure of $[V^{III}(O\text{-}C_6H_4\text{-}O)(bdc)]$ (4)

When $[V^{IV}(O)(bdc)]$ (**2**) and hydroquinone are heated together at 290 °C under anhydrous conditions, hydroquinone (H_2Q) first thermally decomposes via the formation of a resonance stabilized *p*-semiquinone radical and *p*-semiquinone radical anion, to yield *p*-benzoquinone (Q) as the dominant product as described in Scheme 2.2. As reported by Dellinger and co-workers, the thermal degradation of hydroquinone initiates at 250°C and *p*-benzoquinone is the only observable product below 700 °C. This strongly suggests the formation of *p*-semiquinone radical as an intermediate.[80,81]

Scheme 2.2 Formation of *p*-Semiquinone Radical and *p*-Benzoquinone from the Pyrolysis of Hydroquinone

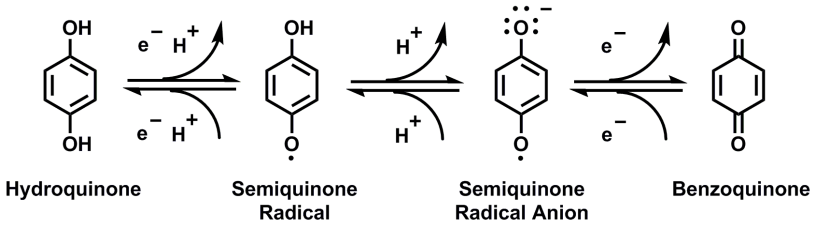

During the first step of the thermal decomposition, one electron (e^-) and one proton (H^+) are given off, as hydroquinone (H_2Q) becomes *p*-semiquinone radical. This electron then reduces V^{4+} ion in the $[V^{IV}(O)(bdc)]$ framework (**2**) to V^{3+}, and the proton simultaneously protonates the bridging oxygen μ_2-oxo to become μ_2-OH. As the *p*-semiquinone radical further transforms into *p*-semiquinone radical anion, it gives off one more proton (H^+), which then protonates the μ_2-OH. The *p*-semiquinone radical anion is believed to be the species responsible for functionalizing the vanadium octahedral chain. As the *p*-semiquinone radical anion attacks the vanadium chain, a water molecule departs the chain. This functionalization of the chains by the *p*-semiquinone radical anion takes place throughout the structure, until all the bridging μ_2-oxygen atoms are replaced by *p*-semiquinone radical anions and all of the V^{4+} ions are reduced to V^{3+} ions as shown in Figure 2.6.

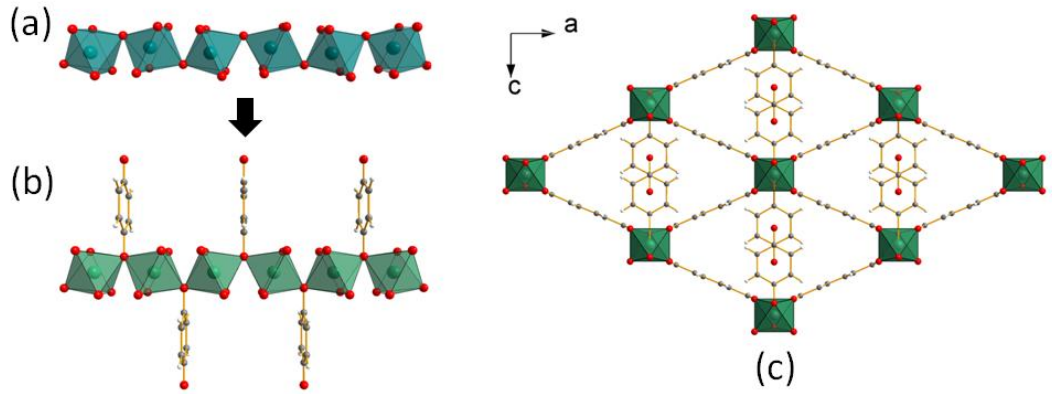

Figure 2.6 (a) Chain of *trans* corner-sharing VO_6 octahedra of the $[V^{IV}(O)(bdc)]$ framework (**2**) before the reaction with hydroquinone in anhydrous atmosphere. (b) Chain of *trans* corner-sharing VO_6 octahedra after the reaction: V^{IV} in compound **2** is reduced to V^{III} as the μ_2-oxo bridging oxygen atom is replaced by the *p*-semiquinone radical anion to yield $[V^{III}(O\text{-}C_6H_4\text{-}O)(bdc)]$ (**4**). (c) Structure of $[V^{III}(O\text{-}C_6H_4\text{-}O)(bdc)]$ (**4**) along the channel axis. (Illustrated in blue, V^{IV}; green, V^{III}; red, O; grey, C; white, H.)

The three-dimensional structure of **4** is illustrated in Figure 2.6c. The six V−O distances in **4** lie in the range of 1.933(4) − 1.986(5) Å, which is typical for V^{III}−O bonds. The vanadium oxygen octahedron is slightly compressed with an axial V−O bond length of 1.933(4) Å, and equatorial V−O bond length of 1.986(5) Å. The axial oxygen atoms are shared by neighboring octahedra to form a zigzag $\cdots O(C_6H_4O) - V - O(C_6H_4O) - V - \cdots$ backbone with a $V{-}O(C_6H_4O){-}V$ angle of 124.8°. The equatorial oxygen atoms are shared with the dicarboxylate anions that cross-link the octahedral chains into a 3D framework. The oxygen−benzene ring−oxygen in $-O-C_6H_4-O$ lie flat on the same plane

and perpendicular to the corner-sharing VO_6 octahedral chains and the tunnel axis. Bond valence sum calculated for the V is 3.27 v.u. in agreement with the assignment as V^{III}.[76]

The C−O bond protruding into the channel that is part of $-O(C_6H_4O)$ has a bond length of 1.29(7) Å corresponding to a bond order of ca. 1.5, which is in agreement with the known resonance and conjugation effect for a semiquinone radical. The unpaired electron delocalizes throughout the benzene ring as indicated by a *g*-value determined by EPR spectroscopy, that is less than 2.003 with a broad spectrum (Figure 2.7), suggesting a carbon-centered radical.[81,82] The other C−O bond of $-O(C_6H_4O)$ which connects two vanadium atoms together has a bond length of 1.41(3) Å which is slightly longer than the other C−O bond previously described (It is noteworthy that C−OH bond distance in hydroquinone is 1.38 Å).[77,78] This is probably caused by the steric effect between the aromatic ring and the vanadium octahedral chain.

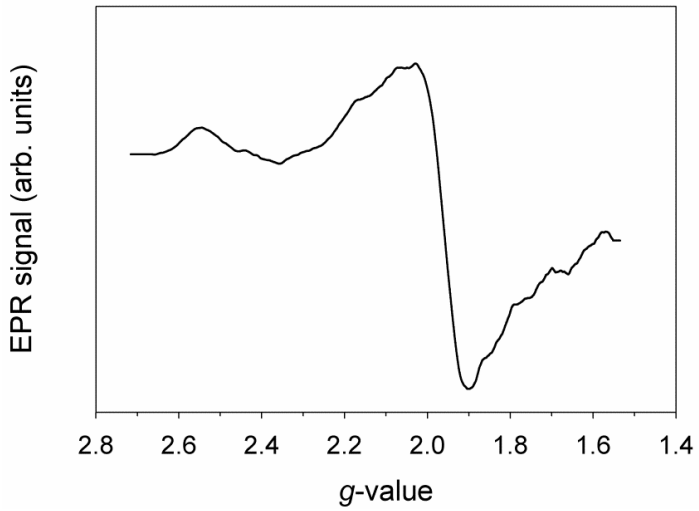

Figure 2.7 EPR spectrum of compound **4** at room temperature.

2.3.5 Temperature-induced Structural Deformations

As mentioned earlier, the compound series MX_2O_4, to which $[V^{IV}(O)(bdc)]$ belongs, can demonstrate significant structural flexibility in response to external stimuli, such as guest molecule uptake, pressure, and temperature with retention of crystallinity.[41] Herein, the discussion is focused on the effect of temperature.

One intriguing feature of the MIL-53/MIL-47 family is the dramatically different breathing behaviors observed for different metal ion centers. As described above, the aluminum analog in the series $[Al^{III}(OH)(bdc)]$, or MIL-53(Al), after framework activation, readily adsorbs water from the atmosphere at room temperature (one mole of water per Al atom) to yield monoclinic MIL-53(Al)$\{H_2O\}$, accompanied by a substantial decrease in channel aperture (closed-pore, *cp*).[37] Upon heating, water is removed and MIL-53(Al)$\{H_2O\}$ transforms into MIL-53(Al)-*lt* (*lt* = low temperature) at 333 K with a monoclinic (*C*2/*c*) narrow-pore (*np*) structure. Further heating causes the pores to open up at 353 K and MIL-53(Al)-*ht* (*ht* = high temperature) is formed. This *ht* phase with an orthorhombic (*Imma*) large-pore (*lp*) structure is stable up to 673 K.[38]

In the case of MIL-53(Al), this reversible flexible character has also been observed to depend on temperature with hysteresis between cooling and heating cycles. The transition from *lp* to *np* occurs in the 125−150 K range on cooling the sample from 450 to 77 K without adsorbing any guest molecules (*lp* at 295 K after heating to 450 K), whereas that from *np* to *lp* occurs in the range of 325−375 K on warming the sample from 77 K (*np* at 295 K after cooling to 77 K).[16,37]

The MIL-53(Cr) or [Cr^{III}(OH)(bdc)] solid exhibits similar breathing behavior as MIL-53(Al), adsorbing one mole of water per Cr atom to yield monoclinic MIL-53(Cr){H_2O}. MIL-53(Cr) adopts either an orthorhombic large-pore (*lp*) form (space group *Imma*; *V* ca. 1490 $Å^3$) that occurs on dehydration and at higher temperatures, or a monoclinic narrow-pore (*np*) form (space group *C*2/*c*; *V* ca. 1020 $Å^3$) at lower temperatures.[28,41]

Another member of the series is MIL-53(Ga) or [Ga^{III}(OH)(bdc)]. After activation, the compound is able to adsorb one mole of water per Ga atom at room temperature under ambient conditions to give MIL-53(Ga){H_2O} with monoclinic $P2_1/c$ symmetry.[38] The water species are trapped within the channels through hydrogen bond interactions with the hydroxyl groups bridging the gallium atoms. The dehydrated form is obtained upon heating the MIL-53(Ga){H_2O} at 353 K resulting in the shrinkage of the channels (unit cell volume decreased by ca. 80 $Å^3$) and the formation of MIL-53(Ga)-*lt* with a narrow-pore (*np*) structure (monoclinic *C*2/*c*), which is retained up to 493 K. At higher temperatures, the open structure MIL-53(Ga)-*ht* with an orthorhombic (*Imma*) large-pore (*lp*) structure (which is isostructural with the high temperature expanded forms of Cr and Al) is formed, before the decomposition temperature at 623 K.[38–40] Compared with the Cr and Al compounds, the stability domain of the narrow-pore (*np*) structure of MIL-53(Ga)-*lt* is larger (ca. 140 K compared to ca. 20 K for Al).[38] It is also worth noting that upon dehydration a narrow pore (*np*) structure is observed for MIL-53(Ga) at room temperature under vacuum, in contrast to well-studied Al- or Cr-based MIL-53 for which the stable phase of the empty structure at room temperature is an open form (*lp*).[38–40]

Boutin et al. also reported a variation of MIL-53(Ga), namely, Ga(OH,F)-MIL-53 where some of the μ_2-OH are replaced by μ_2-F. Despite the small structural difference, it displays a similar breathing behavior to the parent MIL-53(Ga).[40]

Variants with other metals show even more structural complexity; in the case of MIL-53(Fe) or [Fe^{III}(OH)(bdc)], the fully hydrated structure MIL-53(Fe){H_2O} (one water per Fe) corresponds to a monoclinic closed-pore (*cp*) version similar to the hydrated forms mentioned above. The first part of dehydration process removes half of the water molecules (323 K < T < 413 K) resulting in a closing of the structure, and MIL-53(Fe){H_2O} transforms to an intermediate metastable hydrated state MIL-53(Fe)-*int* with triclinic $P\bar{1}$ symmetry, where half of the pores is filled with water molecules and the other half is closed and empty (unit cell volume decreased by ca. 90 $Å^3$). Above 423 K, MIL-53(Fe)-*int* becomes completely anhydrous following by a further small opening of the structure (3 $Å^3$ increase), and [Fe^{III}(OH)(bdc)] or MIL-53(Fe)-*ht* is obtained.[28,32,33] The dehydrated compound adopts a very-narrow-pore (*vnp*) form (monoclinic *C*2/*c* symmetry) with only one type of channel in the structure, which is equivalent to the MIL-53(Ga)-*lt* structure. At higher temperatures, the structure remains closed up to the decomposition temperature at 653 K.[38] The complex hydration-dehydration process of MIL-53(Fe) is reversible.[28]

In addition to MIL-53(Fe), MIL-53(Sc) or [Sc^{III}(OH)(bdc)] also has an unusual breathing transition. Upon removal of the occluded dmf solvent from the as-prepared form, MIL-53(Sc) does not open but instead contracts to give a novel closed-pore (*cp*)

form with monoclinic $P2_1/c$ symmetry, which is distinct from the *vnp* form and any other form adopted by the compounds in the series.[32,41] MIL-53(Sc) is observed to be in the *cp* form in the temperature range of 100−573 K with a gradual expansion of the unit cell volume in response to increasing temperature: the volume increases by 7.4% over the temperature range 100−573 K (cell volume 840 $Å^3$ at 100 K, which is the most contracted structure type observed for MIL-53), and by 623 K it has undergone a transition to a *vnp* form with monoclinic $C2/c$ symmetry with a larger unit cell volume (cell volume 951 $Å^3$ at 623 K) that is isostructural to MIL-53(Fe)-*vnp*.[33,41] The transition complexity of MIL-53(Sc) goes beyond this sensitive response to temperature variation. Hydration of MIL-53(Sc)-*cp* at room temperature, for example, leads to MIL-53(Sc){H_2O} (H_2O:Sc = 0.7:1) with an *int* phase having triclinic symmetry, in which half of the channels are partially open as a result of the uptake of water molecules, while the others are empty and closed, which is similar to the intermediate metastable half-hydrated state of MIL-53(Fe)-*int*.[32,33,41]

In the *cp* structure of MIL-53(Sc) (e.g., at 100 and 293 K), the two opposite Sc μ_2-OH chains corresponding to the short diagonal of the rhombic cross-section of the channel are so close to each other that the hydrogen atom of every hydroxyl group interacts strongly with the nearest oxygen atom of the carboxylate group belonging to the opposite chain. The interatomic distances are 2.05 and 2.15 Å at 100 and 293 K, respectively.[41] In contrast, the formation of such strong and directional hydrogen bonds does not occur in the *vnp* structure (the distance between the pair is 3.8 Å), because of the different alignment of the inorganic chains at 623 K compared with the configuration in

the *cp* structure. The hydrogen bonds formed between the two opposite inorganic chains cause the *cp* structure to be more stable than the *vnp* structure.[41]

In addition to the Al, Cr, Ga, Fe, and Sc members, the vanadium analog is another phase, in which the effect of temperatures on structural transitions has been investigated. In contrast to [V^{IV}(O)(bdc)] traditionally known as MIL-47 where the vanadium ions are tetravalent, Clet and co-workers successfully isolated a vanadium analog in which the vanadium centers are trivalent, designated as MIL-47(V^{III}) or [V^{III}(OH)(bdc)].[42]

Unlike MIL-47(V^{IV}) which was previously reported to remain in an open-pore structure after activation and lack affinity for water, MIL-47(V^{III}) breathes like MIL-53.[42] After activation, MIL-47(V^{III}) adopts an *np* hydrated form with monoclinic *C*2/*c* symmetry in ambient conditions, similar to that observed for MIL-53(Al, Cr, Ga, Fe){H_2O} with one water per vanadium. This is the first striking difference between MIL-47(V^{III}) and MIL-47(V^{IV}) which is known to remain in the *lp* form under the same conditions, and this points out the major role of the oxidation state of the cation.[42] Upon heating to 380 K, MIL-47(V^{III}){H_2O} transforms to an intermediate hydrated state MIL-47(V^{III})-*int* with triclinic symmetry, where half of the pores is filled with water molecules and slightly open, while the other half is closed and empty, similar to MIL-53(Fe)-*int.* Above 420 K, MIL-47(V^{III})-*int* becomes completely anhydrous and monoclinic MIL-47(V^{III})-*cp* is obtained, similar to the one observed for anhydrous MIL-53(Fe).[33] When heated above 480 K, the dehydrated compound MIL-47(V^{III})-*cp* starts to open up, and orthorhombic MIL-47(V^{III})-*lp* is formed. This pore opening may be associated either with

a thermal transformation similar to MIL-53(Al, Cr, and Ga)-*lp*, or to the oxidation of V^{III} to V^{IV}.[42]

To compare the temperature-dependent structural transition behavior of MIL-47(V^{III}) to that of MIL-47(V^{IV}), single crystals of MIL-47(V^{IV}) formulated as [V^{IV}(O)(bdc)] or compound **2** were measured as a function of temperature. As previously reported, upon activation of MIL-47(V^{IV}) by heating to 653 K, the pores of MIL-47(V^{IV}) open up, as the occluded H_2bdc molecules in the channels are removed to form MIL-47(V^{IV})-*ht* with an orthorhombic (*Pnma*) large-pore (*lp*) phase (unit cell volume increased by ca. 80 $Å^3$).[21,22] The large-pore (*lp*) structure of MIL-47(V^{IV})-*ht* is found to remain open even at room temperature without any uptake of water molecules from ambient atmosphere.[21,22] To investigate the structural deformation of MIL-47(V^{IV}) at low temperatures, the measurements were performed in the following temperature sequence: 296, 233, 183, 143, and 100 K. The unit cell parameters change as a function of temperature as shown in Figure 2.8.

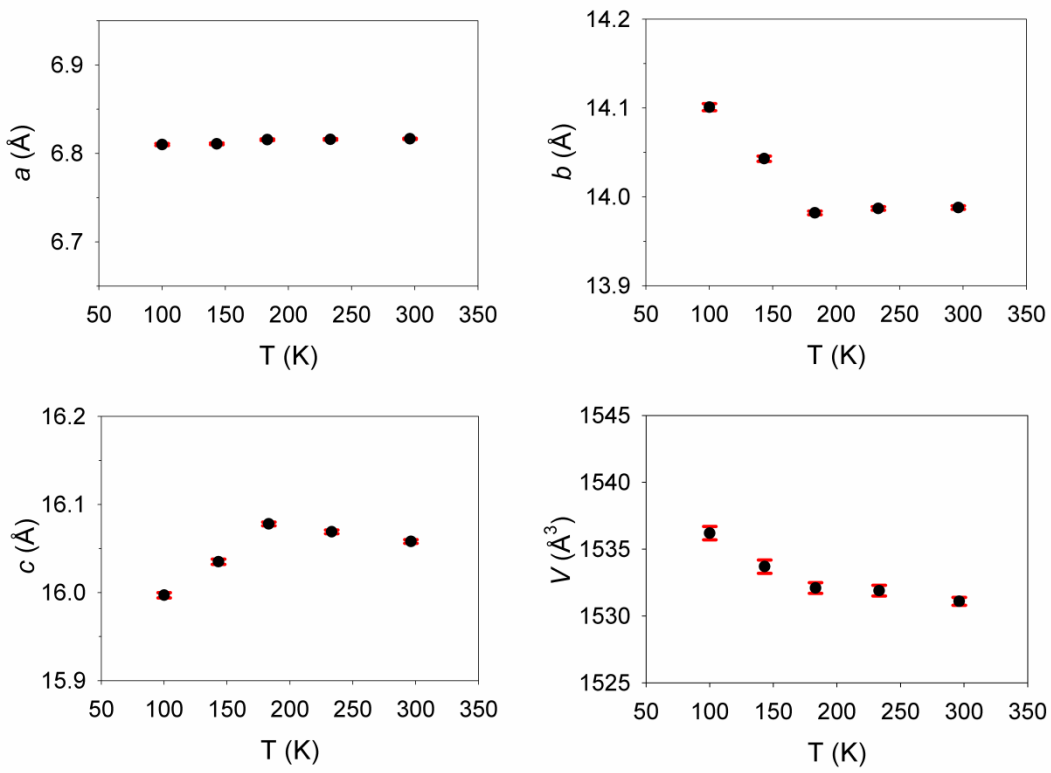

Figure 2.8 Lattice parameters and cell volumes of compound **2**, known as MIL-47(V^{IV}) or [V^{IV}(O)(bdc)], as a function of temperature in the range of 100−296 K (error bars in red).

When MIL-47(V^{IV}) is cooled from room temperature (296 K) down to 100 K, the orthorhombic (*Pnma*) large-pore (*lp*) structure opens up slightly (unit cell volume increases by ca. 8 $Å^3$). As shown in Figure 2.8, the *a* lattice parameters (*a*-axis is the direction along the VO_6 octahedral chain) stay relatively constant, and the *c* lattice parameters decrease very slightly, while those for *b*-axis increase as does the unit cell volume, *V*. This is in contrast to the case of Al and Sc analogs where lowering the

temperature to 77− 100 K causes the pores to close and the unit cell volumes to decrease.[33,37]

Such a striking difference in behavior among the metal ions in response to hydration/dehydration and temperature variation of the MIL-53/MIL-47 family may not be simply explained. Even though the hydrogen bonds (associated to both guest-guest and host-guest O–H interactions) in the hydrated forms play a role, they cannot alone explain the breathing. The most pronounced effect is believed to come from the nature of the metal cation present in the structure.[38]

The effective ionic radius of the metal in octahedral coordination (0.535, 0.615, 0.620, 0.645, 0.745, 0.640, and 0.580 Å for Al^{III}, Cr^{III}, Ga^{III}, Fe^{III} (high spin state), Sc^{III}, V^{III}, and V^{IV}, respectively) may be considered. The larger the radius, the lower the whole stability and the wider the range of stability of the closed-pore form.[38] However, the size of the metal is not sufficient to explain why gallium structure reopens, whereas the iron one does not despite similar sizes. This may suggest that not only the size of the cation plays a role but also its electronic structure. Ga^{III} is diamagnetic ($3d^{10}$) and Fe^{III} is paramagnetic ($3d^5$). In the latter case, magnetic dipolar interactions may be evoked for strengthening the interactions between the chains compared to gallium.[38]

In spite of the similar ionic radii and electronegativities of Cr^{III} and Fe^{III}, the compounds show a very different response toward a simple guest molecule, such as water. The bond distances within the octahedral MO_6 building units are relatively similar: for MIL-53(Fe){H_2O} Fe–O_{av} = 2.00 Å, for MIL-53(Fe)-*int* Fe–O_{av} = 2.00 Å, and for

MIL-53(Fe)-*ht* Fe–O_{av} = 1.99 Å, whereas for MIL-53(Cr){H_2O} Cr–O_{av} = 1.99 Å, and for MIL-53(Cr)-*ht* Cr–O_{av} = 1.95 Å.[28] The –M–O–M–O– chains are disrupted very little upon hydration/dehydration and the small changes in the orientation of the bdc linkers of the two solids could be responsible for the behavior of the framework deformation upon hydration.[28] The flexibility of the structure is restricted to the connection between the inorganic MO_6 chain and the carboxylate functional group of the bdc ligand. Its two oxygen atoms are covalently bound to the carbon atom of the carboxylate but are linked to the metal atoms in the MO_6 chain through ionocovalent bonds. This leads to a possible rotation around the O–O axis of the two planes: O–Cr–O–Cr and O–C–O in case of MIL-53(Cr).[16] Another explanation for the discrepancy between Fe and the other metals, especially Cr, may be related to the electronic configuration of the 3d orbitals of the cations involved in the MIL-53/MIL-47 structure. Fe^{III} has a stable, symmetric half-filled $3d^5$ orbital which is difficult to be perturbed, whereas Cr^{III} possesses a $3d^3$ configuration which is open to accept electrons from the guest molecules.[83]

In case of Ga, the narrow-pore (*np*) form of MIL-53(Ga) is more stabilized than in MIL-53(Al). The more diffuse orbital of Ga^{III} ($3d^{10}$) compared to Al^{III} ($1s^2$ $2s^2$ $2p^6$) is the reason behind the higher stability of its *np* phase, and thus explains why the stability domain of the *np* of MIL-53(Ga)-*lt* is larger (ca. 140 K instead of ca. 20 K for Al) and why MIL-53(Ga) upon dehydration is in *np* form at room temperature (rather than *lp* for Al- or Cr-based MIL-53).[84] The more diffuse nature of the Ga orbitals allows the coordination sphere to deform more; therefore, the bdc linkers can get closer in MIL-

53(Ga) compared to MIL-53(Al). This is believed to be the reason why the *np* phase of MIL-53(Ga) lacks porosity.[84]

For MIL-53(Sc), the additional flexibility causing the unusual closed-pore (*cp*) phase is possibly due to the larger Sc^{III} cation (radius = 0.745 Å) compared to Al^{III}, Cr^{III}, Ga^{III}, Fe^{III}, or V^{III} for which this *cp* form has not yet been reported.[33] If this is the case, a fully dehydrated MIL-53(In) (the effective ionic radius of In^{III} is 0.8 Å) might also be expected to demonstrate a closed-pore (*cp*) structure under the same conditions.[33]

Unlike MIL-47(V^{IV}), MIL-47(V^{III}) is a flexible structure containing μ_2-OH groups. The presence of V^{IV} centers inhibits the flexibility to a large extent. Clet et al. have reported that even with the small amounts of V^{IV} in MIL-47(V^{III} /V^{IV}), they show a dramatic effect on the flexibility.[42] MIL-47(V^{IV}) with a bridging μ_2-oxo group is relatively rigid and remains in an *lp* form both at high temperature and even at low temperature (100 K). This may be explained by the effective ionic radius of the metal ion: 0.640 Å for V^{III} and 0.580 Å for V^{IV}, which is the smallest metal ion among the compound series. As a result, this causes the V–O bond distances of MIL-47(V^{IV}) octahedra to be slightly short (V^{IV}–O_{av} =1.94 Å) with some degree of distortion within the octahedral building units.[22] Presumably, it is believed that not only the size of the cation plays a role but also its electronic structure. V^{III} possesses a $3d^0$ $4s^2$ configuration which is diamagnetic, whereas V^{IV} adopts $3d^0$ $4s^1$ which is paramagnetic. The magnetic interactions may well be responsible for the stability of the structure.

In addition to the studies on breathing behaviors of the traditional MIL-53/MIL-47 frameworks, the effect of additional functional groups have also been investigated. The results show a slightly different flexible behavior due to a complex combination of steric hindrance and intraframework interactions.[83,85] To compare the temperature-induced structural transition of compound **2** or MIL-47(V^{IV}) to that of compound **4**, [V^{III}(O-C_6H_4-O)(bdc)], single crystals of **4** were measured as a function of temperature in the range of 100–296 K (Figure 2.9).

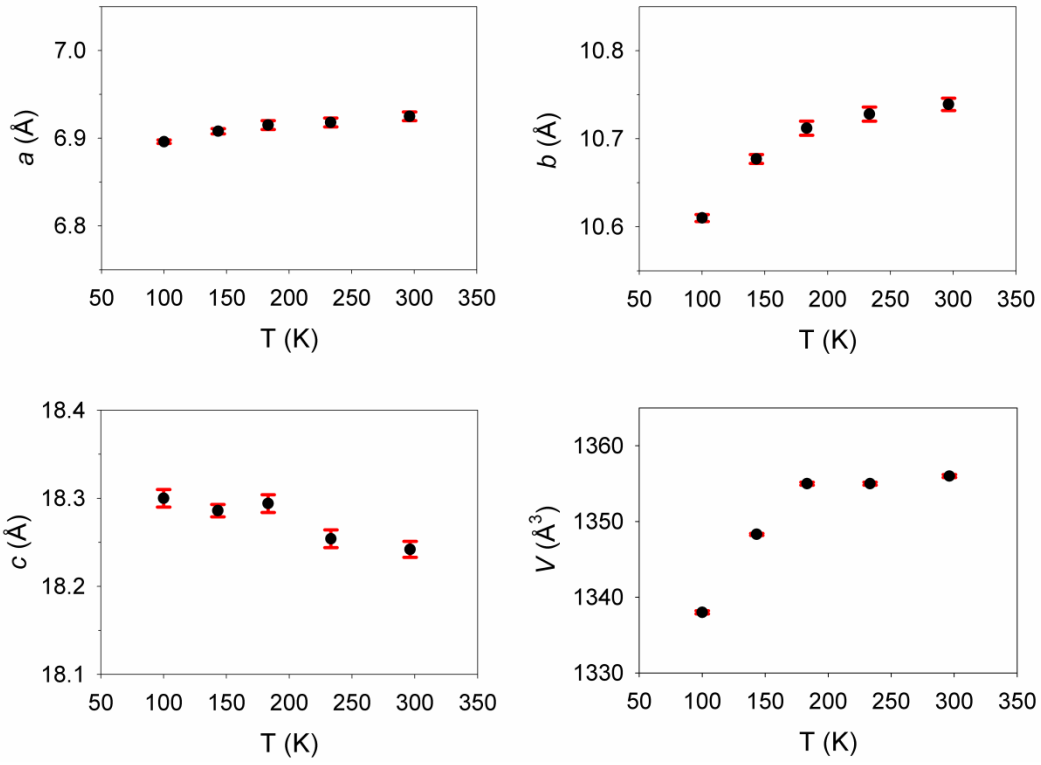

Figure 2.9 Lattice parameters and cell volumes of compound **4**, [V^{III}(O-C_6H_4-O)(bdc)], as a function of temperature in the range of 100–296 K (error bars in red).

When compound **4** is cooled from room temperature (296 K) down to 100 K, the orthorhombic (*Imma*) structure contracts (unit cell volume decreases by ca. 20 $Å^3$). As shown in Figure 2.9, the *a* and *c* lattice parameters stay relatively constant, while the *b* lattice parameters and the unit cell volume, *V* decrease. This is in contrast to the case of compound **2** or MIL-47(V^{IV}) that low temperatures cause the pores to open and the unit cell volumes to increase. This could be due to a combination of the vanadium oxidation state (V^{IV} in compound **2** and V^{III} in compound **4**) and intraframework interactions from the additional functional group. Note that compound **3** was not investigated in order to avoid the effect of quinhydrone guests in the channels on the structural deformation of the framework at low temperatures. In addition to the MIL-53/MIL-47 series, temperature-dependent breathing behaviors have been investigated on other systems as well.[14,86,87]

2.3.6 Thermogravimetric Analysis

TGA measurement of **3** performed from room temperature to 600 °C at 2 °C/min in N_2 flow shows a thermal decomposition in three clearly separated steps between 80 and 460 °C (Figure 2.10a). The first weight loss occurring in the temperature range of 80–130 °C corresponds to the removal of water molecules in the channels (2.15% measured, 2.10% calculated). The second weight loss between 200 and 315 °C corresponds to half (0.38 mol) of the quinhydrone complexes (19.38% measured, 20.15% calculated). The third weight loss between 350 and 460 °C corresponds to the loss of the remaining 0.38 mol of the quinhydrone complexes along with 1 mol of framework bdc

molecules (59.21% measured, 60.03% calculated). The residue was confirmed by PXRD to be V_2O_3. Elemental analysis of **3** also gives a quinhydrone content of 0.76, in accordance with the X-ray data refinement. TGA measurement of **4** performed from room temperature to 950 °C at 2 °C/min in N_2 flow shows no clear thermal decomposition step (Figure 2.10b). The weight loss occurs over the whole temperature range relating to the combustion of the framework.

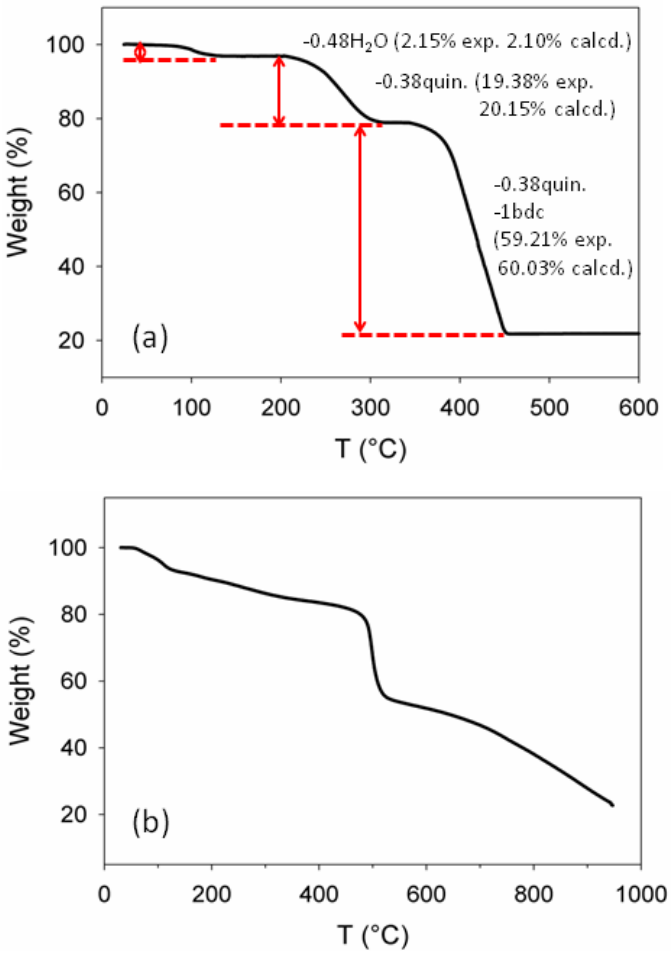

Figure 2.10 Thermogravimetric analyses under a nitrogen flow with a heating rate of 2 °C/min of (a) compound **3** and (b) compound **4**.

2.3.7 FT-IR and PXRD Characterization

The infrared spectrum of compound **3** (Figure 2.11c) shows the vibrational bands characteristic of the framework $-(O-C-O)-$ groups around 1550 and 1430 cm^{-1}, confirming the presence of the dicarboxylate within the solid; a band at ca. 1700 cm^{-1} characteristic of free $-C=O$ groups (as part of the quinhydrone) is also observed for compound **3** but not for compound **2** (Figure 2.11b, shown in comparison with the spectrum of **1**, Figure 2.11a), which is in agreement with the absence of free H_2bdc acid within the pores for this solid.[23] The observed vibrational bands of **3** at 1632 cm^{-1} and in the region 3600–3500 cm^{-1} correspond to the bending and stretching modes of water, respectively.[24] They also overlap with the signature of the hydroxyl group μ_2-OH bridging the vanadium atoms, and the hydroxyl group which is part of the quinhydrone complex, in comparison with the absence of bands in the same region for compound **2**.[24] The infrared spectrum of compound **4** (Figure 2.11d) is quite similar, except for the absence of bands around 3500 cm^{-1}, suggesting that the bridging species is $-O-C_6H_4-O$ and confirming the absence of OH group in the structure.

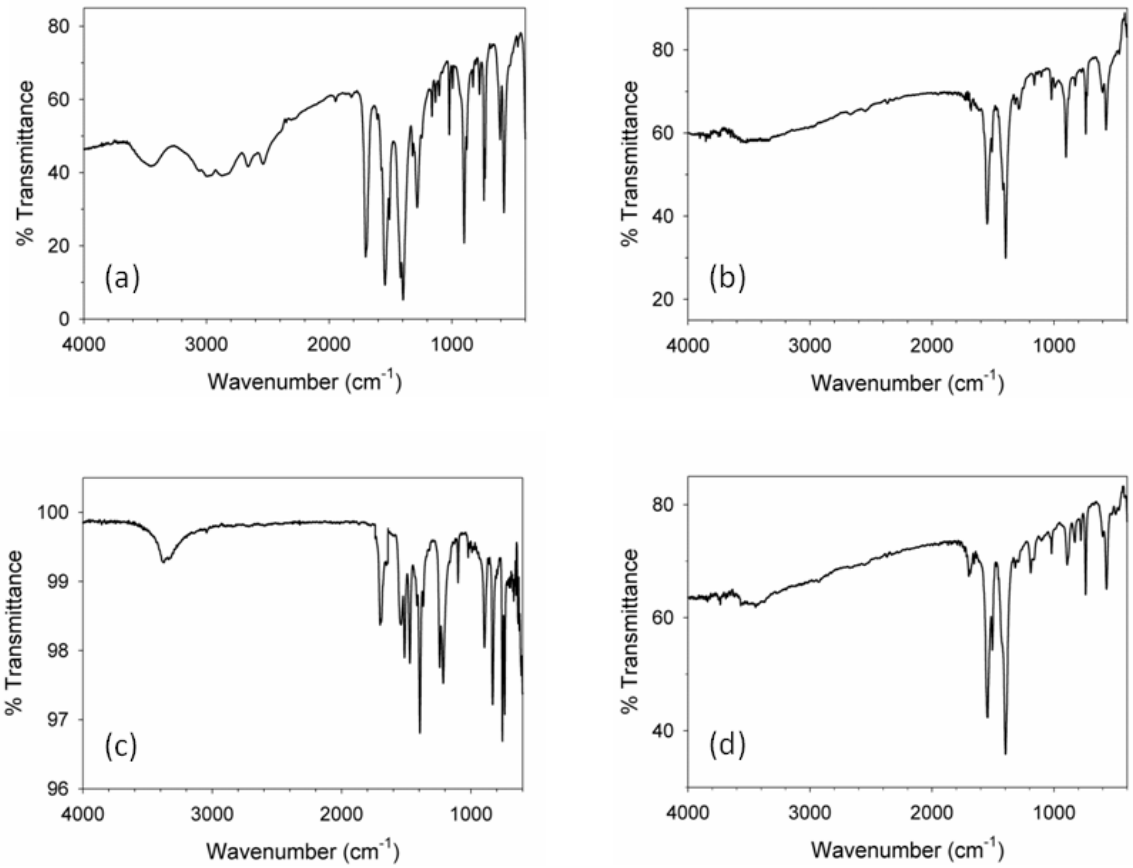

Figure 2.11 From (a) to (d), infrared spectra of compound **1** to **4**, respectively.

Powder XRD data of the compounds are displayed in Figure 2.12. In general, the peak positions on the experimental PXRD patterns are in very good agreement with the simulated patterns. No extra lines are present, indicating the purity of the bulk products. Differences in intensities are most likely due to the preferred orientation of the powdered samples.

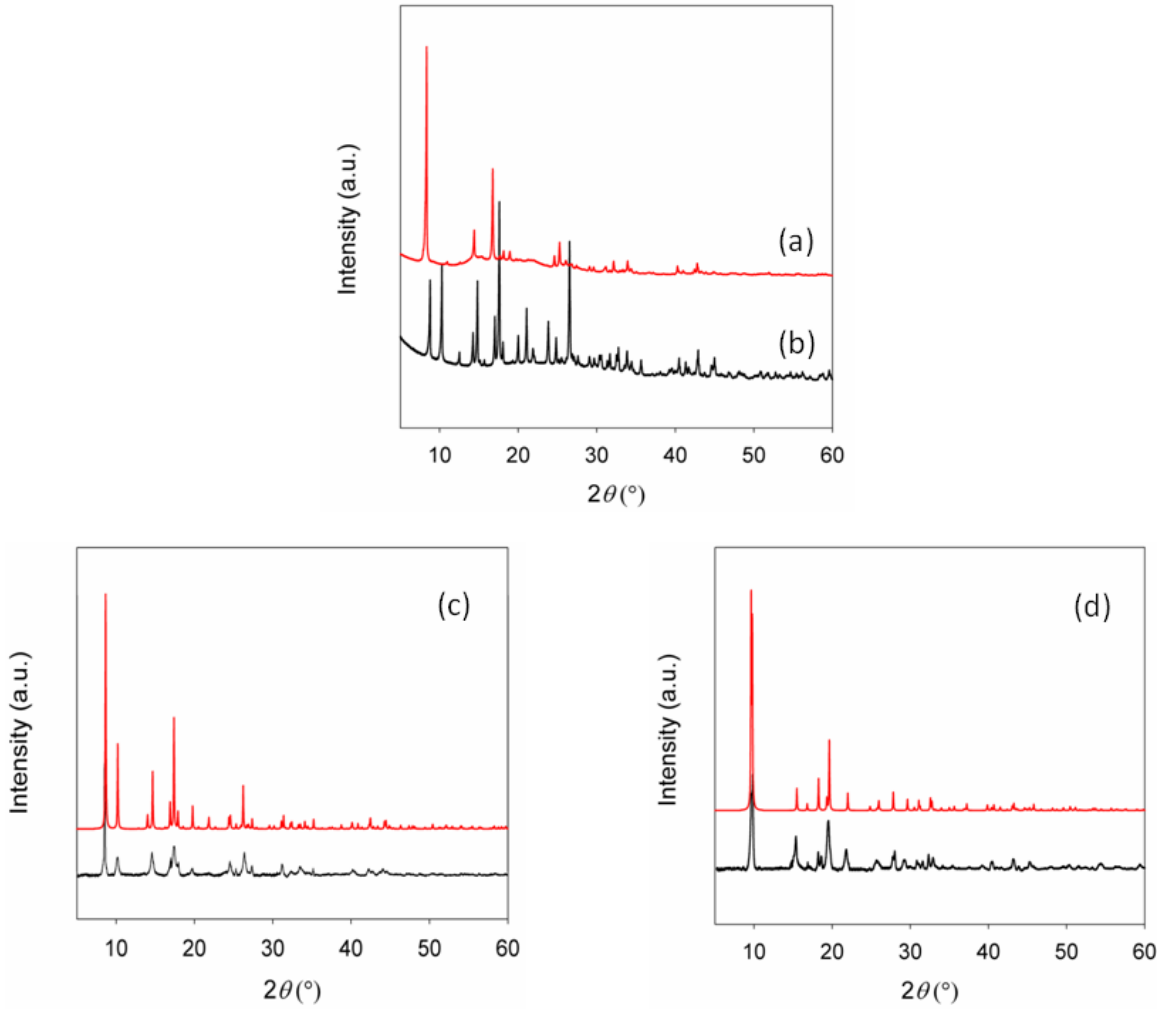

Figure 2.12 Experimental powder X-ray diffraction patterns of **1** (b) and **2** (a). PXRD patterns of compounds **3** and **4** (in red, simulated; in black, experimental) are shown in (c) and (d), respectively.

2.4 Conclusions

We describe an example of redox intercalation using vanadium benzenedicarboxylate, $[V^{IV}(O)(bdc)]$ conventionally denoted as MIL-47, as the host and electroactive hydroquinone as the guest. The single crystals of the as-synthesized $[V^{IV}(O)(bdc)](H_2bdc)_{0.71}$, **1** were heated in air to remove the guest acid molecules. The resulting $[V^{IV}(O)(bdc)]$ structure, **2** was sufficiently flexible and stable to undergo redox intercalation with hydroquinone. The reaction temperatures and especially the atmosphere were found to be the factors that determined the products. In ambient atmosphere, when **2** was heated together with hydroquinone, a quinhydrone charge-transfer complex formed inside the channels and V^{4+} ions were reduced to V^{3+} to yield compound **3**. In addition to the conductivity that could take place along the $\cdots$OH −V− OH −V−$\cdots$ chain, an intermolecular proton-electron transfer reaction of the quinhydrone itself may lead to interesting electrical properties of **3**. Under anhydrous conditions, the $[V^{IV}(O)(bdc)]$ framework (**2**) itself was found to be functionalized by hydroquinone. According to EPR studies, the product from the anhydrous reaction (**4**) was found to contain unpaired electrons, and the *p*-semiquinone radical anion is believed to be the species responsible, with the reduction of V^{4+} to V^{3+} and water as a byproduct.

Moreover, the effect of temperature variation from 296 K to 100 K on the breathing transition of compound **2** was compared to that of **4**. In the case of **2**, low temperatures cause the pores to open and the unit cell volumes to increase, which is in

contrast to the functionalized framework **4**. This could be due to a combination of the oxidation state of the metal ions and intraframework interactions of the additional functional group.

2.5 References

[1] Férey, G. *Chem. Soc. Rev.* **2008**, *37*, 191–214.

[2] Sumida, K.; Rogow, D. L.; Mason, J. A.; McDonald, T. M.; Bloch, E. D.; Herm, Z. R.; Bae, T.-H.; Long, J. R. *Chem. Rev.* **2012**, *112*, 724–781.

[3] Kitagawa, S.; Kitaura, R.; Noro, S.-I. *Angew. Chem., Int. Ed.* **2004**, *43*, 2334–2375.

[4] Li, J.-R.; Kuppler, R. J.; Zhou, H.-C. *Chem. Soc. Rev.* **2009**, *38*, 1477–1504.

[5] Czaja, A. U.; Trukhan, N.; Müller, U. *Chem. Soc. Rev.* **2009**, *38*, 1284–1293.

[6] Lee, J.; Farha, O. K.; Roberts, J.; Scheidt, K. A.; Nguyen, S. T.; Hupp, J. T. *Chem. Soc. Rev.* **2009**, *38*, 1450–1459.

[7] Bétard, A.; Fisher, R. A. *Chem. Rev.* **2012**, *112*, 1055–1083.

[8] Dhakshinamoorthy, A.; Alvaro, M.; Garcia, H. *Chem. Commun*. **2012**, *48*, 11275–11288.

[9] Khajavi, H.; Gascon, J.; Schins, J. M.; Siebbeles, L. D. A.; Kapteijn, F. *J. Phys. Chem. C* **2011**, *115*, 12487–12493.

[10] Fischer, R. A.; Wöll, C. *Angew. Chem., Int. Ed.* **2008**, *47*, 8164–8168.

[11] Férey, G.; Serre, C. *Chem. Soc. Rev.* **2009**, *38*, 1380–1399.

[12] Serre, C.; Mellot-Draznieks, C.; Surblé, S.; Audebrand, N.; Filinchuk, Y.; Férey, G. *Science* **2007**, *315*, 1828–1831.

[13] Sarkisov, L.; Martin, R. L.; Haranczyk, M.; Smit, B. *J. Am. Chem. Soc*. **2014**, *136*, 2228–2231.

[14] Wei, Y.-S.; Chen, K.-J.; Liao, P.-Q.; Zhu, B.-Y.; Lin, R.-B.; Zhou, H.-L.; Wang, B.-Y.; Xue, W.; Zhang, J.-P.; Chen, X.-M. *Chem. Sci*. **2013**, *4*, 1539–1546.

[15] Zeng, M.-H.; Wang, Q.-X.; Tan, Y.-X.; Hu, S.; Zhao, H.-X.; Long, L.-S.; Kurmoo, M. *J. Am. Chem. Soc*. **2010**, *132*, 2561–2563.

[16] Beurroies, I.; Boulhout, M.; Llewellyn, P. L.; Kuchta, B.; Férey, G.; Serre, C.; Denoyel, R. *Angew. Chem., Int. Ed.* **2010**, *49*, 7526–7529.

[17] Beauvais, L. G.; Shores, M. P.; Long, J. R. *J. Am. Chem. Soc*. **2000**, *122*, 2763–2772.

[18] Kepert, C. J. *Chem. Commun*. **2006**, 695–700.

[19] Albrecht, M.; Lutz, M.; Spek, A. L.; Koten, G. V. *Nature* **2000**, *406*, 970–974.

[20] Real, J. A.; Andrés, E.; Munoz, M. C.; Julve, M.; Granier, T.; Bousseksou, A.; Varret, F. *Science* **1995**, *268*, 265–267.

[21] Barthelet, K.; Marrot, J.; Riou, D.; Férey, G. *Angew. Chem., Int. Ed.* **2002**, *41*, 281–284.

[22] Wang, X.; Liu, L.; Jacobson, A. J. *Angew. Chem., Int. Ed.* **2006**, *45*, 6499–6503.

[23] Serre, C.; Millange, F.; Thouvenot, C.; Noguès, M.; Marsolier, G.; Louër, D.; Férey, G. *J. Am. Chem. Soc*. **2002**, *124*, 13519–13526.

[24] Loiseau, T.; Serre, C.; Huguenard, C.; Fink, G.; Taulelle, F.; Henry, M.; Bataille, T.; Férey, G. *Chem. Eur. J*. **2004**, *10*, 1373–1382.

[25] Liu, L.; Wang, X.; Jacobson, A. J. *Dalton Trans*. **2010**, *39*, 1722–1725.

[26] Whitfield, T. R.; Wang, X.; Jacobson, A. J. *Mater. Res. Soc. Symp. Proc*. **2002**, *755*, 191–196.

[27] Whitfield, T. R.; Wang, X.; Liu, L.; Jacobson, A. J. *Solid State Sci.* **2005**, *7*, 1096–1103.

[28] Millange, F.; Guillou, N.; Walton, R. I.; Grenèche, J.-M.; Margiolaki, I.; Férey, G. *Chem. Commun*. **2008**, 4732–4734.

[29] Anokhina, E. V.; Vougo-Zanda, M.; Wang, X.; Jacobson, A. J. *J. Am. Chem. Soc*. **2005**, *127*, 15000–15001.

[30] Vougo-Zanda, M; Huang, J.; Anokhina, E.; Wang, X.; Jacobson, A. J. *Inorg. Chem*. **2008**, *47*, 11535–11542.

[31] Xu, G.; Zhang, X.; Guo, P.; Pan, C.; Zhang, H.; Wang, C. *J. Am. Chem. Soc*. **2010**, *132*, 3656–3657.

[32] Mowat, J. P. S.; Miller, S. R.; Slawin, A. M. Z.; Seymour, V. R.; Ashbrook, S. E.; Wright, P. A. *Microporous Mesoporous Mater.* **2011**, *142*, 322–333.

[33] Mowat, J. P. S.; Seymour, V. R.; Griffin, J. M.; Thompson, S. P.; Slawin, A. M. Z.; Fairen-Jimenez, D.; Düren, T.; Ashbrook, S. E.; Wright, P. A. *Dalton Trans*. **2012**, *41*, 3937–3941.

[34] Wang, X.; Eckert, J.; Liu, L.; Jacobson, A. J. *Inorg. Chem*. **2011**, *50*, 2028–2036.

[35] Férey, G.; Millange, F.; Morcrette, M.; Serre, C.; Doublet, M.-L.; Grenèche, J.-M.; Tarascon, J.-M. *Angew. Chem., Int. Ed.* **2007**, *46*, 3259–3263.

[36] De Combarieu, G.; Morcrette, M.; Millange, F.; Guillou, N.; Cabana, J.; Grey, C. P.; Margiolaki, I.; Férey, G.; Tarascon, J.-M. *Chem. Mater.* **2009**, *21*, 1602–1611.

[37] Liu, Y.; Her, J.-H.; Dailly, A.; Ramirez-Cuesta, A. J.; Neumann, D. A.; Brown, C. M. *J. Am. Chem. Soc*. **2008**, *130*, 11813–11818.

[38] Volkringer, C.; Loiseau, T.; Guillou, N.; Férey, G.; Elkaïm, E.; Vimont, A. *Dalton Trans*. **2009**, 2241–2249.

[39] Chaplais, G.; Simon-Masseron, A.; Porcher, F.; Lecomte, C.; Bazer-Bachi, D.; Bats, N.; Patarin, J. *Phys. Chem. Chem. Phys*. **2009**, *11*, 5241–5245.

[40] Boutin, A.; Bousquet, D. *J. Phys. Chem. C* **2013**, *117*, 8180–8188.

[41] Chen, L.; Mowat, J. P. S.; Fairen-Jimenez, D.; Morrison, C. A.; Thompson, S. P.; Wright, P. A.; Düren, T. *J. Am. Chem. Soc*. **2013**, *135*, 15763–15773.

[42] Leclerc, H.; Devic, T.; Devautour-Vinot, S.; Bazin, P.; Audebrand, N.; Férey, G.; Daturi, M.; Vimont, A.; Clet, G. *J. Phys. Chem. C* **2011**, *115*, 19828–19840.

[43] Graham, A. J.; Banu, A.-M.; Düren, T.; Greenaway, A.; McKellar, S. C.; Mowat, J. P. S.; Ward, K.; Wright, P. A.; Moggach, S. A. *J. Am. Chem. Soc*. **2014**, *136*, 8606–8613.

[44] Wang, Z.; Cohen, S. M. *Chem. Soc. Rev.* **2009**, *38*, 1315–1329.

[45] Kim, H.; Chun, H.; Kim, G.-H.; Lee, H.-S.; Kim, K. *Chem. Commun*. **2006**, 2759–2761.

[46] Givaja, G.; Amo-Ochoa, P.; Gómez-García, C. J.; Zamora, F. *Chem. Soc. Rev.* **2012**, *41*, 115–147.

[47] Hendon, C. H.; Tiana, D.; Walsh, A. *Phys. Chem. Chem. Phys*. **2012**, *14*, 13120–13132.

[48] Silva, C. G.; Corma, A.; García, H. *J. Mater. Chem*. **2010**, *20*, 3141–3156.

[49] Yoon, S. M.; Warren, S. C.; Grzybowski, B. A. *Angew. Chem., Int. Ed.* **2014**, *53*, 4437–4441.

[50] Meilikhov, M.; Yusenko, K.; Torrisi, A.; Jee, B.; Mellot-Draznieks, C.; Pöppl, A.; Fischer, R. A. *Angew. Chem., Int. Ed.* **2010**, *49*, 6212–6215.

[51] Halls, J. E.; Hernán-Gómez, A.; Burrows, A. D.; Marken, F. *Dalton Trans*. **2012**, *41*, 1475–1480.

[52] Meilikhov, M.; Yusenko, K.; Fischer, R. A. *Dalton Trans*. **2010**, *39*, 10990–10999.

[53] Yanai, N.; Uemura, T.; Ohba, M.; Kadowaki, Y.; Maesato, M.; Takenaka, M.; Nishitsuji, S.; Hasegawa, H.; Kitagawa, S. *Angew. Chem., Int. Ed.* **2008**, *47*, 9883–9886.

[54] Meilikhov, M.; Yusenko, K.; Fischer, R. A. *J. Am. Chem. Soc*. **2009**, *131*, 9644–9645.

[55] Himsl, D.; Wallacher D.; Hartmann, M. *Angew. Chem., Int. Ed.* **2009**, *48*, 4639–4642.

[56] Bloch, E. D.; Murray, L. J.; Queen, W. L.; Chavan, S.; Maximoff, S. N.; Bigi, J. P.; Krishna, R.; Peterson, V. K.; Grandjean, F.; Long, G. J.; Smit, B.; Bordiga, S.; Brown, C. M.; Long, J. R. *J. Am. Chem. Soc*. **2011**, *133*, 14814–14822.

[57] Mulfort, K. L.; Hupp, J. T. *J. Am. Chem. Soc*. **2007**, *129*, 9604–9605.

[58] Mulfort, K. L.; Wilson, T. M.; Wasielewski, M. R.; Hupp, J. T. *Langmuir* **2009**, *25*, 503–508.

[59] Bureekaew, S.; Horike, S.; Higuchi, M.; Mizuno, M.; Kawamura, T.; Tanaka, D.; Yanai, N.; Kitagawa, S. *Nat. Mater.* **2009**, *8*, 831–836.

[60] Talin, A. A.; Centrone, A.; Ford, A. C.; Foster, M. E.; Stavila, V.; Haney, P.; Kinney, R. A.; Szalai, V.; Gabaly, F. E.; Yoon, H. P.; Léonard, F.; Allendorf, M. D. *Science* **2014**, *343*, 66–69.

[61] Fuma, Y.; Ebihara, M.; Kutsumizu, S.; Kawamura, T. *J. Am. Chem. Soc*. **2004**, *126*, 12238–12239.

[62] Nagarathinam, M.; Saravanan, K.; Phua, E. J. H.; Reddy, M. V.; Chowdari, B. V. R.; Vittal, J. J. *Angew. Chem., Int. Ed.* **2012**, *51*, 5866–5870.

[63] Li, S.-L.; Xu, Q. *Energy Environ. Sci.* **2013**, *6*, 1656–1683.

[64] Morozan, A.; Jaouen, F. *Energy Environ. Sci.* **2012**, *5*, 9269–9290.

[65] Ameloot, R.; Aubrey, M.; Wiers, B. M.; Gómora-Figueroa, A. P.; Patel, S. N.; Balsara, N. P.; Long, J. R. *Chem. Eur. J.* **2013**, *19*, 5533–5536.

[66] Meilikhov, M.; Yusenko, K.; Esken, D.; Turner, S.; Tendeloo, G. V.; Fischer, R. A. *Eur. J. Inorg. Chem.* **2010**, *2010*, 3701–3714.

[67] Wade, C. R.; Li, M.; Dincă, M. *Angew. Chem., Int. Ed.* **2013**, *52*, 13377–13381.

[68] Leus, K.; Muylaert, I.; Vandichel, M.; Marin, G. B.; Waroquier, M.; Speybroeck, V. V.; Voort, P. V. D. *Chem. Commun.* **2010**, *46*, 5085–5087.

[69] Choi, H. J.; Suh, M. P. *J. Am. Chem. Soc*. **2004**, *126*, 15844–15851.

[70] Han, J. W.; Hill, C. L. *J. Am. Chem. Soc*. **2007**, *129*, 15094–15095.

[71] Rafiee, M.; Nematollahi D. *Electroanalysis* **2007**, *19*, 1382–1386.

[72] Eggins B. R.; Chambers, J. Q. *J. Electrochem. Soc*. **1970**, *117*, 186–192.

[73] Sheldrick, G. M. *SHELXTL: Program for Refinement of Crystal Structures;* Siemens Analytical X-ray Instruments: Madison, WI, 1994.

[74] Gouws, S.; Barton, B.; Loyson, P. L. R.; Zeelie, B. *Electrochim. Acta* **2008**, *53*, 4544–4549.

[75] González Moa, M. J.; Mandado, M.; Mosquera, R. A. *J. Phys. Chem. A* **2007**, *111*, 1998–2001.

[76] Brese, N. E.; O'Keeffe, M. *Acta Crystallogr.* **1991**, *B47*, 192–197.

[77] Sakurai, T. *Acta Crystallogr*. **1965**, *19*, 320–330.

[78] Sakurai, T. *Acta Crystallogr*. **1968**, *B24*, 403–411.

[79] Nakasuji, K.; Sugiura, K.; Kitagawa, T.; Toyoda, J.; Okamoto, H.; Okaniwa, K.; Mitani, T.; Yamamoto, H.; Murata, I.; Kawamoto, A.; Tanaka, J. *J. Am. Chem. Soc*. **1991**, *113*, 1862–1864.

[80] Truong, H.; Lomnicki, S.; Dellinger, B. *Chemosphere* **2008**, *71*, 107–113.

[81] Molčanov, K.; Kojić-Prodić, B.; Roboz, M. *Acta Crystallogr*. **2006**, *B62*, 1051–1060.

[82] Adounkpe, J.; Khachatryan, L.; Dellinger, B. *Energy Fuels* **2008**, *22*, 2986–2990.

[83] Devic, T.; Horcajada, P.; Serre, C.; Salles, F.; Maurin, G.; Moulin, B.; Heurtaux, D.; Clet, G.; Vimont, A.; Grenèche, J.-M.; Ouay, B. L.; Moreau, F.; Magnier, E.; Filinchuk, Y.; Marrot, J.; Lavalley, J.-C.; Daturi, M.; Férey, G. *J. Am. Chem. Soc*. **2010**, *132*, 1127–1136.

[84] Coudert, F. X.; Ortiz, A. U.; Haigis, V.; Bousquet, D.; Fuchs, A. H.; Ballandras, A.; Weber, G.; Bezverkhyy, I.; Geoffroy, N.; Bellat, J.-P.; Ortiz, G.; Chaplais, G.; Patarin, J.; Boutin, A. *J. Phys. Chem. C* **2014**, *118*, 5397–5405.

[85] Serra-Crespo, P.; Gobechiya, E.; Ramos-Fernandez, E. V.; Juan-Alcaniz, J.; Martinez-Joaristi, A.; Stavitski, E.; Kirschhock, C. E. A.; Martens, J. A.; Kapteijn, F.; Gascon, J. *Langmuir* **2012**, *28*, 12916–12922.

[86] Yang, C.; Wang, X.; Omary, M. A. *Angew. Chem., Int. Ed.* **2009**, *48*, 2500–2505.

[87] Fernandez, C. A.; Thallapally, P. K.; McGrail, B. P. *ChemPhysChem* **2012**, *13*, 3275–3281.

Chapter 3

Exploration of Vanadium Benzenedicarboxylate as a Cathode for Rechargeable Lithium Batteries

3.1 Introduction

Recent research and commercial development of batteries have focused on electrode materials with higher operating voltage and energy density, long cycle life, and rate capability for use in portable electronic devices, electric vehicles, and large-scale energy storage units for the power grid.[1–4] A wide range of compounds, such as $LiMPO_4$ (M = Fe, Mn, or Co),[5] $Li_3M_2(PO_4)_3$,[6] Li_2MSiO_4,[7,8] $LiMSO_4F$,[9,10] $LiMBO_3$ (M = Fe, V, Mn, Co, etc.),[11] $Li_7Mn(BO_3)_3$,[12] $LiVOPO_4$,[13,14] $LiVPO_4F$,[15,16] and $Li_2FeP_2O_7$ have been examined as cathode materials for rechargeable lithium batteries.[17–20] In addition to these inorganic compounds, new organic materials, such as $Li_2C_8H_4O_4$,[21] $Li_2C_6H_4O_4$,[21] $Li_2(C_6H_2O_4)$,[22] $Li_2(C_{14}H_6O_4)$,[23] $Li_4(C_6O_6)$,[24] and $Li_4C_{24}H_8O_8$ have shown promise as electrode materials for Li-ion batteries.[25–28]

Another class of crystalline materials, metal-organic frameworks (MOFs), assembled from inorganic building units (metal ions or clusters) and organic linkers, has also emerged as novel electrode materials for rechargeable lithium batteries.[29,30] Due to the design and synthesis flexibility inherent in MOFs,[31–33] in the past two decades many efforts have been made to address technological applications of these materials in areas, such as gas storage, separations, ion exchange, catalysis, selective molecular adsorption, optoelectronics, magnetic and photoluminescence responses, and drug delivery.[34–39]

MOFs have attracted attention as possible candidates for a new class of electrodes because they possess tunable, porous open channels that allow rapid insertion of species, and redox active metal centers, which can be easily controlled by changing the organic ligand molecules and metal ions.[40]

Among the numerous properties which can be found in porous organic-inorganic frameworks, MOFs still face a number of challenges in the area of redox chemistry and electrical properties, particularly because of their insulating nature.[41–44] Changes in the redox state of the metal centers are usually accompanied by changes in the coordination number of the metal ion, which can lead to a non-reversible degradation of the MOF structure.[45,46] Up to 2006, there had been only three reports of using MOFs as energy-storage electrodes for lithium batteries. None of them was successful. The first attempt was on electrochemical reduction of a microporous nickel phosphate by Li which resulted in the irreversible decomposition of the compound into a nanocomposite electrode made of Ni nanoparticles embedded in a Li_2O matrix.[47] A second example was the Ga-V phosphonate framework containing redox active oxovanadyl centers, with preliminary cycling data revealing that voltage as high as 5 V vs Li/Li^+ was needed to extract the inserted Li^+ ions from the structure.[48] The third reported by Li and co-workers was the study on the electrochemical Li intercalation of a Zn-based MOF. The result showed a relatively high irreversible capacity during the first discharge and a much lower reversible charge-discharge capacity in the following cycles. The precursor decomposed into a Zn-based nanocomposite matrix containing Li_2O. The authors claimed that this material was “not suitable for application in reversible lithium storage”.[49]

One way to bypass these poorly reversible conversion/decomposition reactions is to use MOFs that are based on early 3d transition metals to take advantage of the lower occupation of 3d electron orbitals (higher oxidation states of the metals), which leads to greater M−O bond stability with respect to charge variations, and to bring about some long-range electron delocalization via the stabilization of class II and III mixed valence states.[50] Recently, Férey and co-workers synthesized a wide variety of 3d metal (V^{III}, Cr^{III}, Fe^{III}) carboxylates, which belong to a group of compounds with the general framework formula MX(bdc), based on chains of *trans* corner-sharing MX_2O_4 (M = V,[51,52] Cr,[53] Al,[54,55] Fe,[56–58] In,[59] Ga,[60] Mn,[61] and Sc,[62,63] with X = O, OH, F) octahedra cross-linked by 1,4-benzenedicarboxylate (bdc). The three-dimensional framework that results has one-dimensional rhombic channels. The first member of the compound series $[V^{III}(OH)(bdc)](H_2bdc)_x$, known as MIL-47as, loses the guest acid on heating in air, and simultaneously the framework V^{3+} ions are oxidized to V^{4+} forming $V^{IV}(O)(bdc)$ or MIL-47, without changing the topology of the structure, thus providing the first evidence of chemically induced redox reactions within this system.[51]

In addition to the oxidative removal of H_2bdc from MIL-47as, Jacobson and co-workers synthesized two iron members of the family, namely, $[Fe^{III}(OH)(bdc)](py)_{0.85}$ and $[Fe^{II}(bdc)(dmf)]$ (py = pyridine and dmf = dimethylformamide), where the change in the iron oxidation state is brought about by replacing the OH^- bridging species by the neutral oxygen atom in dmf.[57] This provides the first example of a M^{II} analog with the bridging species along the inorganic chains being neutral. Such findings suggest a possibility of inducing mixed valence states in this MOF family.

In 2007, the first example of MOFs as promising intercalation electrodes in Li-based batteries was reported.[50] An iron compound with composition $[Fe^{III}(OH)_{0.8}F_{0.2}(bdc)](H_2O)$, known as MIL-53, was used as a cathode for a Li-based electrochemical cell. Reversible Li insertion/extraction to the extent of ~0.6 Li^+ per Fe accompanied by reduction/oxidation of Fe^{3+} and Fe^{2+}, with a charge-discharge capacity of 75 mAh/g at a *C*/40 rate (one equivalent Li in 40 h) without any alteration of the framework, was reported. An attempt to increase the electrochemical capacity was made through the adsorption of an electroactive molecule, 1,4-benzoquinone, into the MIL-53 framework.[64] The overall benefit of the quinone uptake was an increase in the electrode capacity from 75 mAh/g to 93 mAh/g, which could not be maintained for longer than 5 cycles. Even though insertion of 2 more Li^+ per mole of 1,4-benzoquinone is possible in principle compared to the parent MIL-53(Fe), practically this could not be achieved due to the solubility of the guest molecule in the electrolyte.

Following the same approach, an iron-based MOF designated as MIL-68, $[Fe^{III}(OH)(bdc)](dmf)_{1.1}$, which has larger and more rigid (compared to the rhombic channels of MIL-53) triangular and hexagonal one-dimensional pores, was electrochemically investigated for lithium insertion. Surprisingly, only 0.35 Li^+ per Fe could be inserted into the structure corresponding to a capacity of 30 mAh/g at a *C*/10 cycling rate.[65]

Lithium storage by a formate-based MOF, $Zn_3(HCOO)_6$, was reported.[66] An incredibly high capacity of 560 mAh/g corresponding to 9.6 moles of Li was obtained for up to 60 cycles at 0.11*C* within the voltage range of 0.005− 3.0 V. Metal formate frameworks were found to react reversibly with Li through a conversion reaction. The matrix involved during discharge-charge cycling was lithium formate rather than the typical Li_2O. Also, the same authors reported the electrochemistry of $Co_3(HCOO)_6$ and $Zn_{1.5}Co_{1.5}(HCOO)_6$ with lithium metal.[66]

In other studies, Devic and co-workers used MOFs based on the redox active organic linker tetrathiafulvalene tetracarboxylic acid, $(TTF\text{-}TC)H_4$, as the positive electrodes in lithium batteries. The TTF-based compounds, namely, $M_2(TTF\text{-}TC)H_2$ (M = K, Rb, Cs), denoted MIL-132(K), MIL-133(K), MIL-133(Rb) and MIL-134(Cs), exhibited a similar behavior in solid state cyclic voltammetry and galvanostatic charge-discharge experiments. When MIL-132(K) was used as cathode material in a lithium cell, a reversible cyclability was achieved at high current density (10*C*) with a reasonable capacity of 50 mAh/g, corresponding to 0.6 Li insertion for the voltage range between 2.3 and 3.75 V.[67] Another series of TTF-based MOFs, $[M(H_2O)_4]_2(TTF\text{-}TC)(H_2O)_4$ (M = Ni, Co) labeled MIL-136(Ni) and MIL-136(Co), and $[Ni_2(H_2O)_5(TTF\text{-}TC)(H_2O)$ labeled MIL-136′(Ni), were also investigated as positive electrode materials in lithium cells. These compounds exhibited reversible charge-discharge profile at constant 10*C* current density between the voltage range of 2.0− 4.3 V with a capacity about 20 mAh/g corresponding to ~0.6 Li insertion.[68]

Honma et al. reported the use of Prussian blue analogs (PBAs), $A_xMn^{II}_y[Fe^{III}(CN)_6]\cdot nH_2O$ (A = K, Rb), as electrode materials exhibiting reversible lithium insertion/extraction with a capacity of about 60 mAh/g in the voltage range of 2.0−4.3 V at a constant current density of 50 mA/g.[69] The result suggests that the valence state of Mn ions is constant at 2+ and that the Fe ions are redox active during the charge-discharge process.[70,71] Okubo et al. demonstrated that the ion storage ability of the cyanide-bridged MOF, $K_2Mn^{II}[Mn^{II}(CN)_6]$, can be enhanced by suppressing vacancy formation within the framework. Once the K^+ ions are completely removed electrochemically, a vacancy-free PBA framework $Mn^{III}[Mn^{III}(CN)_6]$ can be fabricated. The vacancy-free PBA compound underwent reversible Li-ion intercalation/deintercalation with a capacity of ~197 mAh/g in the voltage range of 2.0−4.2 V at a constant current density of 30 mA/g.[72] Following the same line, $K_{0.14}Cu^{II}_{1.43}[Fe^{III}(CN)_6]\cdot 5H_2O$ was used as cathode material in a lithium cell in the voltage range of 2.0−4.3 V. The result suggests that the insertion of Li ions in CuFe-PBA is accompanied by a reversible redox reaction of both Fe and Cu ions.[73] Furthermore, Talham and co-workers reported Prussian blue analog core-shell particle hetero-structures as the cathode material for Li-ion storage, consisting of a high-capacity $K_{0.1}Cu[Fe(CN)_6]_{0.7}\cdot 3.8H_2O$ core and lower capacity but highly stable shell of $K_{0.1}Ni[Fe(CN)_6]_{0.7}\cdot 4.1H_2O$.[74] The capacity of 99 mAh/g corresponds to one Li per $[Fe(CN)_6]^{3-/4-}$ in both the CuFe-PBA core and the NiFe-PBA shell, plus 0.6 Li per $Cu^{2+/+}$ site in the core (Ni^{2+} in the NiFe-PBA shell is not reduced). The cycling stability of the core@shell particles was found to be much better than that of the uncoated CuFe-PBA.[75]

It is worth noting that PBAs are well-known redox active materials, and their properties have been well-studied in other types of electrochemical systems as well.[40,76–79]

In addition to those MOFs mentioned above, metal organic-phosphate frameworks, namely, $K_{2.5}[(VO)_2(HPO_4)_{1.5}(PO_4)_{0.5}(C_2O_4)]$, $Na_2[(VO)_2(HPO_4)_2(C_2O_4)]$, and $KLi[(VO)_2(HPO_4)_2(C_2O_4)]$, were also investigated for lithium storage. At a current density of 40 mA/g or 0.3*C* within the voltage window of 2.5−4.6 V, the compounds were able to exhibit similar voltage profiles with a reversible capacity for lithium uptake of 66, 55, and 60 mAh/g, respectively.[80]

Wang and co-workers recently reported the use of Mn-based layered MOF, formulated as $[Mn(tfbdc)(4,4'\text{-bpy})(H_2O)_2]$ (tfbdc = 2,3,5,6-tetrafluoroterephthalate, 4,4′-bpy = 4,4′-bipyridine), as electrode material. The compound exhibited an irreversible high capacity which dropped rapidly during the first few cycles. From the fourth cycle, the electrodes maintained a stable reversible capacity of ~390 mAh/g in the voltage range of 0.01−2.5 V at 50 mA/g. The Mn-based MOF was believed to react with Li through a conversion reaction during discharge, leading to formation of Mn and Li_2(tfbdc)(4,4′-bpy).[81]

Another variation of Prussian blue analogs (PBAs), $[Mn(H_2O)][Mn(HCOO)_{2/3}(H_2O)_{2/3}]_{3/4}[Mo(CN)_8]\cdot H_2O$, reported by Okubo et al. with a octacyanometallate-bridged structure exhibited electrochemical Li-ion insertion/extraction with high durability. Approximately 0.52 Li could be inserted/extracted reversibly in the range of 3.0−4.3 V at a constant current density of 10

mA/g with reversible specific capacity of ca. 30 mAh/g, corresponding to the solid state redox reaction of the $[Mo^{V}(CN)_8]^{3-}/[Mo^{IV}(CN)_8]^{4-}$ couple.[82]

Gou et al. investigated another three-dimensional framework, $Co_2(OH)_2(bdc)$, as an anode material for lithium-ion batteries. This compound exhibited good stability as well as a high reversible capacity of ca. 650 mAh/g at a current density of 50 mA/g within the voltage range of $0.02-3.0$ V.[83] The metal-organic frameworks used as electrode materials in Li batteries which, to the best of our knowledge, have been reported up to now are summarized in Table 3.1.

Table 3.1 Summary of Metal-Organic Frameworks Reported as Electrode Materials in Rechargeable Lithium Batteries

Formula	Compound	Voltage (V vs Li/Li^+)	Current density	Capacity (mAh/g)	Mechanism	Reference
$[Fe^{III}(OH)_{0.8}F_{0.2}(bdc)](H_2O)$	MIL-53(Fe)	1.5−3.5	*C*/40	75	intercalation	50,64
$[Fe^{III}(OH)(bdc)](dmf)_{1.1}$	MIL-68(Fe)	1.5−3.5	*C*/10	30	intercalation	65
$Zn_3(HCOO)_6$	FOR1	0.005−3.0	0.11*C*	560	conversion	66
$Co_3(HCOO)_6$	FOR3	0.005−3.0	0.11*C*	410	conversion	66
$Zn_{1.5}Co_{1.5}(HCOO)_6$	FOR4	0.005−3.0	0.11*C*	510	conversion	66
$K_2(TTF\text{-}TC)H_2$	MIL-132(K)	2.3−3.75	10*C*	50	intercalation	67
$K_2(TTF\text{-}TC)H_2$	MIL-133(K)	2.3−3.75	10*C*	30	intercalation	67
$Rb_2(TTF\text{-}TC)H_2$	MIL-133(Rb)	2.3−3.75	10*C*	50	intercalation	67
$Cs_2(TTF\text{-}TC)H_2$	MIL-134(Cs)	2.3−3.75	10*C*	45	intercalation	67
$[Ni(H_2O)_4]_2(TTF\text{-}TC)(H_2O)_4$	MIL-136(Ni)	2.0−4.3	10*C*	20	intercalation	68
$[Co(H_2O)_4]_2(TTF\text{-}TC)(H_2O)_4$	MIL-136(Co)	2.0−4.3	10*C*	20	intercalation	68
$[Ni_2(H_2O)_5(TTF\text{-}TC)(H_2O)$	MIL-136′(Ni)	2.0−4.3	10*C*	20	intercalation	68
$Rb_xMn^{II}_y[Fe^{III}(CN)_6]\cdot nH_2O$		2.0−4.3	50 mA/g	60	intercalation	69,70,71
$K_xMn^{II}_y[Fe^{III}(CN)_6]\cdot nH_2O$		2.0−4.3	50 mA/g	60	intercalation	69,70,71
$Mn^{III}[Mn^{III}(CN)_6]$		2.0−4.2	30 mA/g	197	intercalation	72
$K_{0.14}Cu^{II}_{1.43}[Fe^{III}(CN)_6]\cdot 5H_2O$		2.0−4.3	−	−	intercalation	73
$K_{0.1}Cu[Fe(CN)_6]_{0.7}\cdot 3.8H_2O$ @ $K_{0.1}Ni[Fe(CN)_6]_{0.7}\cdot 4.1H_2O$		2.5−4.3	10 mA/g	99	intercalation	74,75
$K_{2.5}[(VO)_2(HPO_4)_{1.5}(PO_4)_{0.5}(C_2O_4)]$		2.5−4.6	40 mA/g	65	intercalation	80
$Na_2[(VO)_2(HPO_4)_2(C_2O_4)]$		2.5−4.6	40 mA/g	55	intercalation	80
$KLi[(VO)_2(HPO_4)_2(C_2O_4)]$		2.5−4.6	40 mA/g	60	intercalation	80
[Mn(tfbdc)(4,4′-bpy)$(H_2O)_2$]		0.01−2.5	50 mA/g	390	conversion	81
$[Mn(H_2O)][Mn(HCOO)_{2/3}(H_2O)_{2/3}]_{3/4}[Mo(CN)_8]\cdot H_2O$		3.0−4.3	10 mA/g	30	intercalation	82
$Co_2(OH)_2(bdc)$		0.02−3.0	50 mA/g	650	−	83

* bdc = 1,4-benzenedicarboxylate; dmf = dimethylformamide; TTF-TC = tetrathiafulvalene tetracarboxylate; tfbdc = 2,3,5,6-tetrafluoroterephthalate; 4,4′-bpy = 4,4′-bipyridine. Note that several MOFs have also been used as sacrificial precursors to form transition metal oxide nanoparticles upon calcination for battery electrode materials.[4,84–87] Furthermore, the uses of MOFs in Li-O_2 and Li-S batteries have been reported.[88–92]

In the context of the previous work on metal-organic frameworks, we have investigated a vanadium-based compound, $V^{IV}(O)(bdc)$ or MIL-47,[51,52] which is based on an early 3d transition metal and isostructural to MIL-53(Fe), belonging to the compound series MX(bdc). Previously, we have reported the direct synthesis of large single crystals of $[V^{IV}(O)(bdc)](H_2bdc)_{0.71}$.[52] After removal of the guest acid molecules by heating the crystals of $[V^{IV}(O)(bdc)](H_2bdc)_{0.71}$ in air, the $V^{IV}(O)(bdc)$ structure is sufficiently flexible to undergo single-crystal-to-single-crystal transformations upon adsorption of organic guest molecules (e.g., aniline, thiophene, and acetone), enabling the details of the guest structures, framework-guest interactions, and framework deformations upon removal or adsorption of guest species to be determined.[52,93] The ability to accommodate guest molecules inside the pores, which possibly leads to migration pathways for Li^+ ions, together with the redox active metal centers of $V^{IV}(O)(bdc)$ motivated us to investigate this MOF as a rechargeable intercalation electrode in Li-based batteries.

3.2 Experimental Section

3.2.1 Synthesis

Polycrystalline $V^{IV}(O)(bdc)$ was chosen to be used for the investigation on lithium intercalation. The small particle size helps provide large contact area between the active material and the electrolyte used. All chemicals used in this work were reagent grade and used as received from commercial sources without further purification. $V^{IV}(O)(bdc)$ powder was prepared under synthetic conditions as previously reported[94] with some minor variations. The reactants, vanadyl sulfate $VOSO_4 \cdot nH_2O$ and diammonium benzenedicarboxylate $(NH_4)_2bdc$, were heated overnight at 80 °C before use. 2.0 mmol (0.43 g) of $VOSO_4 \cdot nH_2O$ and 2.0 mmol (0.40 g) of $(NH_4)_2bdc$ were then transferred to a round bottomed flask fitted with a condenser, together with 20 mL of dimethylformamide (dmf) which had been dried over molecular sieves prior to the reaction. The mixture was heated at reflux with stirring at 160 °C for 3 d using an oil bath. A yellow brown powder was precipitated from the solution, filtered, washed with methanol, and then dried under vacuum at 80 °C for 12 h. The product was confirmed to be $V^{IV}(O)(bdc)$ without extra guest acid molecules in the channels, unlike that obtained from the hydrothermal synthesis (at 220 °C) which is in the form of large single crystals of $[V^{IV}(O)(bdc)](H_2bdc)_{0.71}$ requiring further calcination.[52] This method yields powder $V^{IV}(O)(bdc)$ with pores that are empty and ready for guest intercalation without further framework activation before use. This synthesis was developed at lower reaction temperature and at one atmosphere pressure to eliminate the need for pressure vessels in scale-up.

The formation of $Li_xV(O)(bdc)$ by intercalation was investigated between $x = 0.1$ and $x = 2$ by two different methods: (1) chemical reaction at ambient temperature under an argon atmosphere between V(O)(bdc) and *n*-butyllithium (LiC_4H_9) in hexane as the reducing agent, and (2) in electrochemical cells.

3.2.2 Chemical Intercalation

To prepare $Li_xV(O)(bdc)$, an appropriate amount of 1.6 M *n*-butyllithium (LiC_4H_9) in hexane was added to V(O)(bdc) powder under an argon atmosphere, and the resulting mixture was stirred at room temperature for a period of 3−48 h; longer times were used for larger values of x in $Li_xV(O)(bdc)$. The product of the reaction was isolated by filtration, washed with hexane to remove traces of unreacted reagent and byproducts, and dried under vacuum at room temperature. The filtrate and washings were combined and mixed with 25 mL of water. The extent of lithium intercalation was determined quantitatively by titrating the liquid mixture with a standardized aqueous HCl solution. Equilibration of the solid with a non-aqueous electrolyte solution containing Li^+ ions, 1 M $LiPF_6$ in ethylene carbonate (EC)/dimethyl carbonate (DMC) solution (1/1 by weight), for 24 h inside an argon-filled glovebox was used to ensure product homogeneity.

3.2.3 Electrochemical Studies

The electrochemical charge-discharge properties of V(O)(bdc) were determined using a multichannel potentiostat-galvanostat MacPile system (Biologic SA, Claix, France) at different current densities between 4.0 and 1.7 V vs Li/Li^+ in 2032 coin cells.

Coin Cells. In a standard coin cell, the positive electrode consisted of 65 wt% V(O)(bdc), 30 wt% acetylene carbon black, and 5 wt% polyvinylidene fluoride (PVdF) binder. The mixture was ground in an agate mortar and solvent-cast onto a 16-mm-diameter stainless steel disc using N-methyl-2-pyrrolidinone (NMP). The electrodes were then dried under vacuum at 100 °C for 12 h (1 mg of active electrode material). The cells had a lithium metal negative electrode separated from the positive electrode by a Whatman borosilicate glass fiber sheet (separator) saturated with 1 M $LiPF_6$ in ethylene carbonate (EC)/dimethyl carbonate (DMC) solution (1/1 by weight), which was used as the electrolyte. The cells were assembled in an argon-filled glovebox. Electrochemical testing conditions are specified in the Results and Discussion section.

3.2.4 Materials Characterization

Phase analysis and determination of unit cell parameters were performed using powder X-ray diffraction (XRD) with a Phillips PANalytical X'Pert PRO diffractometer with Cu Kα radiation (λ = 1.54046 Å) at room temperature. PXRD analyses of $Li_xV(O)(bdc)$ were performed in a sealed sample holder to avoid any contact with air. Extraction of the peak positions, pattern indexing, and profile refinements were carried out using GSAS.

3.3 Results and Discussion

3.3.1 Synthesis

Polycrystalline $V^{IV}(O)(bdc)$ can be prepared by the reflux method described. The reactants $VOSO_4 \cdot nH_2O$, $(NH_4)_2bdc$, and dmf have to be dried prior to use. When the starting materials are added to the reaction flask, a dark blue solution is formed. As the reflux continues at 160 °C, yellow powder is precipitated from the solution together with a green byproduct which can be removed by washing with methanol. The removal of the impurity phase was monitored by powder XRD and disappearance of the green color of the filtrate after the washing. The methanol-washed sample was dried overnight under vacuum at 80 °C to give the open microporous structure shown in Figure 3.1. The product was confirmed by powder XRD to be $V^{IV}(O)(bdc)$ which has empty channels without extra guest molecules from the reaction. The powder product is ready for lithium intercalation without further framework activation before use. It is worth noting that the

amount of excess water in the reaction is found to be critical to the final product. Without drying the starting materials before the reaction, a green solid was obtained as the final product instead and powder XRD indicated that the sample was not the desired $V^{IV}(O)(bdc)$ phase. Furthermore, it was found that this synthetic method is favorable for scale-up. An attempt to double the amounts of the reactants was successful.

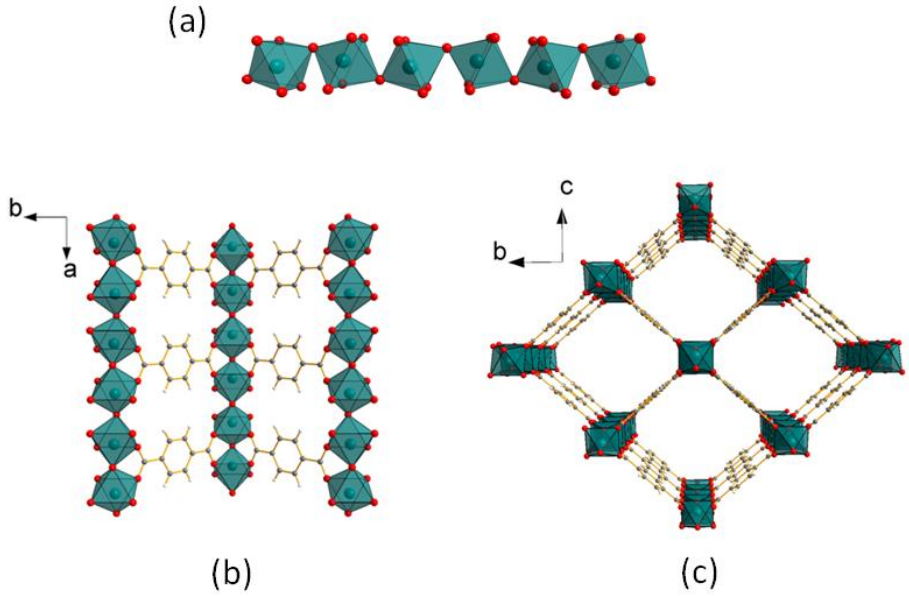

Figure 3.1 Structure of $V^{IV}(O)(bdc)$ framework: (a) Chain of *trans* corner-sharing VO_6 octahedra. (b) VO_6 chains cross-linked by 1,4-benzenedicarboxylate (bdc). (c) Projection of the framework along the *a*-axis showing one-dimensional diamond-shaped channels with an aperture of ~7.6 x 7.7 Å, which can accommodate diffusion of small guest species, such as Li^+ ions. (Illustrated in blue, V^{IV}; red, O; grey, C; white, H.)

3.3.2 Structure and Morphology

The structure and phase purity of V^{IV}(O)(bdc) were confirmed by analyzing the powder XRD data using the profile method. The X-ray diffraction pattern is shown in Figure 3.2. The profile refinement indicated an orthorhombic space group, *Pnma* (wR_p = 2.26%) with lattice parameters a = 6.8221(2) Å, b = 16.069(5) Å, c = 13.982(2) Å, and V = 1534.2(3) $Å^3$, which are very close to those reported previously from single crystal X-ray diffraction data.[51,52] The porous structure of V^{IV}(O)(bdc) can be described as chains of *trans* corner-sharing VO_6 octahedra (Figure 3.1a), which are cross-linked by 1,4-benzenedicarboxylate (bdc) as shown in Figure 3.1b. The octahedral chains have a zigzag −O=V−O=V− backbone with alternating short and long V−O apical bonds of the VO_6 octahedra, with the vanadium ions in the tetravalent oxidation state.[52] The equatorial corners of the VO_6 octahedra are shared with the bdc ligands. The one-dimensional channels (along the *a*-axis) parallel to the octahedral chains have a diamond-shaped cross-section. The size of the empty tunnels available for guest molecules from the space-filling model is approximately 7 x 7 Å (Figure 3.1c). According to the crystal structure of V^{IV}(O)(bdc), the bdc ligands are flat and the benzene ring plane is almost parallel to the channel axis, with an angle of 3.7° between the bdc benzene ring and the *a*-axis.[52] This small inclination of bdc toward the channel axis causes a slight fluctuation of the channel aperture and makes the individual channels polar. Nevertheless, the polarities of neighboring channels are in opposite directions; as a result, the structure as a whole is non-polar.[52] Moreover, since V^{IV}(O)(bdc) has μ_2-oxo as the bridging species between the metal ions, in contrast to MIL-53(Fe) and the other compounds in the MX(bdc) family

which have a bridging μ_2-OH group, this makes V^{IV}(O)(bdc) lack affinity for water. Therefore, the framework with completely empty channels can be obtained and stable under ambient conditions, and guest species may be intercalated.

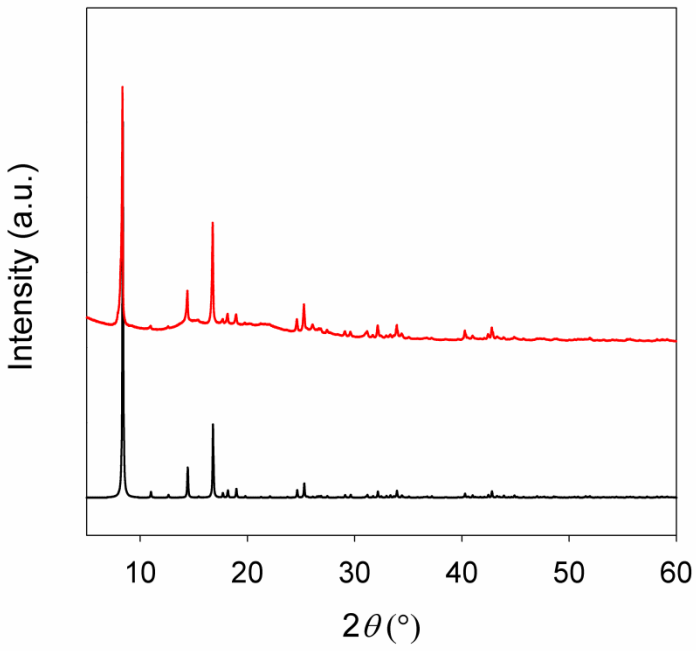

Figure 3.2 Experimental powder X-ray diffraction pattern of V^{IV}(O)(bdc) from the reflux method (illustrated in red) and that simulated from single crystal X-ray diffraction data[52] (shown in black).

3.3.3 Electrochemical Behavior of $V^{IV}(O)(bdc)$

In order to investigate the electrochemical properties, $V^{IV}(O)(bdc)$ was used as an intercalation electrode material.

For room temperature galvanostatic cycling, electrodes composed of V(O)(bdc) were discharged and charged in lithium cells with metallic Li as the negative electrode, at a rate of 1 Li in 12 h or *C*/12 (10 mA/g) with an open circuit voltage (OCV) of ~3.2 V.[50,95–98] The first electrochemical cycle obtained from a coin cell is shown in Figure 3.3. The profile shows that 0.7 Li^+ ions per formula unit can be reversibly inserted into and removed from V(O)(bdc) between 4.0 and 1.8 V, with a pronounced plateau at 2.7 V and a very short one at 1.95 V; the total capacity corresponds to 82 mAh/g. Presumably, over the discharge range from 3.2 V down to 1.8 V (first cycle), the V^{4+} ions in the $V^{IV}(O)(bdc)$ framework actively participate in the electrochemical lithium intercalation, where the metal ions are reduced as Li^+ is inserted into the structure and oxidized during deintercalation. At x in $Li_xV(O)(bdc)$ equal to 0.7, the vanadium ions are believed to be in a mixed valence state, where 70% of the vanadium is reduced to trivalent, while the rest remains tetravalent. The second discharge is quite different from the first, showing significantly less IR drop. Figure 3.3 shows a highly reversible voltage profile of V(O)(bdc) vs Li/Li^+ up to 50 cycles with 50^{th} cycle in red.

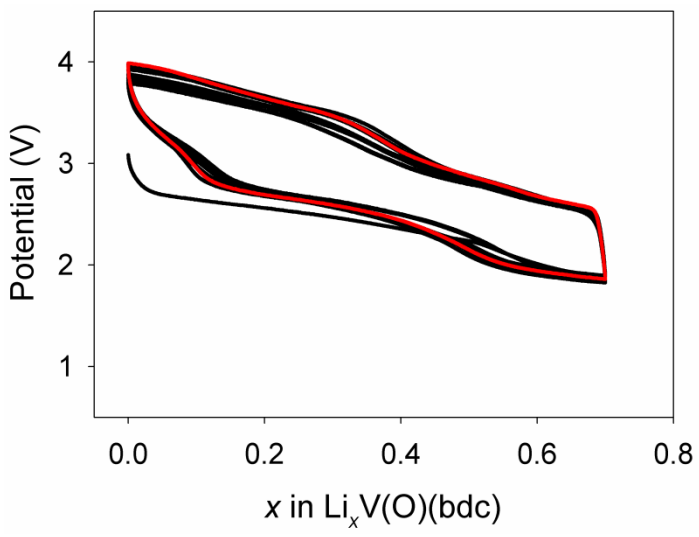

Figure 3.3 Electrochemical profile of a Li/V(O)(bdc) coin cell cycled between 4.0 and 1.8 V up to *x* in $Li_xV(O)(bdc)$ equal to 0.7 at a rate of *C*/12 (10 mA/g); first 50 cycles with 50th cycle highlighted in red.

The discharge voltage profiles of V(O)(bdc) at various *C* rates ranging from *C*/12 (10 mA/g) to 10*C* (1200 mA/g) are shown in Figure 3.4. With increasing discharge rate, the discharge potential decreases due to kinetic effects. With a cutoff voltage of 1.6 V, the cells gave a discharge capacity ranging from 37 up to 118 mAh/g, depending on the cycling rate. It is noteworthy that at a really fast discharge rate of 10*C* (1 Li in 6 min), a discharge capacity as high as ~40 mAh/g can be obtained. The excellent rate capability and high capacity of the electrodes can be attributed to the following: (a) the open three-dimensional porous framework structure of V(O)(bdc) with large empty tunnels. As a result, Li^+ with an effective ionic radius of 0.76 Å can rapidly diffuse into the channels, and the framework can accommodate a large amount of Li^+; and (b) the small particle

size of V(O)(bdc) powder, providing large contact area between the active material and the $LiPF_6$ electrolyte, resulting in short diffusion paths for Li^+ ions, thereby enhancing the rate capability. At discharge rate of *C*/12 (Figure 3.4), 1 Li per formula unit, $x = 1$ in $Li_xV(O)(bdc)$, can be intercalated. This corresponds to the reduction of all of the V^{4+} ions in the structure to V^{3+} with the transformation of the octahedral chain backbone from −O=V−O=V− (indicative of V^{4+}) to −OH −V− OH −V−, as 1 mole of Li^+ ions per formula unit is inserted.

Furthermore, the fact that the host framework used for lithium intercalation in this study is based on vanadium which is an early 3d transition metal with high oxidation states (V^{4+}/V^{3+} redox couple), means lower occupation of 3d electron orbitals: $3d^0\,4s^1$ for V^{4+} and $3d^0\,4s^2$ for V^{3+}. This leads to higher M−O bond stability with respect to charge variations during redox intercalation/deintercalation of Li ions, and could be responsible for the good reversibility of Li insertion/extraction in V(O)(bdc). A similar phenomenon has been observed in the case of oxidative removal of H_2bdc molecules from the channels of MIL-47as, $[V^{III}(OH)(bdc)](H_2bdc)_x$, where the framework V^{3+} ions are oxidized to V^{4+} forming $V^{IV}(O)(bdc)$ or MIL-47, without changing the topology of the framework, providing an evidence of chemically induced redox reactions within this system.[51] A few examples also exist in Fe-based members of this compound series MX(bdc),[57] including the use of MIL-53(Fe), $[Fe^{III}(OH)_{0.8}F_{0.2}(bdc)](H_2O)$, for Li intercalation in lithium batteries, which involves reversible Fe^{3+}/Fe^{2+} redox couple without any alteration of the structure.[50] One aspect of the compounds in MX(bdc) family that is worth mentioning, is their ability to demonstrate significant structural flexibility (dynamic frameworks) upon

loading/unloading of guest species without deformation of the framework. Such behavior has been discussed in great detail,[52,93] and could explain the stability of the host V(O)(bdc) structure during reversible lithium insertion.

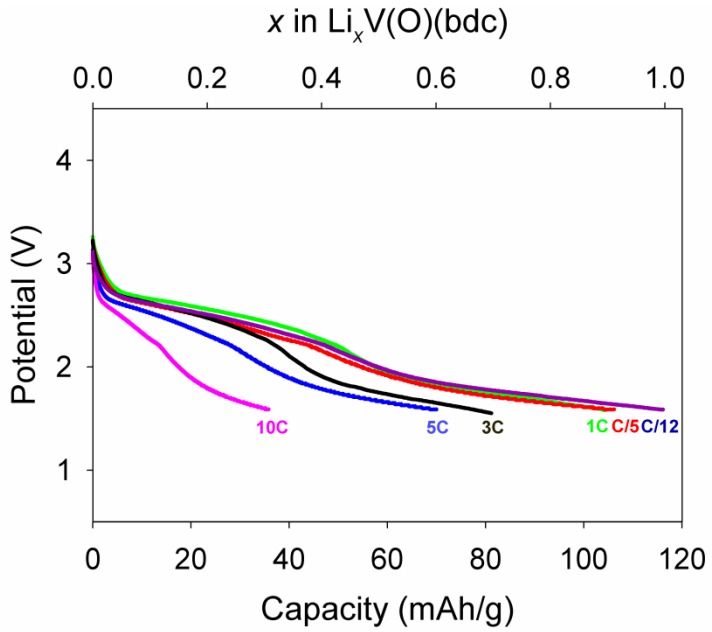

Figure 3.4 Rate performance of Li/V(O)(bdc) coin cells at various discharge rates: 10*C* = 1200 mA/g, 5*C* = 600 mA/g, 3*C* = 360 mA/g, 1*C* = 120 mA/g, *C*/5 = 24 mA/g, and *C*/12 = 10 mA/g.

Results of repeated galvanostatic cycling of Li/V(O)(bdc) cells with a rate of *C*/12 are shown in Figure 3.5. The reversible specific capacity vs cycle number shows excellent capacity retention up to at least 50 cycles with 100% coulombic efficiency, when the cell is cycled to *x* in $Li_xV(O)(bdc)$ equal to 0.7 (Figure 3.5, black circles). It is worth noting that when the cells are cycled further than *x* = 0.7 (down to *x* = 1.0 and *x* =

1.3), the capacity declines during initial cell cycles followed by capacity retention of ~70−75 mAh/g as shown in Figure 3.5, red squares and blue triangles, respectively. The irreversible initial capacity loss may be explained by additional Li-reactions that are non-reversible at low cell discharge voltage, irreversible structural deformation upon large loading of the guest lithium ions causing too much lattice strain, and part of Li^+ ions becoming trapped in the framework.

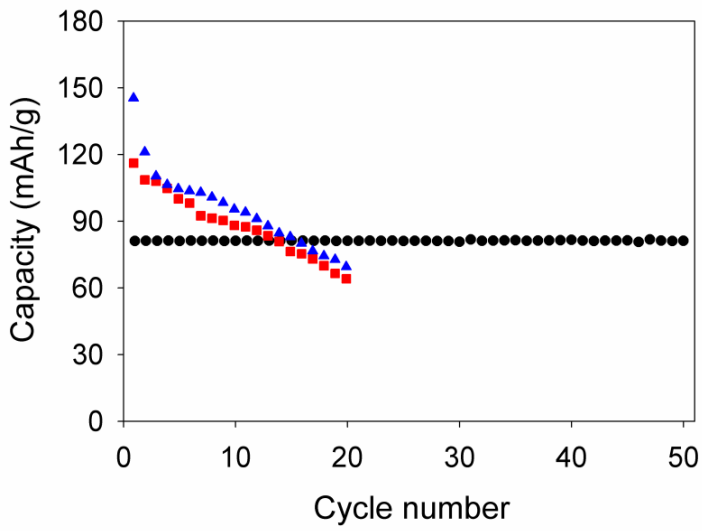

Figure 3.5 Capacity retention data for galvanostatic cycling of Li/V(O)(bdc) cells at *C*/12 (10 mA/g) when cycled to *x* in $Li_xV(O)(bdc)$ = 0.7 (black circles), *x* = 1.0 (red squares), and *x* = 1.3 (blue triangles).

3.3.4 Chemical Redox Study of V(O)(bdc) using a Reducing Agent

To further understand the structural evolution of V(O)(bdc) upon lithium insertion/extraction, X-ray diffraction data were obtained for chemically reduced V(O)(bdc) ($Li_xV(O)(bdc)$, $x = 0.5$ to $x = 2$). As described earlier, *n*-BuLi can be used as a reducing agent to prepare $Li_xV(O)(bdc)$ from V(O)(bdc) in a ratio according to the reaction: $V(O)(bdc) + xC_4H_9Li \rightarrow Li_xV(O)(bdc) + x/2C_8H_{18}$.[99] The *x* value was confirmed by titration of the filtrate which had been hydrolyzed, with a standardized aqueous HCl solution to determine the amount of *n*-BuLi left over from the reaction. Because hexane was used as the reaction medium during the chemical intercalation, the product $Li_xV(O)(bdc)$ was subsequently equilibrated in the electrolyte (1 M $LiPF_6$ solution in EC/DMC) by stirring for 24 h, to ensure the compositional homogeneity of the lithiated particles. X-ray diffraction measurements were performed on $Li_xV(O)(bdc)$ using a sealed sample holder loaded in the glovebox. The resulting X-ray diffraction patterns are shown in Figure 3.6 and the lattice parameters determined by profile refinement using GSAS are summarized in Figure 3.7. Figure 3.8 gives an example of the refinement of the pristine V(O)(bdc) for comparison with $Li_xV(O)(bdc)$ ($x = 2$).

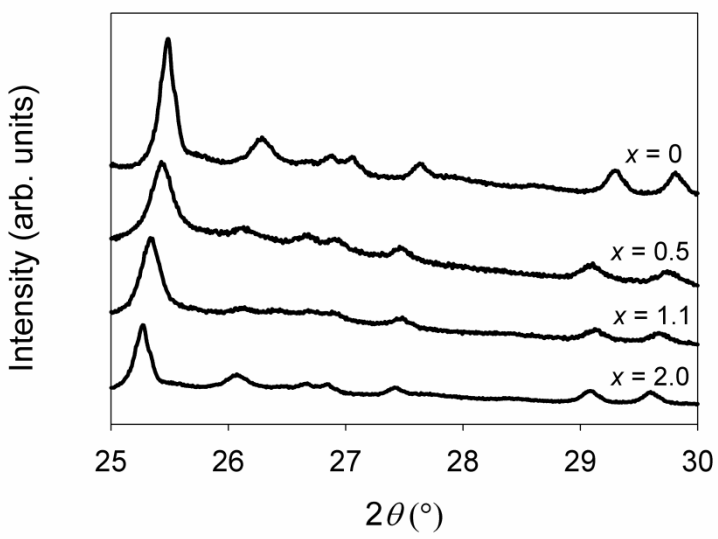

Figure 3.6 X-ray diffraction patterns of $Li_xV(O)(bdc)$, illustrating the changes occurring in the range of $x = 0 \rightarrow 2$; selected 2θ range (25−30°). The samples were prepared by chemical reduction using *n*-BuLi.

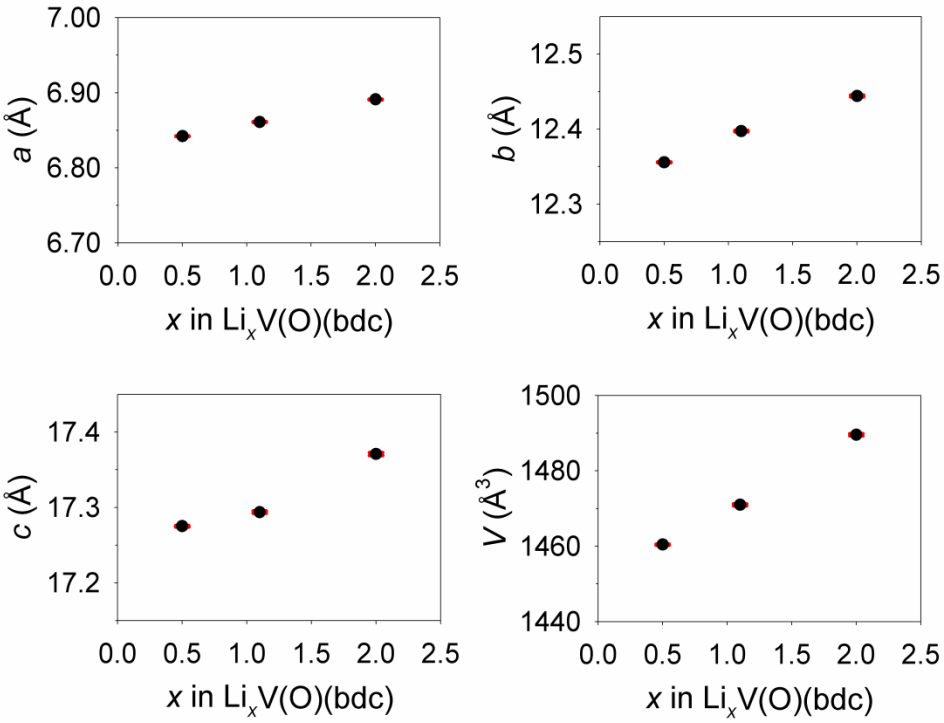

Figure 3.7 Lattice parameters and unit cell volume of chemically prepared $Li_xV(O)(bdc)$ refined by profile fitting (error bars in red).

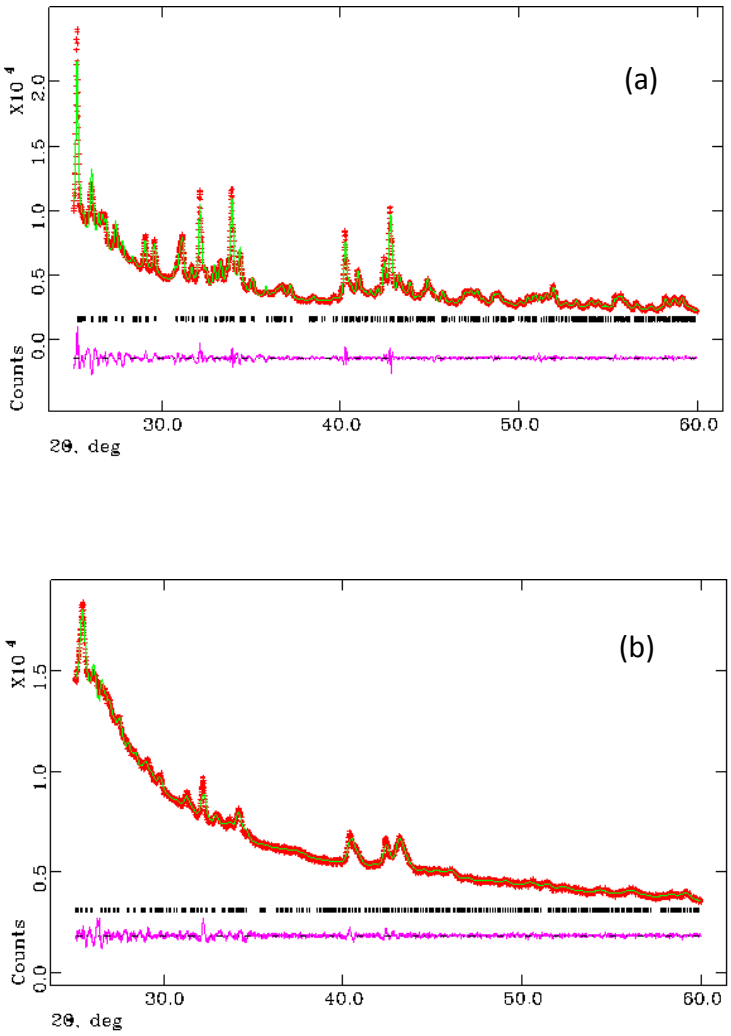

Figure 3.8 (a) Le Bail XRD refinement of pristine V(O)(bdc). (b) The refinement of $Li_2V(O)(bdc)$ prepared from V(O)(bdc) using *n*-BuLi in $P2_12_12_1$, wR_p = 1.98%: lattice parameters a = 6.8909(5) Å, b = 12.444(1) Å, and c = 17.371(2) Å. (The measured data are shown in orange, the calculated data are shown in green, and the difference is shown in pink. Bragg reflections are shown by vertical tick marks.)

The results of the chemically prepared $Li_xV(O)(bdc)$ phases ($0 \leq x \leq 2$) are in good agreement with the voltage profile shown in Figure 3.3. Starting from the pristine V(O)(bdc), the electrochemical insertion of Li^+ ions into crystalline V(O)(bdc) takes place through a two-phase equilibrium, which can be easily identified by the presence of a potential plateau at 2.7 V on the galvanostatic discharge curve. When Li^+ ions are inserted into $Li_xV(O)(bdc)$ (from $x = 0$ to ca. 0.1), a gradual decrease of cell potential is observed, corresponding to a single-phase solid solution. For $x = 0.1 \rightarrow$ ca. 0.4, the phase $Li_xV(O)(bdc)$ ($x = 0{-}0.1$) is in equilibrium with the second solid solution phase that is formed when $0.4 \leq x \leq 0.5$. The profile refinements suggest that $Li_xV(O)(bdc)$ ($0.4 \leq x \leq 0.5$) has a similar structure to the parent compound with the orthorhombic $P2_12_12_1$ structure.

Further intercalation results in a very short voltage plateau compared to the first one at ca. $x = 0.55$, and the process taking place at this point is not understood. At $x > 0.6$, no plateau is observed, consistent with the lithiation occurring in a single phase (as shown in Figure 3.3 and 3.4). Thus, $Li_xV(O)(bdc)$ ($x > 0.6$) can be considered as a solid solution. The lattice parameters of $Li_xV(O)(bdc)$ ($x = 2$) with space group $P2_12_12_1$ show that the unit cell volume of $Li_2V(O)(bdc)$ is only ~2% larger than that of the parent compound due to the guest insertion. Overall, there is a clear trend in the lattice parameters as x in $Li_xV(O)(bdc)$ is larger: the increase of lattice parameters b and c is more pronounced than that of lattice parameters a, which correspond to the direction of corner-sharing VO_6 chains.

During charge, deintercalation of lithium occurs and the phase transition results in solid-solution-like electrochemical behavior, with sloping voltage profile over the range from $x = 0.7 \rightarrow x = 0$ in case of Figure 3.3. The result suggests that some structural reorganization, as indicated by the electrochemical and PXRD data, does occur but nevertheless lithium intercalation into V(O)(bdc) is reversible.

3.4 Conclusions

The polycrystalline microporous vanadium-based compound, V^{IV}(O)(bdc) or MIL-47, prepared by the reflux method behaves as a rechargeable intercalation electrode material in Li-based batteries. V(O)(bdc) can be reversibly cycled in an electrochemical cell with lithium metal as the counter electrode at rates up to 10*C* with good specific capacity. The structural changes associated with the electrochemical lithiation have been characterized through ex-situ X-ray diffraction of phases prepared by a chemical route. Li^+ ions can be chemically intercalated into V(O)(bdc) using *n*-BuLi. At $x = 2$ in $Li_xV(O)(bdc)$, the unit cell volume is only 2% larger than that of the pristine compound. Large open channels along the crystallographic *a*-axis of the framework and the ability to demonstrate structural flexibility upon guest loading/unloading of V(O)(bdc) could account for the lithium storage capacity with small unit cell volume expansion, which reduces lattice strain and helps with intercalation reversibility and the stability of the host structure. The higher M−O bond stability of V(O)(bdc) with respect to charge variations during the redox intercalation, may also play an important role on a high specific capacity. In contrast, the isostructural iron compound MIL-53(Fe), $[Fe^{III}(OH)_{0.8}F_{0.2}(bdc)]$, suffers

from a poor capacity of ~70 mAh/g, corresponding to the limited amount of Li that can be reversibly inserted (< 0.6 Li per Fe), even though available sites still exist in the structure. This is due to the fact that when more than half of the Fe^{3+} ions in the structure are reduced to Fe^{2+}, the local environment of the metal ions is strongly destabilized.[100–102] By further understanding of the mechanism involved during Li insertion and modification of the basic framework architecture, such as organic linker functionalization, the electrochemical properties of this vanadium-based MOF may be improved.

3.5 References

[1] Armand, M.; Tarascon, J.-M. *Nature* **2008**, *451*, 652−657.

[2] Goodenough, J. B.; Kim, Y. *Chem. Mater*. **2010**, *22*, 587−603.

[3] Scrosati, B.; Hassoun, J.; Sun, Y.-K. *Energy Environ. Sci*. **2011**, *4*, 3287−3295.

[4] Morozan, A.; Jaouen, F. *Energy Environ. Sci.* **2012**, *5*, 9269−9290.

[5] Padhi, A. K.; Nanjundaswamy, K. S.; Goodenough, J. B. *J. Electrochem. Soc.* **1997**, *144*, 1188−1194.

[6] Masquelier, C.; Wurm, C.; Rodríguez-Carvajal, J.; Gaubicher, J.; Nazar, L. *Chem. Mater*. **2000**, *12*, 525−532.

[7] Kuganathan, N.; Islam, M. S. *Chem. Mater*. **2009**, *21*, 5196−5202.

[8] Nishimura, S.-I.; Hayase, S.; Kanno, R.; Yashima, M.; Nakayama, N.; Yamada, A. *J. Am. Chem. Soc*. **2008**, *130*, 13212−13213.

[9] Aricò, A. S.; Bruce, P.; Scrosati, B.; Tarascon, J.-M.; van Schalkwijk, W. *Nat. Mater*. **2005**, *4*, 366−377.

[10] Barpanda, P.; Ati, M.; Melot, B. C.; Rousse, G.; Chotard, J. N.; Doublet, M. L.; Sougrati, M. T.; Corr, S. A.; Jumas, J. C.; Tarascon, J.-M. *Nat. Mater*. **2011**, *10*, 772−779.

[11] Yamada, A.; Iwane, N.; Harada, Y.; Nishimura, S.-I.; Koyama, Y.; Tanaka, I. *Adv. Mater*. **2010**, *22*, 3583−3587.

[12] Afyon, S.; Wörle, M.; Nesper, R. *Angew. Chem., Int. Ed.* **2013**, *52*, 12541−12544.

[13] Kerr, T. A.; Gaubicher, J.; Nazar, L. F. *Electrochem. Solid-State Lett*. **2000**, *3*, 460−462.

[14] Saravanan, K.; Lee, H. S.; Kuezma, M.; Vittal, J. J.; Balaya, P. *J. Mater. Chem.* **2011**, *21*, 10042−10050.

[15] Barker, J.; Saidi, M. Y.; Swoyer, J. L. *J. Electrochem. Soc.* **2004**, *151*, A1670−A1677.

[16] Reddy, M. V.; Subba Rao, G. V.; Chowdari, B. V. R. *J. Power Sources* **2010**, *195*, 5768−5774.

[17] Nishimura, S.-I.; Nakamura, M.; Natsui, R.; Yamada, A. *J. Am. Chem. Soc*. **2010**, *132*, 13596−13597.

[18] Whittingham, M. S. *Chem. Rev*. **2004**, *104*, 4271−4301.

[19] Kaveevivitchai, W.; Jacobson, A. J. *Chem. Mater*. **2013**, *25*, 2708−2715.

[20] Masquelier, C.; Croguennec, L. *Chem. Rev*. **2013**, *113*, 6552−6591.

[21] Armand, M.; Grugeon, S.; Vezin, H.; Laruelle, S.; Ribiere, P.; Poizot, P.; Tarascon, J.-M. *Nat. Mater*. **2009**, *8*, 120−125.

[22] Xiang, J.; Chang, C.; Li, M.; Wu, S.; Yuan, L.; Sun, J. *Cryst. Growth Des*. **2008**, *8*, 280−282.

[23] Zeng, R.-H.; Li, X.-P.; Qiu, Y.-C.; Li, W.-S.; Yi, J.; Lu, D.-S.; Tan, C.-L.; Xu, M.-Q. *Electrochem. Commun.* **2010**, *12*, 1253−1256.

[24] Chen, H.; Armand, M.; Courty, M.; Jiang, M.; Grey, C. P.; Dolhem, F.; Tarascon, J.-M.; Poizot, P. *J. Am. Chem. Soc*. **2009**, *131*, 8984−8988.

[25] Zhao, R. R.; Cao, Y. L.; Ai, X. P.; Yang, H. X. *J. Electroanal. Chem*. **2013**, *688*, 93−97.

[26] Song, Z.; Zhou, H. *Energy Environ. Sci.* **2013**, *6*, 2280–2301.

[27] Poizot, P.; Dolhem, F. *Energy Environ. Sci.* **2011**, *4*, 2003–2019.

[28] Morita, Y.; Nishida, S.; Murata, T.; Moriguchi, M.; Ueda, A.; Satoh, M.; Arifuku, K.; Sato, K.; Takui, T. *Nat. Mater*. **2011**, *10*, 947−951.

[29] Li, S.-L.; Xu, Q. *Energy Environ. Sci*. **2013**, *6*, 1656−1683.

[30] Allendorf, M. D.; Schwartzberg, A.; Stavila, V.; Talin, A. A. *Chem. Eur. J*. **2011**, *17*, 11372−11388.

[31] Férey, G. *Chem. Soc. Rev*. **2008**, *37*, 191−214.

[32] Sumida, K.; Rogow, D. L.; Mason, J. A.; McDonald, T. M.; Bloch, E. D.; Herm, Z. R.; Bae, T.-H.; Long, J. R. *Chem. Rev*. **2012**, *112*, 724−781.

[33] Kitagawa, S.; Kitaura, R.; Noro, S. I. *Angew. Chem., Int. Ed*. **2004**, *43*, 2334−2375.

[34] Li, J.-R.; Kuppler, R. J.; Zhou, H.-C. *Chem. Soc. Rev*. **2009**, *38*, 1477−1504.

[35] Czaja, A. U.; Trukhan, N.; Müller, U. *Chem. Soc. Rev*. **2009**, *38*, 1284−1293.

[36] Lee, J.; Farha, O. K.; Roberts, J.; Scheidt, K. A.; Nguyen, S. T.; Hupp, J. T. *Chem. Soc. Rev*. **2009**, *38*, 1450−1459.

[37] Bétard, A.; Fisher, R. A. *Chem. Rev*. **2012**, *112*, 1055−1083.

[38] Dhakshinamoorthy, A.; Alvaro, M.; Garcia, H. *Chem. Commun*. **2012**, *48*, 11275−11288.

[39] Khajavi, H.; Gascon, J.; Schins, J. M.; Siebbeles, L. D. A.; Kapteijn, F. *J. Phys. Chem. C* **2011**, *115*, 12487−12493.

[40] Wessells, C. D.; Huggins, R. A.; Cui, Y. *Nat. Commun*. **2011**, *2*, 550−554.

[41] Givaja, G.; Amo-Ochoa, P.; Gómez-García, C. J.; Zamora, F. *Chem. Soc. Rev.* **2012**, *41*, 115−147.

[42] Hendon, C. H.; Tiana, D.; Walsh, A. *Phys. Chem. Chem. Phys*. **2012**, *14*, 13120−13132.

[43] Silva, C. G.; Corma, A.; García, H. *J. Mater. Chem*. **2010**, *20*, 3141−3156.

[44] Yoon, S. M.; Warren, S. C.; Grzybowski, B. A. *Angew. Chem., Int. Ed.* **2014**, *53*, 4437−4441.

[45] Yanai, N.; Uemura, T.; Ohba, M.; Kadowaki, Y.; Maesato, M.; Takenaka, M.; Nishitsuji, S.; Hasegawa, H.; Kitagawa, S. *Angew. Chem., Int. Ed.* **2008**, *47*, 9883−9886.

[46] Meilikhov, M.; Yusenko, K.; Fischer, R. A. *J. Am. Chem. Soc*. **2009**, *131*, 9644−9645.

[47] Tran-Van, P.; Barthelet, K.; Morcrette, M.; Harlem, M.; Tarascon, J.-M.; Cheetham, A. K.; Férey, G. *J. New Mater. Electrochem. Syst.* **2003**, *6*, 29−34.

[48] Cheng, C.-Y.; Fu, S.-J.; Yang, C.-J.; Chen, W.-H.; Lin, K.-J.; Lee, G.-H.; Wang, Y. *Angew. Chem., Int. Ed.* **2003**, *42*, 1937−1940.

[49] Li, X.; Cheng, F.; Zhang, S.; Chen, J. *J. Power Sources* **2006**, *160*, 542−547.

[50] Férey, G.; Millange, F.; Morcrette, M.; Serre, C.; Doublet, M.-L.; Grenèche, J.-M.; Tarascon, J.-M. *Angew. Chem., Int. Ed.* **2007**, *46*, 3259−3263.

[51] Barthelet, K.; Marrot, J.; Riou, D.; Férey, G. *Angew. Chem., Int. Ed.* **2002**, *41*, 281−284.

[52] Wang, X.; Liu, L.; Jacobson, A. J. *Angew. Chem., Int. Ed.* **2006**, *45*, 6499−6503.

[53] Serre, C.; Millange, F.; Thouvenot, C.; Noguès, M.; Marsolier, G.; Louër, D.; Férey, G. *J. Am. Chem. Soc*. **2002**, *124*, 13519−13526.

[54] Loiseau, T.; Serre, C.; Huguenard, C.; Fink, G.; Taulelle, F.; Henry, M.; Bataille, T.; Férey, G. *Chem. Eur. J*. **2004**, *10*, 1373−1382.

[55] Liu, L.; Wang, X.; Jacobson, A. J. *Dalton Trans*. **2010**, *39*, 1722−1725.

[56] Whitfield, T. R.; Wang, X.; Jacobson, A. J. *Mater. Res. Soc. Symp. Proc*. **2002**, *755*, 191−196.

[57] Whitfield, T. R.; Wang, X.; Liu, L.; Jacobson, A. J. *Solid State Sci.* **2005**, *7*, 1096−1103.

[58] Millange, F.; Guillou, N.; Walton, R. I.; Grenèche, J.-M.; Margiolaki, I.; Férey, G. *Chem. Commun*. **2008**, 4732−4734.

[59] Anokhina, E. V.; Vougo-Zanda, M.; Wang, X.; Jacobson, A. J. *J. Am. Chem. Soc*. **2005**, *127*, 15000−15001.

[60] Vougo-Zanda, M; Huang, J.; Anokhina, E.; Wang, X.; Jacobson, A. J. *Inorg. Chem*. **2008**, *47*, 11535−11542.

[61] Xu, G.; Zhang, X.; Guo, P.; Pan, C.; Zhang, H.; Wang, C. *J. Am. Chem. Soc*. **2010**, *132*, 3656−3657.

[62] Mowat, J. P. S.; Miller, S. R.; Slawin, A. M. Z.; Seymour, V. R.; Ashbrook, S. E.; Wright, P. A. *Microporous Mesoporous Mater.* **2011**, *142*, 322−333.

[63] Mowat, J. P. S.; Seymour, V. R.; Griffin, J. M.; Thompson, S. P.; Slawin, A. M. Z.; Fairen-Jimenez, D.; Düren, T.; Ashbrook, S. E.; Wright, P. A. *Dalton Trans*. **2012**, *41*, 3937−3941.

[64] De Combarieu, G.; Morcrette, M.; Millange, F.; Guillou, N.; Cabana, J.; Grey, C. P.; Margiolaki, I.; Férey, G.; Tarascon, J.-M. *Chem. Mater*. **2009**, *21*, 1602−1611.

[65] Fateeva, A.; Horcajada, P.; Devic, T.; Serre, C.; Marrot, J.; Grenèche, J.-M.; Morcrette, M.; Tarascon, J.-M.; Maurin, G.; Férey, G. *Eur. J. Inorg. Chem.* **2010**, 3789−3794.

[66] Saravanan, K.; Nagarathinam, M.; Balaya, P.; Vittal, J. J. *J. Mater. Chem.* **2010**, *20*, 8329−8335.

[67] Nguyen, T. L. A.; Demir-Cakan, R.; Devic, T.; Morcrette, M.; Ahnfeldt, T.; Auban-Senzier, P.; Stock, N.; Goncalves, A.-M.; Filinchuk, Y.; Tarascon, J.-M.; Férey, G. *Inorg. Chem.* **2010**, *49*, 7135−7143.

[68] Nguyen, T. L. A.; Devic, T.; Mialane, P.; Rivière, E.; Sonnauer, A.; Stock, N.; Demir-Cakan, R.; Morcrette, M.; Livage, C.; Marrot, J.; Tarascon, J.-M.; Férey, G. *Inorg. Chem.* **2010**, *49*, 10710−10717.

[69] Okubo, M.; Asakura, D.; Mizuno, Y.; Kim, J. D.; Mizokawa, T.; Kudo, T.; Honma, I. J. *Phys. Chem. Lett*. **2010**, *1*, 2063−2071.

[70] Asakura, D.; Okubo, M.; Mizuno, Y.; Kudo, T.; Zhou, H.; Amemiya, K.; De Groot, F. M. F.; Chen, J.-L.; Wang, W.-C.; Glans, P.-A.; Chang, C.; Guo, J.; Honma, I. *Phys. Rev. B* **2011**, *84*, 045117/1−045117/6.

[71] Mizuno, Y.; Okubo, M.; Asakura, D.; Saito, T.; Hosono, E.; Saito, Y.; Oh-ishi, K.; Kudo, T.; Zhou, H. *Electrochim. Acta* **2012**, *63*, 139−145.

[72] Asakura, D.; Okubo, M.; Mizuno, Y.; Kudo, T.; Zhou, H.; Ikedo, K.; Mizokawa, T.; Okazawa, A.; Kojima, N. *J. Phys. Chem. C* **2012**, *116*, 8364−8369.

[73] Okubo, M.; Asakura, D.; Mizuno, Y.; Kudo, T.; Zhou, H.; Okazawa, A.; Kojima, N.; Ikedo, K.; Mizokawa, T.; Honma, I. *Angew. Chem., Int. Ed.* **2011**, *50*, 6269−6273.

[74] Asakura, D.; Li, C. H.; Mizuno, Y.; Okubo, M.; Zhou, H.; Talham, D. R. *J. Am. Chem. Soc*. **2013**, *135*, 2793−2799.

[75] Nanba, Y.; Asakura, D.; Okubo, M.; Mizuno, Y.; Kudo, T.; Zhou, H.; Amemiya, K.; Guo, J.; Okada, K. *J. Phys. Chem. C* **2012**, *116*, 24896−24901.

[76] Wessells, C. D.; Peddada, S. V.; Huggins, R. A.; Cui, Y. *Nano Lett.* **2011**, *11*, 5421−5425.

[77] Wessells, C. D.; McDowell, M. T.; Peddada, S. V.; Pasta, M.; Huggins, R. A.; Cui, Y. *ACS Nano* **2012**, *6*, 1688−1694.

[78] Pasta, M.; Wessells, C. D.; Huggins, R. A.; Cui, Y. *Nat. Commun*. **2012**, *3*, 1149.

[79] Lu, Y.; Wang, L.; Cheng, J.; Goodenough, J. B. *Chem. Commun*. **2012**, *48*, 6544−6546.

[80] Nagarathinam, M.; Saravanan, K.; Phua, E. J. H.; Reddy, M. V.; Chowdari, B. V. R.; Vittal, J. J. *Angew. Chem., Int. Ed.* **2012**, *51*, 5866−5870.

[81] Liu, Q.; Yu, L.; Wang, Y.; Ji, Y.; Horvat, J.; Cheng, M.-L.; Jia, X.; Wang, G. *Inorg. Chem.* **2013**, *52*, 2817−2822.

[82] Okubo, M.; Kagesawa, K.; Mizuno, Y.; Asakura, D.; Hosona, E.; Kudo, T.; Zhou, H.; Fujii, K.; Uekusa, H.; Nishimura, S.-I.; Yamada, A.; Okazawa, A.; Kojima, N. *Inorg. Chem.* **2013**, *52*, 3772−3779.

[83] Gou, L.; Hao, L.-M.; Shi, Y.-X.; Ma, S.-L.; Fan, X.-Y.; Xu, L.; Li, D.-L.; Wang, K. *J. Solid State Chem.* **2014**, *210*, 121−124.

[84] Zhang, L.; Wu, H. B.; Madhavi, S.; Hng, H. H.; Lou, X. W. *J. Am. Chem. Soc*. **2012**, *134*, 17388−17391.

[85] Zhang, L.; Wu, H. B.; Lou, X. W. *J. Am. Chem. Soc*. **2013**, *135*, 10664−10672.

[86] Cao, X.; Zheng, B.; Rui, X.; Shi, W.; Yan, Q.; Zhang, H. *Angew. Chem., Int. Ed.* **2014**, *53*, 1404−1409.

[87] Yang, S. J.; Nam, S.; Kim, T.; Im, J. H.; Jung, H.; Kang, J. H.; Wi. S.; Park, B.; Park, C. R. *J. Am. Chem. Soc*. **2013**, *135*, 7394−7397.

[88] Li, Q.; Xu, P.; Gao, W.; Ma, S.; Zhang, G.; Cao, R.; Cho, J.; Wang, H.-L.; Wu, G. *Adv. Mater*. **2014**, *26*, 1378−1386.

[89] Wu, D.; Guo, Z.; Yin, X.; Pang, Q.; Tu, B.; Zhang, L.; Wang, Y.-G.; Li, Q. *Adv. Mater*. **2014**, *26*, 3258−3262.

[90] Demir-Cakan, R.; Morcrette, M.; Nouar, F.; Davoisne, C.; Devic, T.; Gonbeau, D.; Dominko, R.; Serre, C.; Férey, G.; Tarascon, J.-M. *J. Am. Chem. Soc*. **2011**, *133*, 16154−16160.

[91] Wang, Z.; Li, X.; Cui, Y.; Yang, Y.; Pan, H.; Wang, Z.; Wu, C.; Chen, B.; Qian, G. *Cryst. Growth Des*. **2013**, *13*, 5116−5120.

[92] Zheng, J.; Tian, J.; Wu, D.; Gu, M.; Xu, W.; Wang, C.; Gao, F.; Engelhard, M. H.; Zhang, J.-G.; Liu, J.; Xiao, J. *Nano Lett*. **2014**, *14*, 2345−2352.

[93] Wang, X.; Eckert, J.; Liu, L.; Jacobson, A. J. *Inorg. Chem*. **2011**, *50*, 2028−2036.

[94] Jacobson, A. J.; Wang, X.; Liu, L. U.S. Patent 2010/0176031, 2010.

[95] Mikhailova, D.; Sarapulova, A.; Voss, A.; Thomas, A.; Oswald, S.; Gruner, W.; Trots, D. M.; Bramnik, N. N.; Ehrenberg, H. *Chem. Mater*. **2010**, *22*, 3165−3173.

[96] Sathiya, M.; Ramesha, K.; Rousse, G.; Foix, D.; Gonbeau, D.; Prakash, A. S.; Doublet, M. L.; Hemalatha, K.; Tarascon, J.-M. *Chem. Mater*. **2013**, *25*, 1121−1131.

[97] Ellis, B. L.; Michael Makahnouk, W. R.; Rowan-Weetaluktuk, W. N.; Ryan, D. H.; Nazar, L. F. *Chem. Mater*. **2010**, *22*, 1059−1070.

[98] Saravanan, K.; Ananthanarayanan, K.; Balaya, P. *Energy Environ. Sci*. **2010**, *3*, 939−948.

[99] Dickens, P. G.; French, S. J.; Hight, A. T.; Pye, M. F. *Mater. Res. Bull*. **1979**, *14*, 1295−1299.

[100] Combelles, C.; Yahia, M. B.; Pedesseau, L.; Doublet, M.-L. *J. Power Sources* **2011**, *196*, 3426−3432.

[101] Combelles, C.; Doublet, M.-L. *Ionics* **2008**, *14*, 279−283.

[102] Combelles, C.; Yahia, M. B.; Pedesseau, L.; Doublet, M.-L. *J. Phys. Chem. C* **2010**, *114*, 9518−9527.

Chapter 4

Electrochemical Reactions of Lithium with Transition Metal Formates

4.1 Introduction

For the past two decades, a significantly increasing demand for portable electronic devices and electric vehicles worldwide has driven the developments of advanced energy storage systems, such as rechargeable lithium-based batteries.[1–7] Despite several advantages of today's Li-ion batteries (LIBs), batteries with superior performance, higher power and energy density, and longer lifespan are still required to power newly emerging electronics, and new electrode materials are still needed. [8–14] Among rapidly growing classes of materials, metal-organic frameworks (MOFs), assembled from inorganic building units and organic linkers, have drawn considerable attention from research communities due to their fascinating structures and promising applications.[15–20] Despite the variety of useful MOF characteristics, namely, numerous pores, cavities, and active sites which may accommodate Li^+ ions, up to now only a small number of MOFs have been successfully used as electrode materials for lithium batteries (a summary can be found in Table 3.1). Changes in the redox state of the metal centers of MOFs usually lead to a non-reversible degradation of the structure. This is the case for a microporous nickel phosphate MOF and a Zn-based compound (MIL-177) used as electrode materials in Li cells, where the electrochemical reactions led to the irreversible decomposition of the compounds through conversion processes.[21,22] Although a Ga-V phosphonate framework containing redox active oxovanadyl centers underwent insertion of Li ions, the

deintercalation process was found to be difficult, and voltage as high as 5 V vs Li/Li^+ was needed to extract the intercalated ions.[23]

MOFs, such as MIL-53 with composition $[Fe^{III}(OH)_{0.8}F_{0.2}(bdc)](H_2O)$, MIL-68 formulated $[Fe^{III}(OH)(bdc)](dmf)_{1.1}$, Prussian blue analogs (PBAs) $A_xMn^{II}_y[Fe^{III}(CN)_6]\cdot nH_2O$ (A = K, Rb), and TTF-based compounds, $M_2(TTF\text{-}TC)H_2$ (M = K, Rb, Cs) were able to undergo reversible Li^+ insertion/extraction without any alteration of the host structure. However, they suffered from a poor electrochemical capacity.[24–28]

Among the limited number of MOFs used for lithium storage, a formate-based MOF, $Zn_3(HCOO)_6$, has been reported.[29] An incredibly high capacity of 560 mAh/g corresponding to 9.6 moles of Li per formula unit was obtained at a relatively high current density of $0.11C$ within the voltage range of 0.005−3.0 V for up to 60 cycles. The electrochemistry of $Co_3(HCOO)_6$, and $Zn_{1.5}Co_{1.5}(HCOO)_6$ with Li was also studied. The metal formate frameworks were found to react reversibly with Li through conversion reactions rather than intercalation. The matrix involved during discharge-charge cycling was lithium formate, unlike the typical conversion process where Li_2O was formed. Due to the outstanding capacity of the formate-based compounds, $[NH_2(CH_3)_2][Fe^{III}Fe^{II}(HCOO)_6]$ was chosen for an electrochemical investigation.[30] Moreover, iron compounds are the choice for application in lithium battery system because of the low toxicity, redox activity, and low cost due to the abundance of iron.

4.2 Experimental Section

4.2.1 Materials and Measurements

All chemicals used during this work were reagent grade and used as received from commercial sources without further purification. Thermogravimetric analysis (TGA) measurements were carried out using a TA Instruments Hi-Res 2950 system with a heating rate of 5 °C/min. Infrared (IR) measurements were carried out on a PerkinElmer Spectrum 100 FT-IR spectrometer in the range 400− 4000 cm^{-1}. Single crystal X-ray analyses were performed at room temperature on a Siemens SMART platform diffractometer outfitted with an APEX II area detector and monochromatized Mo Kα radiation (λ = 0.71073 Å). Powder X-ray diffraction (PXRD) patterns were collected at room temperature on a Phillips PANalytical X'Pert PRO diffractometer with Cu Kα radiation (λ = 1.54046 Å).

4.2.2 Synthesis

$[NH_2(CH_3)_2][Fe^{III}Fe^{II}(HCOO)_6]$, **FeFOR**, was prepared solvothermally according to the literature procedure,[30] from the mixture of $FeCl_3 \cdot 6H_2O$ (1.5 mmol, 0.41 g) in 15 mL of dimethylformamide (dmf) and formic acid (1:1 V/V). The reactants were heated in a 23 mL Teflon-lined stainless steel Parr autoclave at 145 °C for 2 d, and let cool to room temperature. The reaction conditions were optimized to obtain the pure phase of the compound. Large black crystals of **FeFOR** were vacuum filtered, washed with dmf, and dried in air. (Yield = 50% based on $FeCl_3 \cdot 6H_2O$)

4.2.3 Electrochemical Studies

The electrochemical properties of compound **FeFOR** were investigated in a lithium cell which had lithium metal as counter electrode. Owing to the high reactivity of lithium with moisture, electrochemical cells were assembled in a dry box (argon-filled glovebox used in this case).

Teflon-bag Cells. The active material, **FeFOR**, was mixed and ground with carbon black (a conducting additive) in the weight ratio of 70:30. The mixture was then used as cathode material. Cathodes were prepared by hot pressing the mixture at 100 °C into a stainless steel grid, which served as current collector to give 1 cm^2 of active area. The active material content in the electrode was about 3–7 mg. The electrodes were dried in vacuum at 90 °C for 12 h before transfer to the glovebox, in which cell assembly was performed. Cells were constructed by surrounding the cathodes with microporous polypropylene separators (2400 Celgard membranes), and then lithium foils which served as anodes. The assembled cells were immersed in the electrolyte contained in a Teflon bag. The electrolyte consisted of a solution of 1 M $LiPF_6$ in ethylene carbonate (EC)/dimethyl carbonate (DMC) (1:1 by weight). The cells were pressed together by two glass slides to ensure good contact within the cells, and aged for 12 h before measurements. Electrochemical studies were performed with a multichannel potentiostat-galvanostat MacPile system (Biologic SA, Claix, France) in a potentiostatic mode. Electrochemical testing conditions are specified in the Results and Discussion section.

4.3 Results and Discussion

4.3.1 Structure of FeFOR and Phase Characterization

$[NH_2(CH_3)_2][Fe^{III}Fe^{II}(HCOO)_6]$ (**FeFOR**) is a three-dimensional framework consisting of a formate anion ($HCOO^-$) that connects two metal ions, Fe^{II} and Fe^{III}, as shown in Figure 4.1a.[30] Crystallographic studies show that the compound contains dimethylammonium ions (DMA^+), $(CH_3)_2NH_2^+$, that are disordered in the cavities of the structure, and are formed by decomposition of the solvent dmf. All the metal ions have octahedral geometry, coordinated by six oxygen atoms from six formate anions (Figure 4.1a).[30] Figure 4.1b shows a projection along the *a*-axis of the 3D framework without the cations in the cavities, and Figure 4.1c illustrates the structure with the $(CH_3)_2NH_2^+$ ions shown as space-filling.

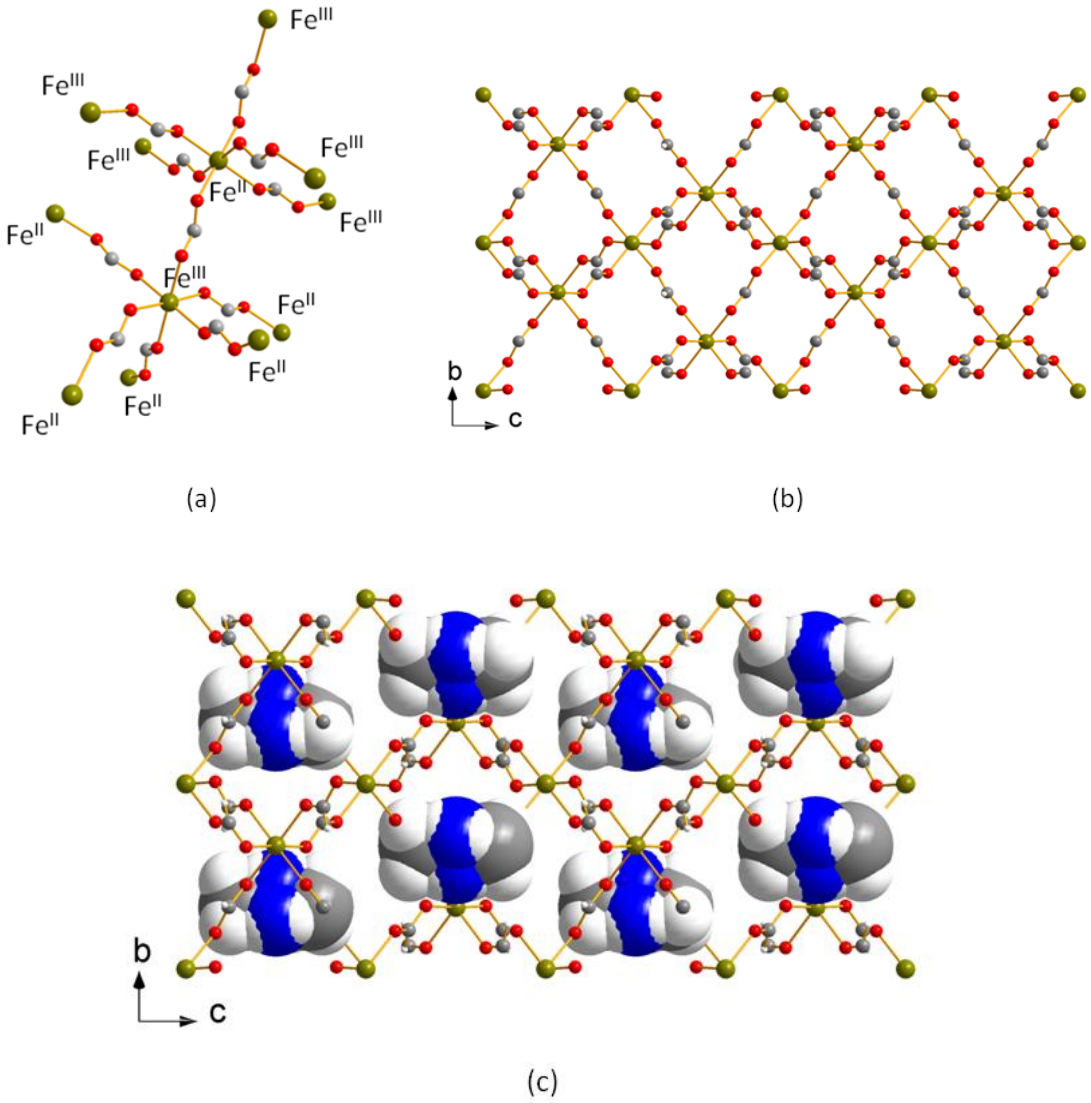

Figure 4.1 (a) Coordination and linkage modes of the ligands and metal ions in **FeFOR**. (b) 3D view of the **FeFOR** framework along the crystallographic *a*-axis. (The $(CH_3)_2NH_2^+$ ions occupying the cavities are omitted.) (c) The structure with the cations shown as space-filling. (Illustrated in green, Fe; red, O; grey, C; white, H; blue, N.)

The two metal atoms in the asymmetric unit are distinguished by the bond distances. The Fe^{II}–O bond length is 2.125(1) Å, whereas the Fe^{III}–O bond is 2.009(1) Å. Each Fe^{II} is coordinated to six Fe^{III} ions by six formate anions, and each Fe^{III} is connected to six Fe^{II} ions (Figure 4.1a). In the synthesis of **FeFOR**, the Fe^{III} from the starting material is reduced to Fe^{II}, as dmf is hydrolyzed into HCOOH and $(CH_3)_2NH$ which is the reducing agent.[30]

The compound was characterized by single crystal X-ray diffraction. The compound (**FeFOR**) crystallized in trigonal $P\bar{3}1/c$ space group with lattice parameters: a = 8.270(1) Å, b = 8.270(1) Å, c = 13.930(3) Å, V = 825.1(2) $Å^3$, with Z = 2.[30] The purity of the bulk phase was confirmed by using powder X-ray diffraction (PXRD). The experimental PXRD pattern is in good agreement with the simulated one from the single crystal structure,[30] confirming the phase purity of bulk samples (Figure 4.2).

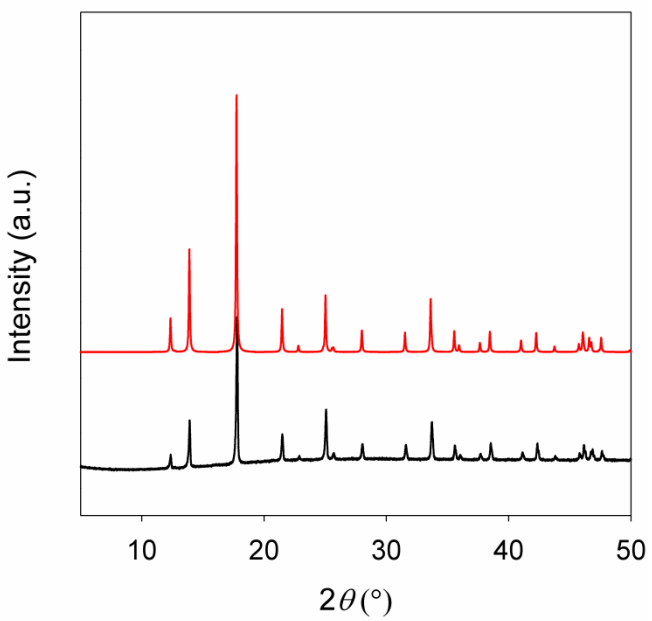

Figure 4.2 Experimental powder X-ray diffraction pattern of **FeFOR** from the optimized synthesis (illustrated in black) and that simulated from the single crystal X-ray diffraction data (shown in red).

Thermogravimetric measurements (TGA) were conducted to investigate the thermal stability of the synthesized compound in air at a heating rate of 5 °C/min. The TGA data of **FeFOR** obtained under flowing air atmosphere show a single-step weight loss (Figure 4.3) at approximately 290 °C. This corresponds to a thermal decomposition to a metal oxide. The experimental residue was examined by powder X-ray diffraction and identified as Fe_2O_3. It can be concluded that **FeFOR** loses its structural integrity upon removal of the guest molecules by heating.

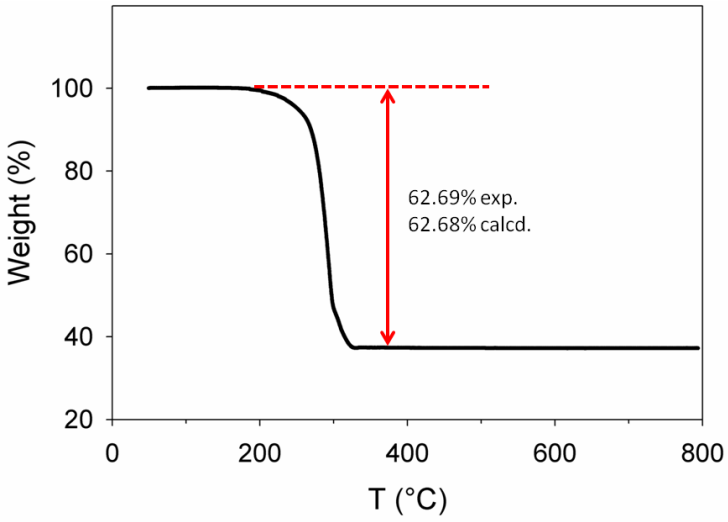

Figure 4.3 Thermogravimetric data of **FeFOR** under an air flow with a heating rate of 5 °C/min.

4.3.2 Electrochemical Behavior of FeFOR

The electrochemical behavior of **FeFOR** was investigated using the potentiostatic mode. Cells containing compound **FeFOR** as cathode material were cycled using 10-mV potential steps with a 0.01 mA preset current limit. **FeFOR** showed highly reversible behavior in the low x region ($0 < x \leq 0.5$), corresponding to 31.3 mAh/g for up to 20 cycles with an open circuit voltage (OCV) of ~3.1 V. Presumably over the discharge range of $0 < x \leq 0.5$, all of the Fe^{3+} ions in **FeFOR** framework are reduced to Fe^{2+} as Li^{+} ions are inserted into the structure and oxidized during deintercalation. A sloping cell voltage is observed which suggests a solid solution (single-phase) behavior. The potential-composition profiles obtained during the first and second discharge-charge are shown in Figure 4.4.

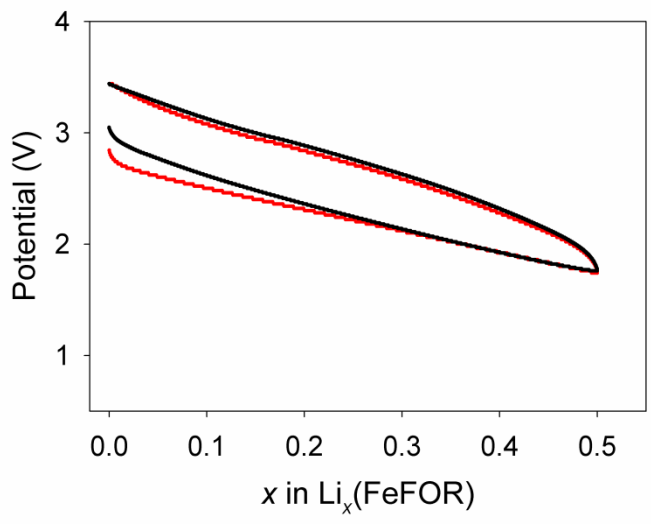

Figure 4.4 Voltage-composition profiles of a Li/**FeFOR** cell discharged and charged between $0 < x \leq 0.5$ (1^{st} cycle in red and 2^{nd} cycle in black).

On discharge $x \geq 0.5$, it was found that the cell was still reversible. A voltage-composition plot when the cell was discharged to x equal to 2 is displayed (Figure 4.5).

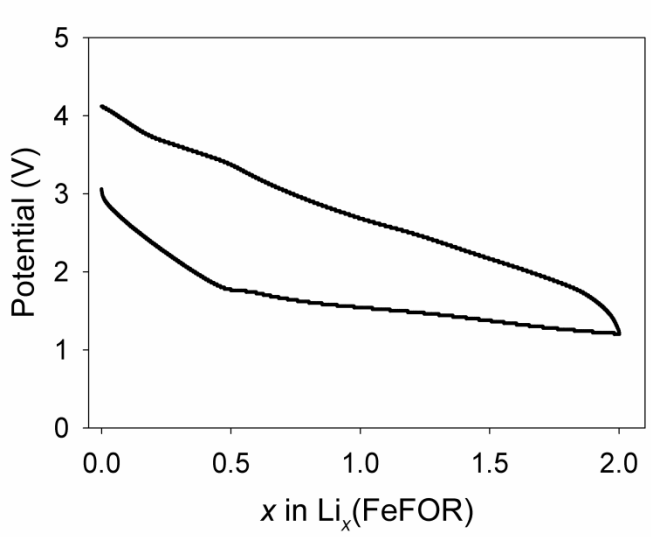

Figure 4.5 Voltage-composition profile of a Li/**FeFOR** cell discharged and charged between $0 < x \leq 2$.

Figure 4.5 shows a distinct slope change on the discharge curve at x equal to 0.5. In order to investigate further, the details of the current-composition profile obtained during discharge in the range of $0.3 \leq x \leq 0.8$ are shown (Figure 4.6).

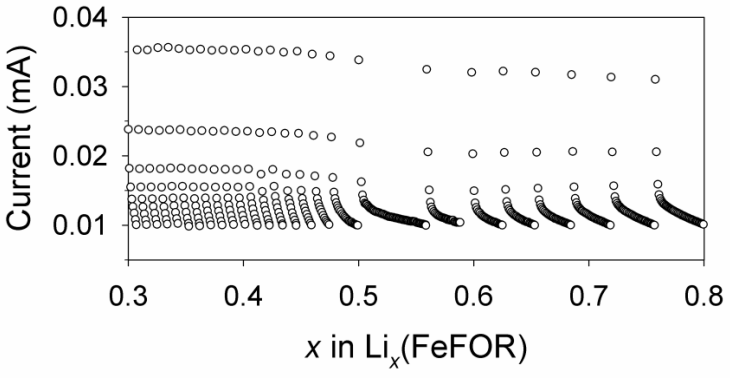

Figure 4.6 Current-composition profile of a Li/**FeFOR** cell during discharge.

During the potentiostatic measurement (10-mV potential steps), each potential step takes the system to a non-equilibrium state, producing a large initial current (Figure 4.6). Subsequently, the current slowly decays to a preset current limit (0.01 mA) as a new equilibrium state is established. Once the preset current limit is reached, another voltage step takes place. The time taken during each potential step depends on the kinetics of the process. Therefore, as the current passing through the cell is monitored during potential steps, the rate of re-equilibration can be determined.

From the current-composition profile in Figure 4.6, it is apparent from the shape of current decay that two different processes are happening in this system, and the point where a new process starts to play a role is at x in Li_x(FeFOR) equal to 0.5. In order to pursue a mechanistic study on this electrochemical system, infrared spectroscopy was used to investigate a sample recovered from a cell discharged to x = 0.5. The infrared spectrum (Figure 4.7) showed the characteristic peak of a formate ion at 1600 cm^{-1},[30,31] and suggested that formate ions were formed during the reaction.

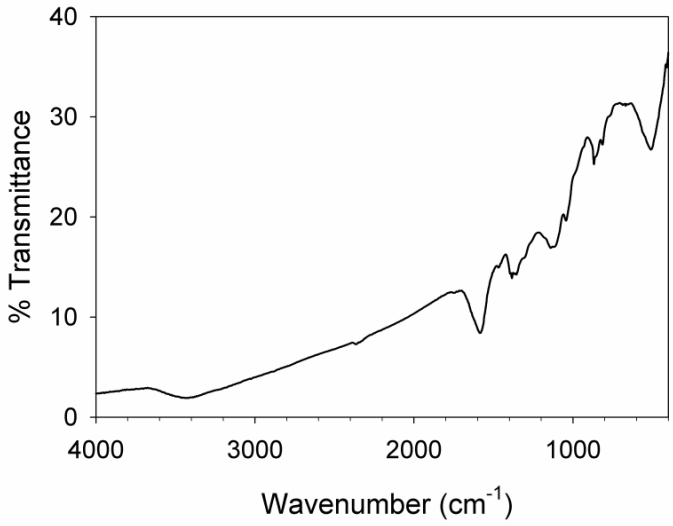

Figure 4.7 Infrared spectrum of the electrode mixture recovered from a cell discharged to $x = 0.5$ in Li_x(FeFOR).

Therefore, during discharge a cathodic reaction could be proposed as follows:

$$[NH_2(CH_3)_2][Fe^{III}Fe^{II}(HCOO)_6] + Li^+ + e^- \rightarrow Li[NH_2(CH_3)_2][Fe_2^{II}(HCOO)_6]$$

$$Li[NH_2(CH_3)_2][Fe_2^{II}(HCOO)_6] + 4Li^+ + 4e^- \rightarrow 2Fe + 5LiHCOO + [NH_2(CH_3)_2]HCOO$$

However, a thorough investigation of the reaction mechanism and phase transformation is still needed to be done in order to fully understand cathodic reaction of **FeFOR**.

4.4 Conclusions

The use of metal organic frameworks as active materials in Li-based batteries is still in its infancy. In this work, **FeFOR** was synthesized, characterized, and investigated electrochemically for an application in lithium batteries. The electrochemical performances suggest that **FeFOR** reacts reversibly with Li. A possible mechanism of the electrochemical reaction of **FeFOR** with Li was proposed. Infrared spectroscopy reveals that formate species are involved during the cycling. While the system presented here is a preliminary result, it is noteworthy that up to 2.7 Li^+ per formula unit of **FeFOR** can be reversibly inserted, which corresponds to gravimetric electrochemical capacity of 169 mAh/g.

4.5 References

[1] Tarascon, J.-M.; Armand, M. *Nature* **2001**, *414*, 359–367.

[2] Bruce, P. G. *Chem. Commun.* **1997**, 1817–1824.

[3] Owen, J. R. *Chem. Soc. Rev.* **1997**, *26*, 259–267.

[4] Rahner, D.; Machill, S.; Schlörb, H.; Siury, K.; Kloss, M.; Plieth, W. *J. Solid State Electrochem.* **1998**, *2*, 78–84.

[5] Winter, M.; Besenhard, J. O.; Spahr, M. E.; Novák, P. *Adv. Mater.* **1998**, *10*, 725–763.

[6] Goodenough, J. B.; Manthiram, A.; Wnetrzewski, B. *J. Power Sources* **1993**, *43*, 269–275.

[7] Guo, Y.-G.; Hu, J.-S.; Wan, L.-J. *Adv. Mater.* **2008**, *20*, 2878–2887.

[8] Scrosati, B.; Garche, J. *J. Power Sources* **2010**, *195*, 2419–2430.

[9] Whittingham, M. S. *Chem. Rev.* **2004**, *104*, 4271–4301.

[10] Goodenough, J. B.; Kim, Y. *J. Power Sources* **2011**, *196*, 6688–6694.

[11] Bruce, P. G.; Scrosati, B.; Tarascon, J.-M. *Angew. Chem., Int. Ed.* **2008**, *47*, 2930–2946.

[12] Winter, M.; Brodd, R. J. *Chem. Rev.* **2004**, *104*, 4245–4269.

[13] Bruce, P. G. *Solid State Ionics* **2008**, *179*, 752–760.

[14] Guyomard, D.; Tarascon, J.-M. *Adv. Mater.* **1994**, *6*, 408–412.

[15] Kitagawa, S.; Kitaura, R.; Noro, S. *Angew. Chem., Int. Ed*. **2004**, *43*, 2334–2375.

[16] Cheetham, A. K.; Rao, C. N. R.; Feller, R. K. *Chem. Commun.* **2006**, 4780–4795.

[17] Yaghi, O. M.; O'Keeffe, M.; Ockwig, N. W.; Chae, H. K.; Eddaoudi, M.; Kim, J. *Nature* **2003**, *423*, 705–714.

[18] James, S. L. *Chem. Soc. Rev.* **2003**, *32*, 276–288.

[19] Czaja, A. U.; Trukhan, N.; Müller, U. *Chem. Soc. Rev.* **2009**, *38*, 1284–1293.

[20] Tranchemontagne, D. J.; Mendoza-Cortés, J. L.; O'Keeffe, M.; Yaghi, O. M. *Chem. Soc. Rev.* **2009**, *38*, 1257–1283.

[21] Tran-Van, P.; Barthelet, K.; Morcrette, M.; Harlem, M.; Tarascon, J.-M.; Cheetham, A. K.; Férey, G. *J. New Mater. Electrochem. Syst.* **2003**, *6*, 29–34.

[22] Li, X.; Cheng, F.; Zhang, S.; Chen, J. *J. Power Sources* **2006**, *160*, 542–547.

[23] Cheng, C.-Y.; Fu, S.-J.; Yang, C.-J.; Chen, W.-H.; Lin, K.-J.; Lee, G.-H.; Wang, Y. *Angew. Chem., Int. Ed.* **2003**, *42*, 1937–1940.

[24] Férey, G.; Millange, F.; Morcrette, M.; Serre, C.; Doublet, M.-L.; Grenèche, J.-M.; Tarascon, J.-M. *Angew. Chem., Int. Ed.* **2007**, *46*, 3259–3263.

[25] De Combarieu, G.; Morcrette, M.; Millange, F.; Guillou, N.; Cabana, J.; Grey, C. P.; Margiolaki, I.; Férey, G.; Tarascon, J.-M. *Chem. Mater*. **2009**, *21*, 1602–1611.

[26] Fateeva, A.; Horcajada, P.; Devic, T.; Serre, C.; Marrot, J.; Grenèche, J.-M.; Morcrette, M.; Tarascon, J.-M.; Maurin, G.; Férey, G. *Eur. J. Inorg. Chem.* **2010**, 3789–3794.

[27] Okubo, M.; Asakura, D.; Mizuno, Y.; Kim, J. D.; Mizokawa, T.; Kudo, T.; Honma, I. J. *Phys. Chem. Lett*. **2010**, *1*, 2063–2071.

[28] Nguyen, T. L. A.; Demir-Cakan, R.; Devic, T.; Morcrette, M.; Ahnfeldt, T.; Auban-Senzier, P.; Stock, N.; Goncalves, A.-M.; Filinchuk, Y.; Tarascon, J.-M.; Férey, G. *Inorg. Chem.* **2010**, *49*, 7135–7143.

[29] Saravanan, K.; Nagarathinam, M.; Balaya, P.; Vittal, J. J. *J. Mater. Chem.* **2010**, *20*, 8329–8335.

[30] Zhao, J.-P.; Hu, B.-W.; Lloret, F.; Tao, J.; Yang, Q.; Zhang, X.-F.; Bu, X.-H. *Inorg. Chem.* **2010**, *49*, 10390–10399.

[31] Moreno, M. A.; Gálvez, O.; Maté, B.; Herrero, V. J.; Escribano, R. *J. Phys. Chem. A* **2011**, *115*, 70–75.

Chapter 5

High Capacity Microporous Molybdenum-Vanadium Oxide Electrodes for Rechargeable Lithium Batteries

* *This chapter is based on a published article:* Kaveevivitchai, W.; Jacobson, A. J. *Chem. Mater*. **2013**, *25*, 2708−2715.

5.1 Introduction

The demand for batteries with higher operating voltage and energy density, long cycle life, and rate capability has been driven by their increasing use in portable electronic devices and in electric vehicles.[1−3] In the development of rechargeable batteries, a wide range of compounds have been examined as cathode materials for rechargeable lithium batteries.[4] Among them, molybdenum and vanadium oxides have been investigated.[5] Oxides such as V_2O_5 and MoO_3 undergo intercalation of Li^+ ions into their crystal lattice; however, they have poor recharge characteristics after deep discharge, low electronic conductivity, and other drawbacks, as discussed elsewhere.[6−9,17] One of the approaches to avoid these problems is to use molybdenum-doped vanadium oxides with enhanced electronic conductivity due to an increased V^{4+} concentration produced by substitution of Mo^{6+} for V^{5+}.[10,11] Only a small number of structure types based on mixed molybdenum-vanadium oxides have been reported. Vanadium ions in V_2O_5 can be partially substituted by molybdenum ions leading to the solid solution series $(V_{1-y}Mo_y)_2O_5$ ($0 \leq y \leq 0.3$) with a random distribution of vanadium and molybdenum ions.[12,13]

Since the molybdenum ions remain Mo^{6+}, a corresponding V^{4+} concentration is present in order to maintain overall charge balance. The ideal structure can be described as a $2 \times \infty \times \infty$ shear structure based on ReO_3, composed of MO_6 octahedra forming corner-shared blocks two octahedra wide and infinite in the remaining two directions. The blocks share edges with each other, giving rise to planes of edge sharing octahedra perpendicular to the short block dimension. The metal ions are displaced off the center of the MO_6 octahedra, resulting in one very short and one exceptionally long M−O distance (2.81 Å in the pristine V_2O_5 decreasing to 2.54 Å when $y = 0.3$).[8,13,14] The layers in the V_2O_5 structure are bound together by weak V−O bonds. The presence of Mo^{6+} ions in the V_2O_5-type layers shortens the average M−O long bond length and increases the three-dimensional character of the structure. Molybdenum-substituted V_2O_5, $(V_{1-y}Mo_y)_2O_5$ ($0 \leq y \leq 0.3$), has a discharge capacity of up to 150 mAh/g between 3.0 and 1.5 V at 0.5 mA/cm^2 when used as a cathode material in a lithium cell, and shows relatively good rate capability and reversibility.[8]

Another member of the mixed molybdenum-vanadium-based oxide family is $Mo_6V_9O_{40}$, which was first reported as MoV_2O_8 by Magneli and Blomberg.[15] This compound is structurally closely related to the solid solution $(V_{1-y}Mo_y)_2O_5$ ($0 \leq y \leq 0.3$), being a $3 \times \infty \times \infty$ shear structure of a ReO_3-type lattice with off-center displacement of the metal ions.[12,13] The thickness of the slabs is the only difference between the structures of $(V_{1-y}Mo_y)_2O_5$ and $Mo_6V_9O_{40}$. The shape of the discharge curve of this phase is similar to that of $(V_{1-y}Mo_y)_2O_5$ ($0 \leq y \leq 0.3$). Li^+ ions can be inserted reversibly into the vacant

tunnels in the structure, giving a capacity of ~250 mAh/g between 3.9 and 1.7 V at 1 mA/cm^2.[16,17]

Jacobsen and co-workers investigated the electrochemical properties of $V_yMo_{2-y}O_5$, in which the homogeneity range has been determined as $1 \leq y \leq 1.14$. The structure is a three-dimensional network consisting of chains of corner-sharing VO_6 octahedra, running parallel to the *c*-axis of the tetragonal unit cell. These VO_6 octahedra chains are connected by MoO_4 tetrahedra, in such a way that each tetrahedron joins four different octahedra. This compound reversibly cycles a large amount of Li^+ between 3.0 and 1.5 V at 0.05 mA/cm^2 corresponding to a specific capacity of ~200 mAh/g, with only a minor change of the host structure while retaining its crystallinity through several cycles.[13]

The compound $LiMoVO_6$, which crystallizes with the $ThTi_2O_6$ brannerite-type structure, has been studied by Julien and co-workers.[18] The quasi-layered structure of brannerite is composed of VO_6 and MoO_6 chains along the *b*-axis. Each VO_6 and MoO_6 octahedron shares three edges to form anionic MO_6 layers. Monovalent Li^+ ions are accommodated between the anionic sheets in LiO_6 octahedral sites. On the basis of the charge-discharge profiles for lithium insertion in $LiMoVO_6$ positive electrodes between 3.5 and 1.8 V at 0.05 mA/cm^2, an initial capacity of ~200 mAh/g has been obtained. Upon cycling, however, the reversible capacity declines rapidly and instability of the brannerite structure has been observed.[18–20]

Recently, Mikhailova and co-workers have reported a new mixed molybdenum-vanadium oxide, $Li_3V(MoO_4)_3$, which has an orthorhombic NASICON-type structure and large channels that are half-filled by Li^+ ions. $Li_3V(MoO_4)_3$ is able to undergo both Li extraction and insertion while preserving the crystal structure, when cycled between 4.9 and 1.8 V at a rate of *C*/10 with an initial specific capacity of ~150 mAh/g.[21] The previous results for mixed molybdenum-vanadium oxides used as cathode materials in Li batteries are summarized in Table 5.1.

Table 5.1 Summary of Mixed Molybdenum-Vanadium Oxides Reported as Cathode Materials in Rechargeable Lithium Batteries

Compound	Composition	Voltage (V vs Li/Li^+)	Capacity (mAh/g)
$(V_{1-y}Mo_y)_2O_5$	$0 \le y \le 0.30$	1.5−3.0	150
$Mo_6V_9O_{40}$	−	1.7−3.9	250
$V_yMo_{2-y}O_5$	$1 \le y \le 1.14$	1.5−3.0	200
$LiMoVO_6$	−	1.8−3.5	200
$Li_3V(MoO_4)_3$	−	1.8−4.9	150

In the context of the previous work on mixed molybdenum-vanadium oxides, we have investigated a recently reported molybdenum-vanadium-based molecular sieve, $Mo_{2.5+y}VO_{9+\delta}$.[22,23] Microcrystalline $Mo_{2.5+y}VO_{9+\delta}$ was synthesized by hydrothermal reaction between $(NH_4)_6Mo_7O_{24}\cdot 4H_2O$ and $VOSO_4\cdot nH_2O$. The structure of this molybdenum-rich oxide has channels defined by seven-membered rings of corner-sharing MO_6 (M = $Mo^{5+/6+}$ or $V^{4+/5+}$) octahedra, and is isostructural to the orthorhombic

MoVNbTeO compounds, which are very active and selective catalysts for propane oxidation.[24–26] These mixed metal oxides have a layered orthorhombic structure, where each layer is composed of three-, six-, and seven-membered rings of corner-sharing MO_6 octahedra and pentagonal $[(M)M_5O_{27}]$ units, assembled from a MO_7 pentagonal bipyramid and five edge-sharing MO_6 octahedra (Figure 5.1). Layers are stacked together by corner-sharing to form a framework structure with three-, six-, and seven-membered ring channels. The Te atoms are located in the seven-sided channels in the MoVNbTeO compounds.[27–29] In $Mo_{2.5+y}VO_{9+\delta}$, these channels are empty. $Mo_{2.5+y}VO_{9+\delta}$ also shows outstanding catalytic activity for propane, acrolein, and alcohol oxidation reactions with molecular oxygen, without any structural degradation.[22,23] The large open channels along the crystallographic *c*-axis, which can accommodate small guest molecules, such as Li^+ ions, and the redox properties of $Mo_{2.5+y}VO_{9+\delta}$ suggest the potential of this material as a rechargeable intercalation electrode in Li-based batteries.

5.2 Experimental Section

5.2.1 Synthesis

Samples of $Mo_{2.5+y}VO_{9+\delta}$ were synthesized under hydrothermal conditions as previously reported[22,23] with some minor variations. A reaction mixture of ammonium heptamolybdate $(NH_4)_6Mo_7O_{24}\cdot 4H_2O$ (0.66 g, 0.54 mmol, dissolved in 9 mL H_2O) and vanadyl sulfate $VOSO_4\cdot nH_2O$ (0.25 g, 0.94 mmol, dissolved in 9 mL H_2O) was stirred

at room temperature for 10 min. The resulting solution was then transferred to a 23 mL Teflon-lined Parr stainless steel autoclave, where the solution was purged with nitrogen for 1 min to replace the air, and then heated at 190 °C for 48 h under autogenous pressure. A dark gray solid was obtained from the reaction by filtration, washed with a large amount of water, and dried at 80 °C for 12 h. The dried crude product (0.35 g) was then stirred in 8.75 mL of 0.4 M oxalic acid aqueous solution at 60 °C for 30 min to remove an amorphous byproduct. The solid was isolated, washed with water, and dried at 80 °C for 12 h, before being calcined at 400 °C for 2 h in air with a heating rate of 10 °C/min to remove any water and NH_4^+ from the micropores. The amount of $VOSO_4 \cdot nH_2O$ was varied from 0.57 to 1.27 mmol with a constant amount of $(NH_4)_6Mo_7O_{24} \cdot 4H_2O$ (0.54 mmol), to determine the composition range of phase homogeneity. The experimental procedure was the same for all of the syntheses.

The formation of $Li_xMo_{2.5+y}VO_{9+\delta}$ by intercalation was investigated between x = 0.1 and x = 6 by two different methods: (1) chemical reaction at ambient temperature under an argon atmosphere between $Mo_{2.5+y}VO_{9+\delta}$ and *n*-butyllithium (LiC_4H_9) in hexane as the reducing agent, and (2) in electrochemical cells.

5.2.2 Chemical Intercalation

To prepare $Li_xMo_{2.5+y}VO_{9+\delta}$, an appropriate amount of 1.6 M *n*-butyllithium (LiC_4H_9) in hexane was added to powdered $Mo_{2.5+y}VO_{9+\delta}$ under an argon atmosphere, and the resulting mixture was stirred at room temperature for a period of 3−48 h; longer

times were used for larger values of x in $Li_xMo_{2.5+y}VO_{9+\delta}$. The product of the reaction was isolated by filtration, washed with hexane to remove traces of unreacted reagent and byproducts, and dried under vacuum at room temperature. The filtrate and washings were combined and mixed with 25 mL of water. The extent of lithium intercalation was determined quantitatively by titrating the liquid mixture with a standardized aqueous HCl solution. Equilibration of the solid with a non-aqueous electrolyte solution containing Li^+ ions, 1 M $LiPF_6$ in ethylene carbonate (EC)/dimethyl carbonate (DMC) solution (1/1 by weight), for 24 h inside an argon-filled glovebox was used to ensure product homogeneity.

5.2.3 Electrochemical Studies

The electrochemical charge-discharge properties of $Mo_{2.5+y}VO_{9+\delta}$ were determined using a multichannel potentiostat-galvanostat MacPile system (Biologic SA, Claix, France) at different current densities between 3.9 and 1.5 V vs Li/Li^+ in three different cell configurations: standard Swagelok-type cells, Teflon-bag cells, and 2032 coin cells. Different cell configurations were used to check the reproducibility of the data.

5.2.3.1 Swagelok-type Cells

In a standard Swagelok-type cell, the positive electrode consisted of 75 wt% $Mo_{2.5+y}VO_{9+\delta}$, 15 wt% acetylene carbon black, and 10 wt% polyvinylidene fluoride (PVdF) binder. The mixture was hot-pressed onto a 9.5-mm-diameter aluminum disc and

dried under vacuum at 90 °C for 12 h (13 mg of active electrode material). The negative electrode was lithium foil supported on a current collector. The two electrodes were separated by a Celgard 2400 membrane immersed in 1 M $LiPF_6$ in ethylene carbonate (EC)/dimethyl carbonate (DMC) solution (1/1 by weight), which was used as the electrolyte. The cells were assembled in an argon-filled glovebox.

5.2.3.2 Teflon-bag Cells

The same electrode mixture was used in a Teflon-bag cell. Positive electrodes were prepared by hot pressing the mixture into a stainless steel grid which served as a current collector to give 1 cm^2 of active area (20 mg of active electrode material). The electrodes were dried in vacuum at 90 °C for 12 h, before being transferred to the glovebox in which the cells were assembled. Cells were constructed by surrounding the cathodes with Celgard 2400 membranes and then lithium foils, which served as negative electrodes. The assembled cells were immersed in the electrolyte contained in Teflon bags. The electrolyte consisted of a solution of 1 M $LiPF_6$ in ethylene carbonate (EC)/dimethyl carbonate (DMC) (1/1 by weight). The cells were clamped between glass slides to ensure good inside contacts.

5.2.3.3 Coin Cells

Electrochemical measurements were made using 2032-type coin cells. The cells had a lithium metal negative electrode separated from the positive electrode by a Celgard

2400 membrane. The positive electrodes with the same ratio of the active material, acetylene black, and polyvinylidene fluoride (PVdF) were prepared by hot-pressing the electrode mixture on an aluminum disc (16 mm in diameter with 56 mg of active electrode material). The electrolyte used was 1 M $LiPF_6$ dissolved in ethylene carbonate (EC)/dimethyl carbonate (DMC) solution (1/1 by weight). The cells were assembled in an argon-filled glovebox. Electrochemical testing conditions are specified in the Results and Discussion section.

5.2.4 Chemical Deintercalation

After lithium intercalation into the framework structure of $Mo_{2.5+y}VO_{9+\delta}$ was complete, an iodine (I_2) solution in acetonitrile (CH_3CN) was used as an oxidizing agent to deintercalate the Li^+ ions. A 0.2 M solution of I_2 in CH_3CN was prepared by dissolving freshly sublimed I_2 crystals in anhydrous CH_3CN. An appropriate stoichiometric amount of the I_2 solution was added to the lithiated $Mo_{2.5+y}VO_{9+\delta}$ under an argon atmosphere, and the resulting mixture was stirred at room temperature for 24 h. The product was isolated by filtration, thoroughly washed with CH_3CN, and dried under vacuum at room temperature. The filtrate and washings were combined. The extent of lithium deintercalation was determined quantitatively by titration of the liquid mixture with a standardized sodium thiosulfate ($Na_2S_2O_3$) solution in water, using starch as an indicator. Equilibration of the solid with a non-aqueous electrolyte solution containing Li^+ ions, 1 M $LiPF_6$ in ethylene carbonate (EC)/dimethyl carbonate (DMC) solution (1/1 by weight), for 24 h inside an argon-filled glovebox was used to ensure homogeneity.

5.2.5 Materials Characterization

Phase analysis and determination of cell parameters were performed using powder X-ray diffraction (XRD) with a Phillips PANalytical X'Pert PRO diffractometer with Cu Kα radiation (λ = 1.54046 Å) at room temperature. Phase analyses of $Li_xMo_{2.5+y}VO_{9+\delta}$ were performed in a sealed sample holder to avoid any contact with air. Extraction of the peak positions, pattern indexing, and profile refinements were carried out using GSAS. Scanning electron microscopy (SEM) was performed on a JSM-6330F (JEOL). Elemental Analysis was carried out by Galbraith Laboratories (Knoxville, TN).

5.2.6 Thermogravimetric Analysis

The thermal behavior of the compounds synthesized was investigated on a TA Instruments Hi-Res 2950 thermogravimetric analyzer. Approximately 25 mg of powder was heated using a heating rate of 2 °C/min from room temperature up to 600 °C in an alumina sample pan under a flowing oxygen atmosphere.

5.3 Results and Discussion

5.3.1 Synthesis

Microcrystalline $Mo_{2.5+y}VO_{9+\delta}$ can be prepared by the hydrothermal method previously described. Solutions of ammonium heptamolybdate and vanadyl sulfate prepared separately were combined together to give a dark violet solution where the pentagonal $[(Mo)Mo_5O_{27}]$ units form.[30] This pentagonal $[(Mo)Mo_5O_{27}]$ building block is

assembled from a MoO_7 pentagonal bipyramid and five edgesharing MoO_6 octahedra (Figure 5.1c). After the solution is purged with N_2 gas and the temperature is raised to 190 °C in a sealed reactor, the pentagonal units, together with other molybdenum and vanadium species assemble further into the complex mixed Mo-V oxide.[30] After 48 h, the solid crude product can be obtained together with an amorphous byproduct which can be removed by the use of an aqueous solution of oxalic acid. The removal of the amorphous phase was monitored by powder XRD and disappearance of the blue color of the filtrate after the acid washing. The acid-washed sample was dried overnight at 80 °C; the micropores, however, are still occupied by water and NH_4^+ molecules.[23] To unblock the channels, the sample was calcined in air at 400 °C for 2 h, to give the open microporous structure shown in Figure 5.1.

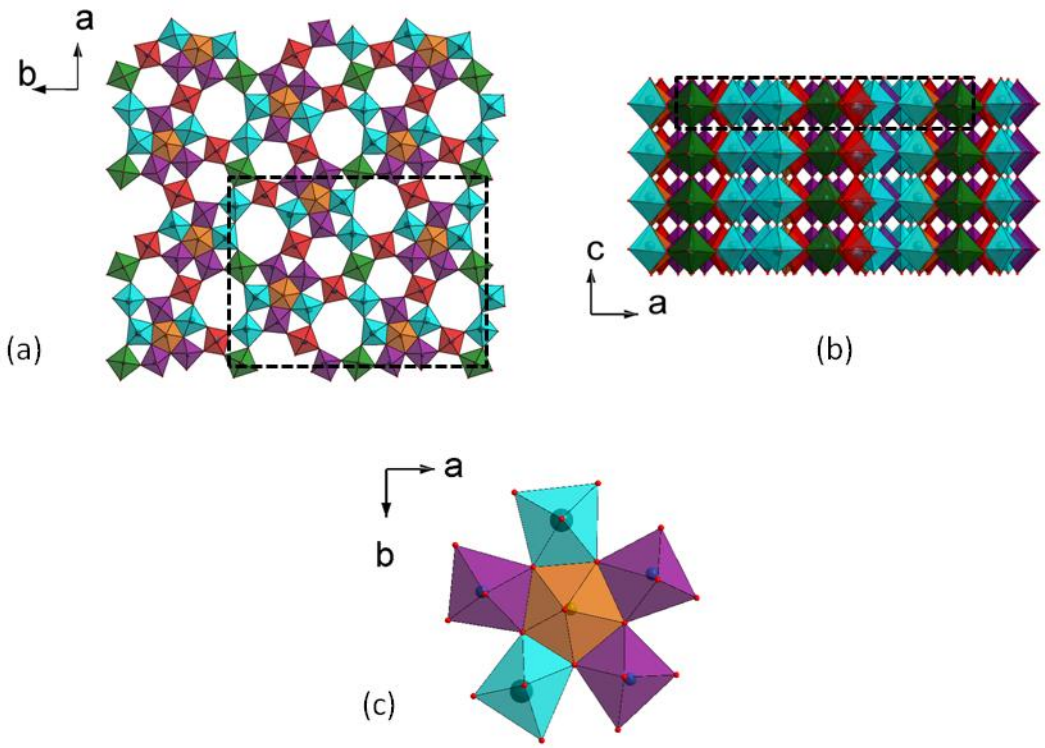

Figure 5.1 (a) Structure of the microporous $Mo_{2.5+y}VO_{9+\delta}$ framework viewed down the *c*-axis showing the connectivity of the three-, six-, and seven-membered rings; the metal ions in the polyhedra shown in different colors were predicted theoretically to have different oxidation states and occupancies of molybdenum and vanadium cations: green, Mo^{5+}/V^{4+}; red, Mo^{6+}/V^{5+}; blue, Mo^{6+}/Mo^{5+}; orange, Mo^{5+}; and purple, Mo^{6+}. (b) Projection of the *a*-*c* plane. (The unit cell is highlighted with dashed line.) (c) Pentagonal $[(M)M_5O_{27}]$ building block unit assembled from a MO_7 pentagonal bipyramid and five edge-sharing MO_6 octahedra.

The amount of N_2 used to purge the solution (in terms of the flow rate and the length of purging time) is critical to the amount of oxygen in the final product. The shorter the amount of time that the reaction mixture is exposed to the N_2, the higher the δ in $Mo_{2.5+y}VO_{9+\delta}$, as confirmed by thermogravimetric experiments performed in an oxygen gas flow. The TGA data (Figure 5.2) show that a weight loss occurs between 35 and 300 °C corresponding to water evaporation and NH_4^+ decomposition in the micropores (3.92% weight loss measured, 3.86% calculated, which is equivalent to 1 molecule of H_2O/NH_4^+ per formula unit or 1 molecule of H_2O/NH_4^+ per six-, or seven-sided channel in the unit cell), leading to the microporous $Mo_{2.5+y}VO_{9+\delta}$ framework. The structure after removal of the guest molecules is stable in the oxygen atmosphere up to approximately 500 °C before the oxidation of $Mo_{2.5+y}VO_{9+\delta}$ occurs at 530 °C, corresponding to the weight gain in the final step (0.29% weight gain). The residue from the TGA study was confirmed by powder XRD to be the mixture of MoO_3 and MoV_2O_8. From the weight gain in this final process, it is possible to calculate the amount of oxygen in this particular sample, z in $Mo_{2.5+y}VO_z$ (z = 9.93). It is noteworthy that z = 9.93 in $Mo_{2.5+y}VO_z$ decreases to 9.86 when the time that the reaction mixture is exposed to the N_2 increases by 50%. According to elemental analysis, the Mo:V ratio of this sample was 2.48:1 per formula unit.

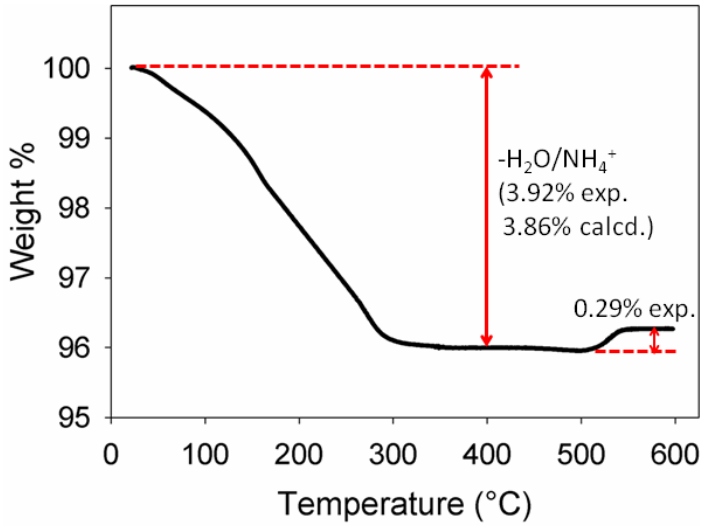

Figure 5.2 Thermogravimetric analysis of $Mo_{2.5+y}VO_{9+\delta}$ under an oxygen flow from 25 to 600 °C at 2 °C/min.

5.3.2 Structure and Morphology

The structure and phase purity of $Mo_{2.5+y}VO_{9+\delta}$ were confirmed by analyzing the powder XRD data using the profile method. The X-ray diffraction pattern is shown in Figure 5.3. The profile refinement indicated an orthorhombic space group, *Pba*2 (wR_p = 2.87%) with lattice parameters a = 21.0505(3) Å, b = 26.3766(5) Å, and c = 4.0144(1) Å, which are very close to those reported by Sadakane et al.[23] The structure of $Mo_{2.5+y}VO_{9+\delta}$ can be described as a layered structure where each layer is made from corner-sharing MO_6 octahedra and pentagonal [(M)-M_5O_{27}] units, and the layers are joined together by corner-sharing to form the three-dimensional microporous framework with three-, six-, and seven-membered ring channels. The size of the empty tunnels available for guest

molecules from the space-filling model is approximately 3 Å in diameter for six-membered ring channels and 5 Å for seven-membered ring channels.

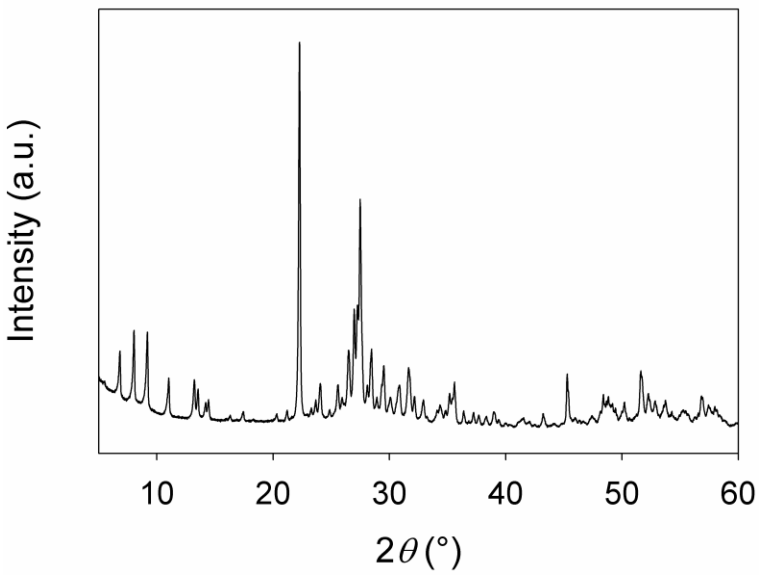

Figure 5.3 Powder X-ray diffraction pattern of microporous $Mo_{2.5+y}VO_{9+\delta}$ (2θ = 5−60°).

SEM images of $Mo_{2.5+y}VO_{9+\delta}$ show uniform rod-like crystals with the size of up to tens of micrometers in length and 200 nm in diameter (Figure 5.4). The crystallographic *c* direction is along the length of the crystal. Figure 5.5 illustrates the cross-sectional projection of a rod-like crystal (*a*-*b* plane), showing the open channels which can accommodate diffusion of small guest species, such as Li^+ ions.

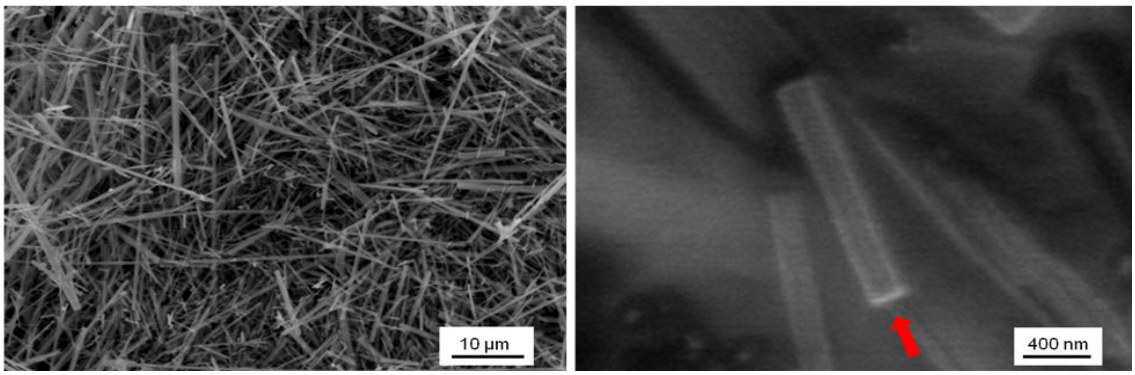

(a) (b)

Figure 5.4 SEM images of the rod-like orthorhombic $Mo_{2.5+y}VO_{9+\delta}$ crystals (200 nm in diameter). Red arrow in (b) pointing along the length of the crystal which is the *c* direction.

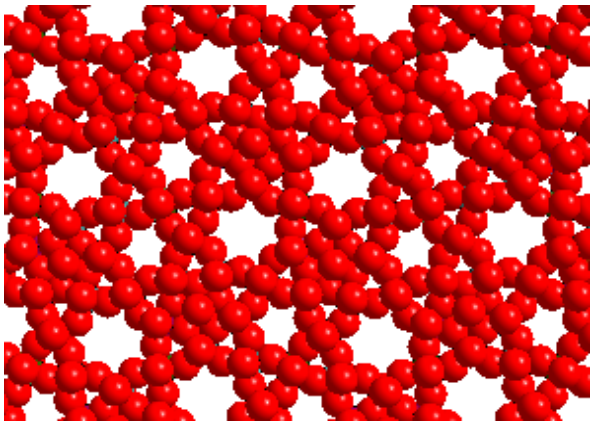

Figure 5.5 Space-filling model of the cross-section of a rod-like $Mo_{2.5+y}VO_{9+\delta}$ crystal (*a*-*b* plane); oxygen in red.

In addition to the original synthesis of $Mo_{2.5+y}VO_{9+\delta}$ (0.54 mmol $(NH_4)_6Mo_7O_{24}\cdot 4H_2O$ and 0.94 mmol $VOSO_4\cdot nH_2O$ used), the products obtained by varying the ratio of the reactants (0.57−1.27 mmol $VOSO_4\cdot nH_2O$ with a constant amount (0.54 mmol) of $(NH_4)_6Mo_7O_{24}\cdot 4H_2O$) were also investigated. The reactions still yield a pure single phase of microcrystalline orthorhombic $Mo_{2.5+y}VO_{9+\delta}$ when the amount of $VOSO_4.nH_2O$ is between 0.67 and 1.14 mmol, as confirmed by powder XRD. Figure 5.6a shows the chemical composition of the final products, determined by elemental analyses as a function of the amount of $VOSO_4\cdot nH_2O$ used (mmol) in each synthesis. Within the homogeneity range of the orthorhombic phase, the higher the content of $VOSO_4\cdot nH_2O$ in the reaction mixture, the more vanadium is incorporated into the structure. The ratio of Mo/V in the structure is, therefore, smaller. As a result, it can be concluded that this new molybdenum-vanadium-based molecular sieve, $Mo_{2.5+y}VO_{9+\delta}$, does not have a single composition as reported, but variable composition in the range $-0.13 \leq y \leq 0.05$.

The compounds with different compositions were shown to be single phase by X-ray diffraction, and the lattice parameters together with unit cell volumes were determined by the profile refinement method (Figure 5.6b). The individual lattice parameters follow a clear trend. As y in $Mo_{2.5+y}VO_{9+\delta}$ varies from low to high, the a and c lattice parameters stay relatively constant, while those for b axis decrease as does the unit cell volume, V.

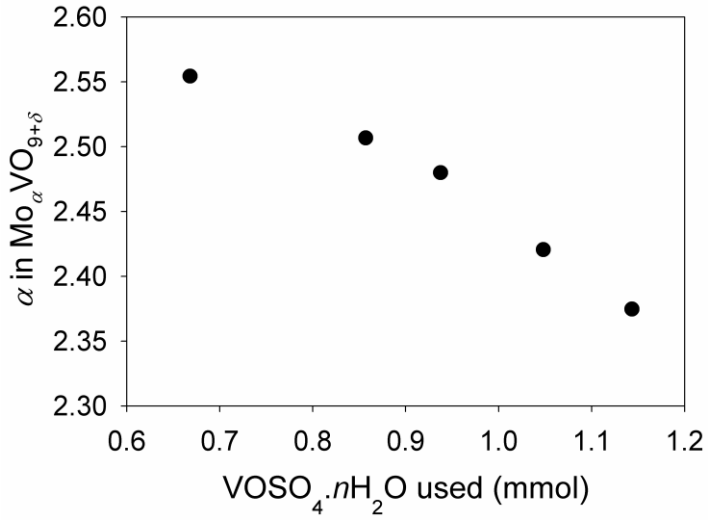

(a)

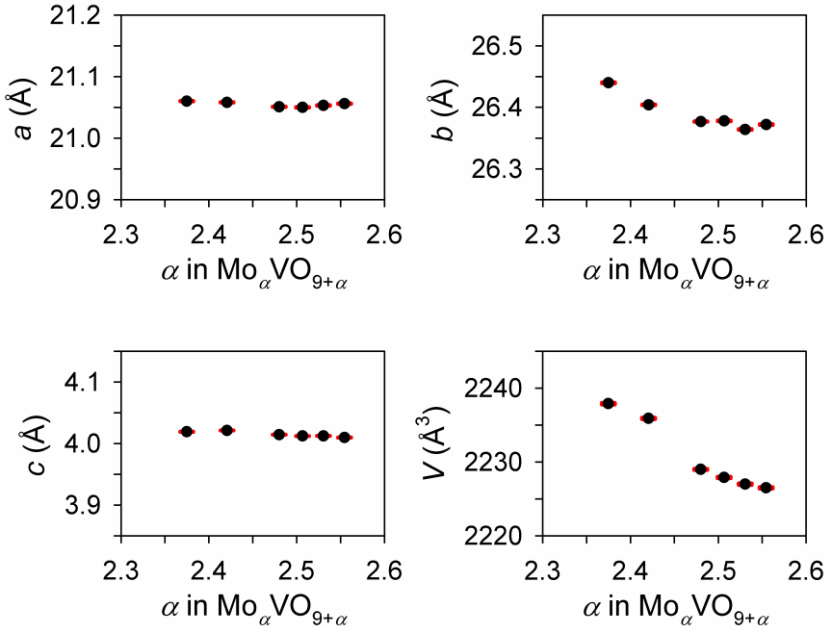

(b)

Figure 5.6 (a) Chemical compositions of the products as a function of the amount of $VOSO_4 \cdot nH_2O$ used (mmol) in each synthesis. (b) Lattice parameters and cell volumes of $Mo_\alpha VO_{9+\delta}$ ($Mo_{2.5+y}VO_{9+\delta}$) phases (error bars in red).

5.3.3 Electrochemical Behavior of $Mo_{2.5+y}VO_{9+\delta}$

In order to investigate the electrochemical properties of $Mo_{2.5+y}VO_{9+\delta}$ as an intercalation electrode material, we chose the original composition, $Mo_{2.48}VO_{9.93}$.

For room temperature galvanostatic cycling, electrodes composed of $Mo_{2.48}VO_{9.93}$ were discharged and charged in a lithium cell with metallic Li as the negative electrode, at a rate of 1 Li in 7 h or *C*/7 (0.15 mA/cm^2) with an open circuit voltage (OCV) of 3.7 V.[21,31–34] The first electrochemical cycle obtained from a Swagelok-type cell is shown in Figure 5.7. The same result was also observed from a coin cell. The profile shows that 6 Li^+ ions per formula unit can be reversibly inserted into and removed from $Mo_{2.48}VO_{9.93}$ between 3.9 and 1.5 V, with a pronounced plateau at 2.4 V and a very short one at 1.75 V; the total capacity corresponds to 345 mAh/g. Due to the nature of $Mo_{2.5+y}VO_{9+\delta}$ framework where molybdenum and vanadium ions ($Mo^{5+/6+}$ or $V^{4+/5+}$) have mixed occupation of crystallographic sites and the uncertainty of local oxygen environments, it is difficult to identify the redox couples and the processes taking place over the discharge range from 3.7 V down to 1.5 V (first cycle). Presumably, all of the metal ions (Mo^{5+}, Mo^{6+}, V^{4+}, and V^{5+}) actively participate in the electrochemical lithium intercalation, where the metal ions are reduced as Li^+ is inserted into the structure and oxidized during deintercalation. The second discharge is quite different from the first, having a smooth curve without any distinct plateaus (red curve in Figure 5.7). This behavior is similar to that previously reported for mixed molybdenum-vanadium oxides cycled in lithium cells, where plateaus were observed only upon reduction during the first discharge.

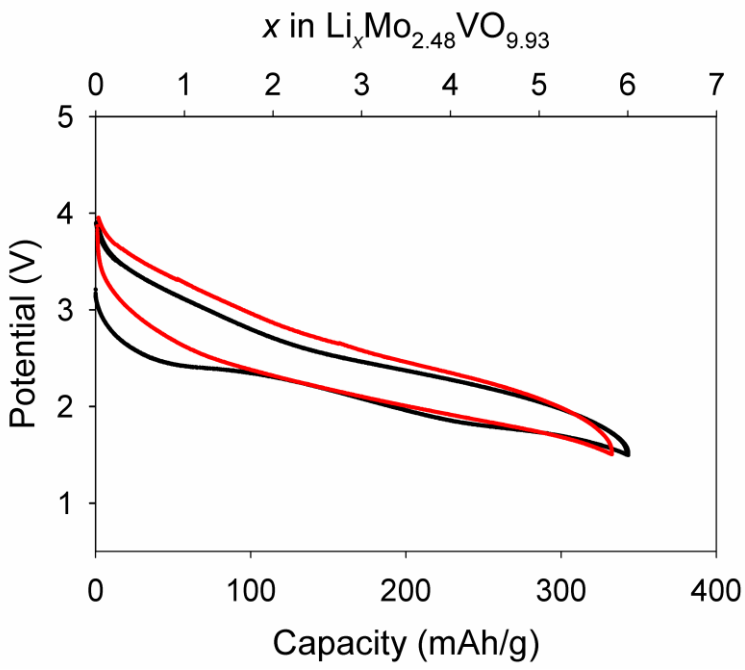

Figure 5.7 Electrochemical profile of a Li/$Mo_{2.48}VO_{9.93}$ Swagelok-type cell cycled between 3.9 and 1.5 V at a rate of *C*/7 (0.15 mA/cm^2), 1st cycle in black and 2nd cycle in red.

The discharge voltage profiles of $Mo_{2.48}VO_{9.93}$ at various *C* rates ranging from *C*/20 (0.05 mA/cm^2) to 10*C* (10 mA/cm^2) are shown in Figure 5.8. With increasing discharge rate, the discharge potential decreases due to kinetic effects. With a cutoff voltage of 1.5 V, the cells gave a discharge capacity ranging from 190 up to 370 mAh/g, depending on the cycling rate. It is noteworthy that at a really fast discharge rate of 10*C* (1 Li in 6 min), a discharge capacity as high as 190 mAh/g can be obtained. The excellent rate capability and high capacity of the electrodes can be attributed to the following: (a) the open three-dimensional porous framework structure of $Mo_{2.48}VO_{9.93}$ with large empty

tunnels. As a result, Li^+ with an effective ionic radius of 0.76 Å can rapidly diffuse into the channels, and the framework can accommodate a large amount of Li^+; (b) the small size of $Mo_{2.48}VO_{9.93}$ rod-like crystals (200 nm in diameter and micrometers in length) provides large contact area between the active material and the $LiPF_6$ electrolyte, resulting in short diffusion paths for Li^+ ions thereby enhancing the rate capability.

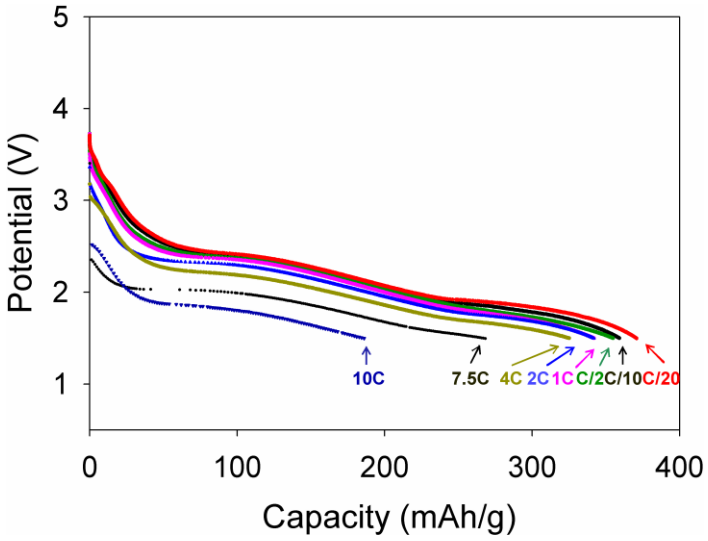

Figure 5.8 Rate performance of $Li/Mo_{2.48}VO_{9.93}$ Teflon-bag cells at various discharge rates: 10*C* = 10 mA/cm^2, 7.5*C* = 8 mA/cm^2, 4*C* = 4 mA/cm^2, 2*C* = 2 mA/cm^2, 1*C* = 1 mA/cm^2, *C*/2 = 0.5 mA/cm^2, *C*/10 = 0.1 mA/cm^2, and *C*/20 = 0.05 mA/cm^2.

Results of repeated galvanostatic cycling of a $Li/Mo_{2.48}VO_{9.93}$ cell with a rate of *C*/5 are shown in Figure 5.9. The reversible specific capacity vs cycle number shows a capacity decline during initial cell cycles followed by stable capacity retention of ~200 mAh/g. The irreversible capacity loss during the first few cycles may correspond to part

of Li^+ ions becoming trapped in the framework in the small three-membered ring channels. Once these small sites are filled, Li^+ can transport in and out of the six- and seven-membered ring tunnels reversibly without further capacity loss.

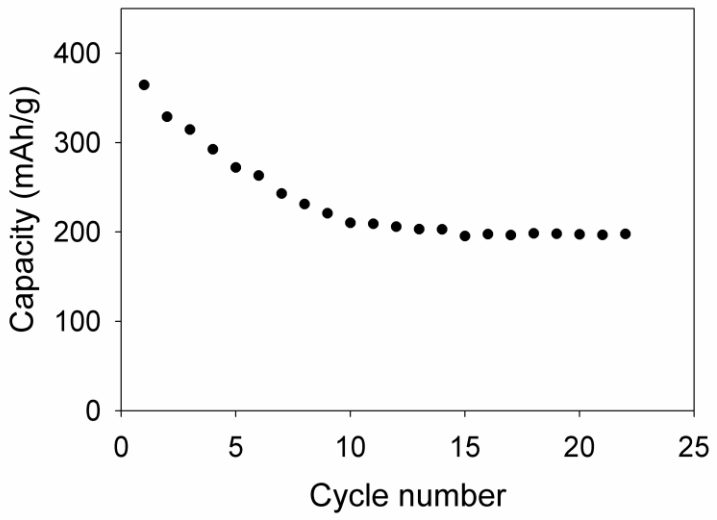

Figure 5.9 Capacity retention data for galvanostatic cycling of a Li/$Mo_{2.48}VO_{9.93}$ Teflon-bag cell at *C*/5 (0.3 mA/cm^2).

In order to compare the electrochemical performance of an electrode made from a mixture of $Mo_{2.48}VO_{9.93}$, acetylene black, and PVdF to that of an electrode prepared from $Mo_{2.48}VO_{9.93}$ only without any conducting additive and binder (the electrode without additive and binder was prepared by hot-pressing the pure active material onto a stainless steel grid), two Teflon-bag cells were assembled and discharged at the same current density of *C*/5 (0.3 mA/cm^2). The discharge data are shown in Figure 5.10. For $x < 0.8$ in $Li_xMo_{2.48}VO_{9.93}$, the two curves are different. The voltage from the $Mo_{2.48}VO_{9.93}$-only

electrode drops rapidly at the beginning, whereas a slow voltage drop is observed in case of the electrode with additives. At $x > 0.8$, the two curves converge and follow the same trend with two plateaus at 2.38 and 1.73 V, and reach $x = 6.4$ at 1.5 V cutoff voltage. This result demonstrates that once some Li^+ ions are introduced into $Mo_{2.48}VO_{9.93}$, the electronic conductivity becomes comparable for electrodes with and without added carbon. The measured resistivities at ambient temperature of $Mo_{2.48}VO_{9.93}$ and $Li_{4.5}Mo_{2.48}VO_{9.93}$ were ~1.5×10^6 Ω·cm and ~4.7×10^4 Ω·cm, respectively.

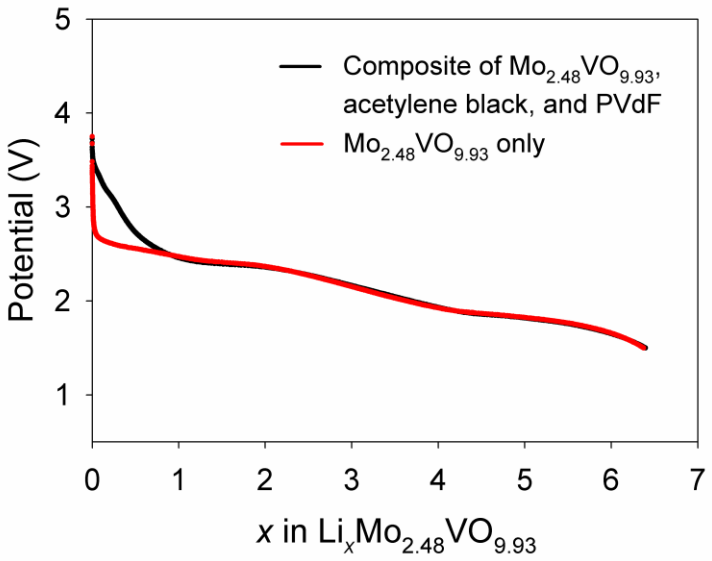

Figure 5.10 Potential-composition profiles of electrodes made from a mixture of active material, acetylene black, and PVdF and from the active material only (galvanostatic discharge of Teflon-bag cells at 0.3 mA/cm^2, *C*/5).

5.3.4 Chemical Redox Studies of $Mo_{2.48}VO_{9.93}$ using Reducing and Oxidizing Agents

To further understand the structural evolution of $Mo_{2.48}VO_{9.93}$ upon lithium insertion and extraction, X-ray diffraction data were obtained for chemically reduced $Mo_{2.48}VO_{9.93}$ ($Li_xMo_{2.48}VO_{9.93}$, x = 0.1 to x = 6). As described earlier, *n*-BuLi can be used as a reducing agent to prepare $Li_xMo_{2.48}VO_{9.93}$ from $Mo_{2.48}VO_{9.93}$ in a ratio according to the reaction: $Mo_{2.48}VO_{9.93} + xC_4H_9Li \rightarrow Li_xMo_{2.48}VO_{9.93} + x/2C_8H_{18}$.[35] The x value was confirmed by titration of the filtrate which had been hydrolyzed, with a standardized aqueous HCl solution to determine the amount of *n*-BuLi left over from the reaction. Because hexane was used as the reaction medium during the chemical intercalation, the product $Li_xMo_{2.48}VO_{9.93}$ was subsequently equilibrated in the electrolyte (1 M $LiPF_6$ solution in EC/DMC) by stirring for 24 h, to ensure compositional homogeneity among the lithiated particles. X-ray diffraction measurements were performed on $Li_xMo_{2.48}VO_{9.93}$ using a sealed sample holder loaded in the glovebox. The resulting diffraction patterns are shown in Figure 5.11, and lattice parameters determined by profile refinement using the GSAS program are summarized in Figure 5.12. Figure 5.13 gives an example of the refinement of the pristine $Mo_{2.48}VO_{9.93}$ for comparison with $Li_xMo_{2.48}VO_{9.93}$ (x = 2).

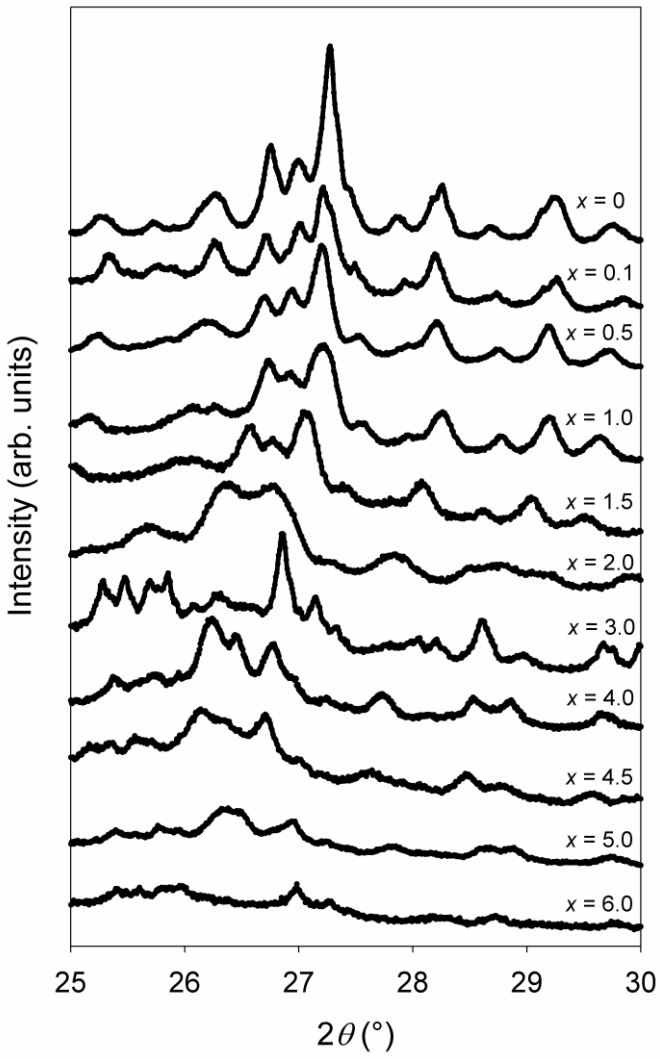

Figure 5.11 X-ray diffraction patterns of $Li_xMo_{2.48}VO_{9.93}$, illustrating the changes occurring in the range of $x = 0 \rightarrow 6$. The samples were prepared by chemical reduction using *n*-BuLi, selected 2θ range (25−30°).

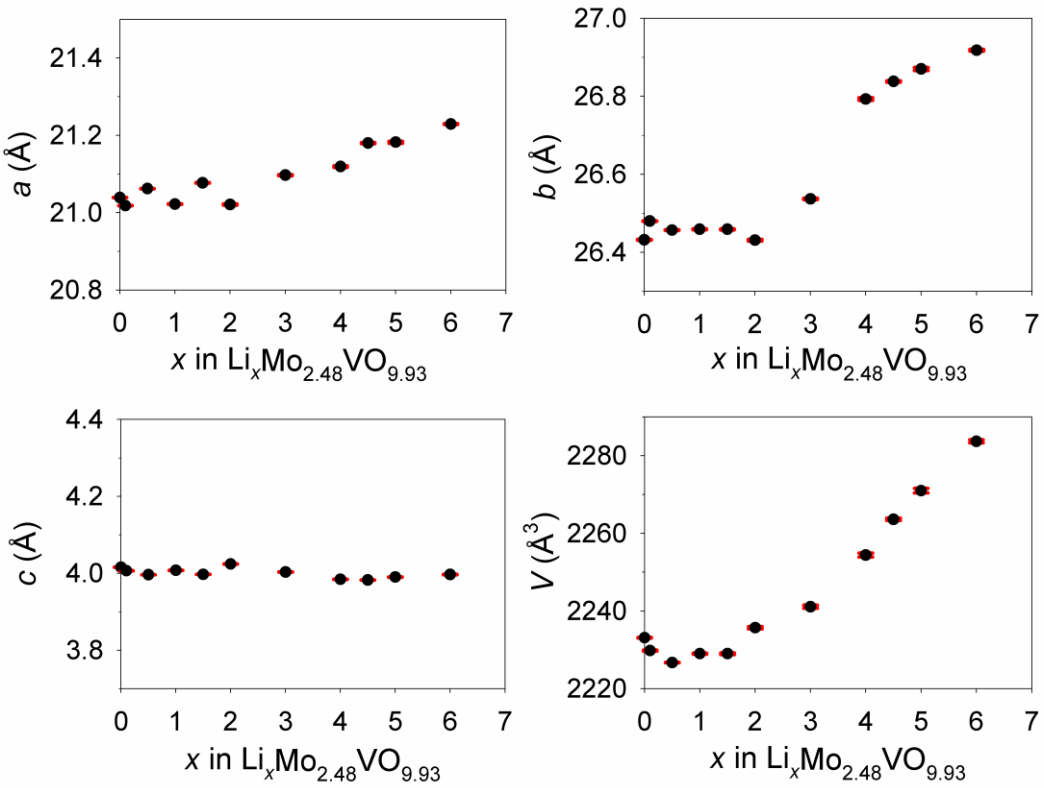

Figure 5.12 Lattice parameters and unit cell volume of chemically prepared $Li_xMo_{2.48}VO_{9.93}$ refined by profile fitting.

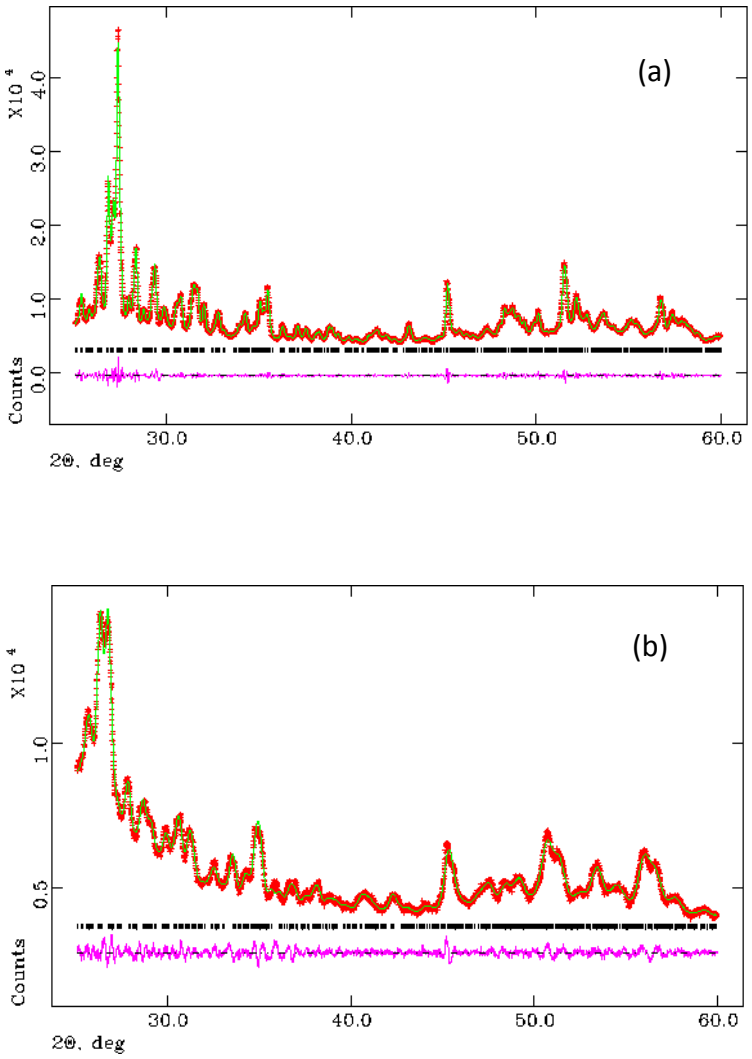

Figure 5.13 (a) Le Bail XRD refinement of pristine $Mo_{2.48}VO_{9.93}$. (b) The refinement of $Li_2Mo_{2.48}VO_{9.93}$ synthesized from $Mo_{2.48}VO_{9.93}$ reduced with *n*-BuLi in *Pba*2, wR_p = 2.54%: lattice parameters a = 21.021(2) Å, b = 26.431(2) Å, and c = 4.0240(2) Å. (The measured data are shown in orange, the calculated data are shown in green, and the difference is shown in pink. Bragg reflections are shown by vertical tick marks.)

The characterization of the phases of chemically prepared $Li_xMo_{2.48}VO_{9.93}$ ($0 \leq x \leq 6$) are in good agreement with the voltage profile shown in Figure 5.7. Starting from the pristine $Mo_{2.48}VO_{9.93}$, the electrochemical insertion of Li^+ ions into crystalline $Mo_{2.48}VO_{9.93}$ takes place through a two-phase equilibrium, which can be easily identified by the presence of a potential plateau at 2.4 V on the galvanostatic discharge curve. When Li^+ ions are inserted into $Li_xMo_{2.48}VO_{9.93}$ (from $x = 0$ to ca. 1), a gradual decrease of cell potential is observed which corresponds to a monophasic solid solution, as confirmed by the PXRD patterns; the unit cell volume decreases in this region. For $x = 1 \rightarrow$ ca. 2, the phase $Li_xMo_{2.48}VO_{9.93}$ ($x = 0-1$) is in equilibrium with the second solid solution phase that is formed when $2 \leq x \leq 4$. A distinct change in unit cell parameters is observed at $x = 2$. The profile refinements suggest that $Li_xMo_{2.48}VO_{9.93}$ ($2 \leq x \leq 4$) has a similar structure to the parent compound, and the orthorhombic *Pba*2 structure is maintained; the *a* and *b* lattice parameters increase while the *c* lattice parameters decrease slightly for $2 \leq x \leq 4$ (Figure 5.12).

Further intercalation results in a very short voltage plateau compared to the first one at ca. $x = 4.5$, and the process taking place at this point is not understood. At $x > 5$, no plateau is observed, consistent with the lithiation occurring in a single phase. Thus $Li_xMo_{2.48}VO_{9.93}$ ($5 \leq x \leq 6$) can be considered as a solid solution. The lattice parameters of $Li_xMo_{2.48}VO_{9.93}$ ($x = 6$) with space group *Pba*2 show that the unit cell volume of $Li_6Mo_{2.48}VO_{9.93}$ is only 2% larger than that of the parent compound due to the guest insertion. Overall, there is a clear trend in the lattice parameters: the *a* and *b* lattice

parameters increase, while the *c* lattice parameters which correspond to the layer stacking direction remain relatively constant.

During charge, deintercalation of lithium occurs and the phase transition results in solid-solution-like electrochemical behavior with sloping voltage profile over the range from $x = 6 \rightarrow x = 0$. To chemically illustrate the reversibility of the electrochemical reaction of $Mo_{2.48}VO_{9.93}$ in the lithium cell, chemically prepared $Li_4Mo_{2.48}VO_{9.93}$ (by *n*-BuLi) was oxidized by using I_2 in CH_3CN as the oxidizing agent in a ratio according to the reaction: $Li_4Mo_{2.48}VO_{9.93} + [(4 - x)/2]I_2 \rightarrow Li_xMo_{2.48}VO_{9.93} + (4 - x)LiI$.[36] The oxidation was rapid, and the reaction was complete when the darkly colored I_2 solution became colorless. The *x* value was confirmed to be $x = 3$ by titrating the filtrate with a standardized $Na_2S_2O_3$ aqueous solution to determine any trace amount of I_2 left over. After the equilibration of the product $Li_3Mo_{2.48}VO_{9.93}$ in the electrolyte, the X-ray diffraction pattern well matched with the one in Figure 5.11 for $x = 3$. The comparison of the X-ray diffraction data obtained for chemically prepared $Li_4Mo_{2.48}VO_{9.93}$ (by *n*-BuLi), $Li_3Mo_{2.48}VO_{9.93}$ by deintercalation, and $Li_3Mo_{2.48}VO_{9.93}$ prepared by intercalation using *n*-BuLi is shown in Figure 5.14. The result confirms that some structural reorganization, as indicated by the electrochemical data, does occur but nevertheless lithium intercalation into $Mo_{2.48}VO_{9.93}$ is reversible.

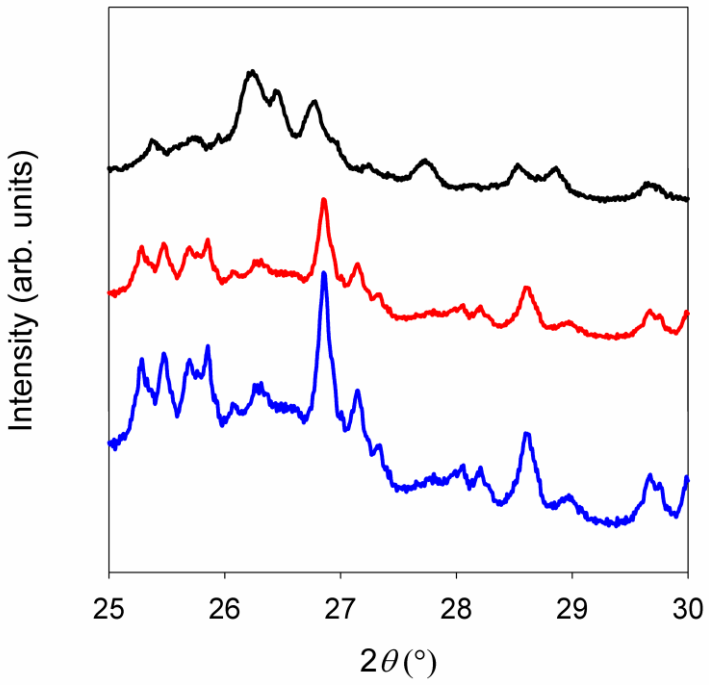

Figure 5.14 X-ray diffraction patterns of $Li_4Mo_{2.48}VO_{9.93}$ chemically prepared by *n*-BuLi (in black), $Li_3Mo_{2.48}VO_{9.93}$ prepared by deintercalation of $Li_4Mo_{2.48}VO_{9.93}$ using I_2 in CH_3CN as the oxidizing agent (in red), and $Li_3Mo_{2.48}VO_{9.93}$ chemically prepared by intercalation using *n*-BuLi (in blue), selected 2θ range (25−30°).

5.4 Conclusions

The newly reported mixed molybdenum-vanadium oxide, $Mo_{2.5+y}VO_{9+\delta}$ has been found to adopt a composition in the range $-0.13 \leq y \leq 0.05$. The compound behaves as a rechargeable intercalation electrode material in Li-based batteries. $Mo_{2.48}VO_{9.93}$ has good electronic conductivity and can be reversibly cycled in an electrochemical cell with lithium as the counter electrode at rates up to 10*C* with good specific capacity. The

structural changes associated with the electrochemical reaction have been characterized through ex-situ X-ray diffraction of phases prepared by a chemical route. Li^+ ions can be reversibly intercalated into $Mo_{2.48}VO_{9.93}$ up to $x = 6$ in $Li_xMo_{2.48}VO_{9.93}$ with only 2% increase in unit cell volume compared to that of the parent compound. Large open channels along the crystallographic *c*-axis of $Mo_{2.48}VO_{9.93}$ framework could account for the high lithium storage capacity with small unit cell volume expansion, which reduces lattice strain and helps with intercalation reversibility. By further understanding of the mechanism of the reactions involved and modification of the basic framework in terms of composition and structure, these electrochemical properties may be further improved.

5.5 References

[1] Armand, M.; Tarascon, J.-M. *Nature* **2008**, *451*, 652−657.

[2] Goodenough, J. B.; Kim, Y. *Chem. Mater*. **2010**, *22*, 587−603.

[3] Scrosati, B.; Hassoun, J.; Sun, Y.-K. *Energy Environ. Sci*. **2011**, *4*, 3287−3295.

[4] Whittingham, M. S. *Chem. Rev*. **2004**, *104*, 4271−4301.

[5] Chernova, N. A.; Roppolo, M.; Dillon, A. C.; Whittingham, M. S. *J. Mater. Chem.* **2009**, *19*, 2526−2552.

[6] Delmas, C.; Cognac-Auradou, H.; Cocciantelli, J. M.; Ménétrier, M.; Doumerc, J. P. *Solid State Ionics* **1994**, *69*, 257−264.

[7] Murphy, D. W.; Christian, P. A. *Science* **1979**, *205*, 651−656.

[8] Fiordiponti, P.; Pasquali, M.; Pistoia, G.; Rodante, F. *J. Power Sources* **1982**, *7*, 133−143.

[9] Pasquali, M.; Pistoia, G.; Rodante, F. *J. Power Sources* **1982**, *7*, 145−152.

[10] Robb, F. Y.; Glaunsinger, W. S. *J. Solid State Chem.* **1979**, *30*, 171−181.

[11] Uchiyama, M.; Slane, S.; Plichta, E.; Salomon, M. *J. Electrochem. Soc*. **1989**, *136*, 36−42.

[12] Delmas, C.; Cognac-Auradou, H. *J. Power Sources* **1995**, *54*, 406−410.

[13] West, K.; Zachau-Christiansen, B.; Skaarup, S.; Jacobsen, T. *Solid State Ionics* **1992**, *53*, 356−363.

[14] Eguchi, M.; Maki, F.; Iwabe, S.; Momose, Y. *J. Power Sources* **2001**, *97*, 548−550.

[15] Magneli, A.; Blomberg, B. *Acta Chem. Scand*. **1951**, *5*, 585−589.

[16] Takeda, Y.; Kanno, R.; Tanaka, T.; Yamamoto, O. *J. Electrochem. Soc*. **1987**, *134*, 641−643.

[17] Tranchant, A.; Messina, R. *J. Power Sources* **1988**, *24*, 85−93.

[18] Amdouni, N.; Zarrouk, H.; Soulette, F.; Julien, C. M. *J. Mater. Chem*. **2003**, *13*, 2374−2380.

[19] Liang, Y.; Han, X.; Cong, C.; Yi, Z.; Zhou, L.; Sun, J.; Zhang, K.; Zhou, Y. *Nanotechnology* **2007**, *18*, 135607−135612.

[20] Cushing, B. L.; Kang, S.-H.; Goodenough, J. B. *Int. J. Inorg. Mater*. **2001**, *3*, 875−879.

[21] Mikhailova, D.; Sarapulova, A.; Voss, A.; Thomas, A.; Oswald, S.; Gruner, W.; Trots, D. M.; Bramnik, N. N.; Ehrenberg, H. *Chem. Mater*. **2010**, *22*, 3165−3173.

[22] Sadakane, M.; Ohmura, S.; Kodato, K.; Fujisawa, T.; Kato, K.; Shimidzu, K.; Murayama, T.; Ueda, W. *Chem. Commun*. **2011**, *47*, 10812−10814.

[23] Sadakane, M.; Kodato, K.; Kuranishi, T.; Nodasaka, Y.; Sugawara, K.; Sakaguchi, N.; Nagai, T.; Matsui, Y.; Ueda, W. *Angew. Chem., Int. Ed*. **2008**, *47*, 2493−2496.

[24] Holmberg, J.; Grasseli, R. K.; Andersson, A. *Appl. Catal. A* **2004**, *270*, 121−134.

[25] Vitry, A.; Morikawa, Y.; Dubois, J. L.; Ueda, W. *Appl. Catal. A* **2003**, *251*, 411−424.

[26] Watanabe, N.; Ueda, W. *Ind. Eng. Chem. Res*. **2006**, *45*, 607−614.

[27] Pyrz, W. D.; Blom, D. A.; Shiju, N. R.; Guliants, V. V.; Vogt, T.; Buttrey, D. J. *J. Phys. Chem. C* **2008**, *112*, 10043−10049.

[28] Murayama, H.; Vitry, D.; Ueda, W.; Fuchs, G.; Anne, M.; Dubois, J. L. *Appl. Catal. A* **2007**, *318*, 137−142.

[29] Li, X.; Buttrey, D. J.; Blom, D. A.; Vogt, T. *Top. Catal*. **2011**, *54*, 614−626.

[30] Sadakane, M.; Watanabe, N.; Katou, T.; Nodasaka, Y.; Ueda, W. *Angew. Chem., Int. Ed.* **2007**, *46*, 1493−1496.

[31] Sathiya, M.; Ramesha, K.; Rousse, G.; Foix, D.; Gonbeau, D.; Prakash, A. S.; Doublet, M. L.; Hemalatha, K.; Tarascon, J.-M. *Chem. Mater*. **2013**, *25*, 1121−1131.

[32] Férey, G.; Millange, F.; Morcrette, M.; Serre, C.; Doublet, M.-L.; Grenèche, J.-M.; Tarascon, J.-M. *Angew. Chem., Int. Ed*. **2007**, *46*, 3259−3263.

[33] Ellis, B. L.; Michael Makahnouk, W. R.; Rowan-Weetaluktuk, W. N.; Ryan, D. H.; Nazar, L. F. *Chem. Mater*. **2010**, *22*, 1059−1070.

[34] Saravanan, K.; Ananthanarayanan, K.; Balaya, P. *Energy Environ. Sci*. **2010**, *3*, 939−948.

[35] Dickens, P. G.; French, S. J.; Hight, A. T.; Pye, M. F. *Mater. Res. Bull*. **1979**, *14*, 1295−1299.

[36] Murphy, D. W.; Cros, C.; Di Salvo, F. J.; Waszczak, J. V. *Inorg. Chem*. **1977**, *16*, 3027−3031.

Chapter 6

Rechargeable Magnesium Batteries Based on a Microporous Molydenum-Vanadium Oxide Electrode

6.1 Introduction

For the past two decades, the Li-ion rechargeable battery has contributed to the commercial success of portable electronic devices, and is considered to be one of the most successful achievements of advanced electrochemical power sources. The implementation of Li-ion batteries in higher-volume applications, such as large-scale energy storage units and sustainable vehicles, namely, hybrid electric vehicles (HEVs), plug-in hybrid electric vehicles (PHEVs), and ultimately full electric vehicles (EVs), however, is still limited by their high prices, resource scarcity, safety issues, and energy density limits.[1–5] An alternate solution to achieve the energy density requirements of electric vehicles is to use other systems that are based on more abundant elements than lithium. Magnesium batteries have been suggested as a promising candidate for next generation battery systems.[6,7] Magnesium, as a divalent metal, is expected to possess a high volumetric capacity of 3833 mAh/cm^3 (2046 mAh/cm^3 for Li) with a low reduction potential (–2.356 V vs standard hydrogen electrode, the lowest reduction potential after Li, –3.04 V), and the abundance of Mg resources (the fifth most abundant element in the earth's crust, 24 times cheaper than Li).[8–10] Magnesium metal anodes also offer superior safety compared to Li when exposed to air, and are not plagued by dendrite formation.[10–12]

Despite the advantages of magnesium over lithium as an anode material, the development of magnesium rechargeable batteries has been hampered by a variety of intrinsic problems related to the use of magnesium metal anodes and magnesium-ion intercalation cathodes.[13,14] One of the significant problems is the passivation of magnesium metal in most conventional non-aqueous polar organic solvents commonly used as electrolytes.[15,16] In contrast to Li electrodes where the surface films are Li-ion conductors, when surface films composed of ionic compounds are formed on Mg electrodes as a result of reduction reactions, they are electronic and ionic insulating, and do not allow Mg-ion migration through them. Thus, reversible Mg metal anodes only exist in passivation-free situations.[17–19] The first electrolytes which allowed Mg electrodes to behave reversibly were, for example, Grignard reagents in ethers, and magnesium organohaloaluminates with a formula of $Mg(AlCl_2BuEt)_2$ in THF. The electrochemical stability window of the first generation of electrolyte solutions was between 1.5 and 2.4 V, which limited the possible use of cathode materials with a higher redox potential.[20,21] However, the first successful prototype magnesium rechargeable batteries were developed in 2000, based on magnesium metal anodes and Mo_6S_8 (Chevrel phase) cathodes with the electrolyte $Mg(AlCl_2BuEt)_2$/THF ($Mg_xMo_6S_8$, $0 < x < 2$ with reversible specific capacity of ~80 mAh/g at 0.3 mA/cm^2).[22] Since then, some other complex solutions which allow passivation-free reversible Mg electrodes have been reported as electrolytes with improved electrochemical stability, such as the all-phenyl-complex (APC) based electrolyte, hexamethyldisilazide magnesium chloride (HMDSMgCl), and magnesium borohydride ($Mg(BH_4)_2$).[6,10,20,23–30]

Despite the increasing number of electrolytes for magnesium batteries reported, many of these complex solutions have limited anodic stability and poor compatibility with potential cathode materials based on transition metal oxides. Moreover, in most of the transition metal oxides and sulfides which can serve as excellent Li-ion insertion electrodes, Mg-ion intercalation is very slow or even impossible, even though these cations have similar ionic radii (0.76 Å for Li^+ and 0.72 Å for Mg^{2+}).[6,8] The reason for the slow kinetics of Mg-ion insertion into inorganic hosts is the divalent character. The sluggish solid state diffusion of the divalent cations is generally believed to arise not only from the strong Mg interactions with the anions and the cations of the hosts or the polarization effect of Mg^{2+} cations with a high charge/radius ratio, but also from the complexity in the redistribution of the divalent cation charge within the local crystal structure of the inorganic materials to maintain electroneutrality.[6,16,31]

In addition to the Chevrel phase, Mo_6S_8, used in the prototype magnesium rechargeable batteries by Aurbach et al.,[22] several types of Chevrel phase ($Mg_xMo_6T_8$, T = S, Se) cathodes have been thoroughly explored for rechargeable Mg batteries.[16,21,32–36] Other potential cathode materials are also being intensively studied,[16,37–43] including metal chalcogenides[44–49] and magnesium metal silicates.[50–55] Furthermore, alternative anode materials besides magnesium metal for Mg batteries have been reported,[56–61] and novel concepts have been developed for advanced rechargeable magnesium batteries.[7,62–66]

Among a wide range of compounds which have been examined as cathode materials for magnesium batteries, transition metal oxides have shown promising electrochemical properties, as they may possess the structural flexibility needed to accommodate the expected structural deformations upon insertion of divalent cations, such as Mg^{2+}.[13,14,67–71] Specifically, oxides, such as V_2O_5 and MoO_3 undergo intercalation of cations into their crystal lattice, including Li^+ and Mg^{2+} ions.[8,13,71–73] V_2O_5 has been studied very intensively as a cathode material for rechargeable Li batteries with high voltage and capacity, and is able to insert Mg ions reversibly.[13] However, V_2O_5 has poor capacity and slow rates of Mg-ion insertion, which could be explained by strong Coulombic interactions of the divalent cations within the host lattice.[8]

One of the approaches to mitigate these problems is to utilize appropriate complexing ligands bonded to the divalent Mg ions to help shield the charge of the cations within the intercalation compound.[10,16] It was found that the presence of a trace amount of water can strongly hydrate Mg ions and increase the rate and capacity of Mg-ion insertion into V_2O_5 electrodes.[16,70,74–79] Nonetheless, this approach is not compatible with magnesium anodes and may lead to excessive structural deformation of the host. Another method to mitigate slow solid state diffusion of Mg^{2+} ions is to decrease the length of diffusion pathway by nanosizing the cathode material.[6,10,16,80]

Another drawback of V_2O_5 is its low electronic conductivity.[71–73] One way to avoid this problem is to use vanadium oxides doped with another transition metal. Molybdenum-doped vanadium oxides have enhanced electronic conductivity due to an increased V^{4+} concentration produced by substitution of Mo^{6+} for V^{5+}.[81–84] In the context

of the oxides, V_2O_5 and MoO_3, which can reversibly undergo intercalation of Mg^{2+} ions into their crystal lattice,[8] we have investigated a molybdenum-vanadium-based molecular sieve $Mo_{2.5+y}VO_{9+\delta}$ as cathode material for rechargeable Mg batteries.[85,86] The large open channels along the crystallographic *c*-axis, which can accommodate small guest molecules, such as Li^+ and Mg^{2+} ions, and the redox properties of $Mo_{2.5+y}VO_{9+\delta}$ suggest the potential of this material as a rechargeable intercalation electrode in Mg-based batteries.[87–93] Recently, we have reported the use of $Mo_{2.5+y}VO_{9+\delta}$ as cathode material in lithium cells with an outstanding reversible capacity exceeding 300 mAh/g.[94] When the cells are discharged between 3.9 and 1.5 V vs Li/Li^+, up to 6 Li^+ ions per formula unit are electrochemically inserted into the framework. Upon recharge, all of the Li^+ ions can be extracted with minimal structural rearrangement.

6.2 Experimental Section

6.2.1 Synthesis

$Mo_{2.5+y}VO_{9+\delta}$ was synthesized under hydrothermal conditions as previously reported.[94] To briefly describe the procedure, a reaction mixture of $(NH_4)_6Mo_7O_{24}\cdot 4H_2O$ (0.66 g, 0.54 mmol, dissolved in 9 mL H_2O) and $VOSO_4\cdot nH_2O$ (0.25 g, 0.94 mmol, dissolved in 9 mL H_2O) was stirred at room temperature for 10 min. The resulting solution was then transferred to a 23 mL Teflon-lined Parr stainless steel autoclave, purged with nitrogen for 1 min to replace the air, and then heated at 190 °C for 48 h. A dark gray solid was obtained from the reaction by filtration, washed with water, and dried at 80 °C. The crude product (0.35 g) was then stirred in 8.75 mL of 0.4 M oxalic acid

aqueous solution at 60 °C for 30 min to remove an amorphous byproduct, washed with water, and dried at 80 °C, before being calcined at 400 °C for 2 h in air to remove any water and NH_4^+ from the micropores.

$Mg_xMo_{2.5+y}VO_{9+\delta}$ (x = 0.1 to x = 2) was prepared by two different methods: (1) chemical intercalation at room temperature under an argon atmosphere of $Mo_{2.5+y}VO_{9+\delta}$ using di-*n*-butylmagnesium, $(C_4H_9)_2Mg$, in heptane as the reducing agent,[14,95,96] and (2) in electrochemical cells.

6.2.2 Chemical Intercalation

To prepare $Mg_xMo_{2.5+y}VO_{9+\delta}$, an appropriate amount of 1 M di-*n*-butylmagnesium ($(C_4H_9)_2Mg$) in heptane was added to powdered $Mo_{2.5+y}VO_{9+\delta}$ inside an argon-filled glovebox. The mixture was stirred at ambient temperature for 3−10 d depending on the degree of the magnesium insertion; longer times were used for larger values of x in $Mg_xMo_{2.5+y}VO_{9+\delta}$. The product was filtered, washed with dry heptane to remove traces of unreacted reagent and byproducts, and dried under vacuum. The filtrate and washings were combined and mixed with 25 mL of water. The extent of magnesium intercalation was quantitatively determined by titrating the liquid mixture with a standardized aqueous HCl solution. The solid was then equilibrated to ensure product homogeneity by stirring in a non-aqueous electrolyte solution containing Mg^{2+} ions, 0.2 M magnesium(II) bis(trifluoromethanesulfonyl)imide, $Mg[N(SO_2CF_3)_2]_2$, ($Mg(TFSI)_2$) in tetrahydrofuran (THF) solution[8,24,97,98] for 48 h inside an argon-filled glovebox.

6.2.3 Electrochemical Studies

The electrochemical properties of $Mo_{2.5+y}VO_{9+\delta}$ were obtained using a multichannel potentiostat-galvanostat MacPile system (Biologic SA, Claix, France) at different discharge-charge current densities between ~2.1 and 1.0 V vs Mg/Mg^{2+} in 2032 coin cells.

Coin Cells. In a standard coin cell, the positive electrode consisted of 75 wt% $Mo_{2.5+y}VO_{9+\delta}$, 15 wt% acetylene carbon black, and 10 wt% polyvinylidene fluoride (PVdF) binder. The mixture was pre-mixed in an agate mortar, and then ground using a high-energy ball mill (SPEX mill 8000M) in an agate vial set for 10 min, followed by hot-pressing onto a stainless steel disc (16 mm in diameter with 1−2 mg of active electrode material). The electrodes were dried in vacuum at 90 °C for 12 h, before being transferred to an argon-filled glovebox in which the cells were assembled. The cells had a magnesium metal disc as the negative electrode which was thoroughly scraped using the sharp edge of microscope glass slides, and then rinsed with anhydrous THF (which had been distilled with benzophenone containing sodium chips under argon and dried over molecular sieves) to clean its surface from any passivation layer (oxide species, such as MgO and $Mg(OH)_2$).[17,24] In order to make sure that the newly exposed magnesium surface would be totally free of contaminants arising from the glovebox (any possible oxidation of the Mg surface), the Mg disc was scraped once again while immersed in anhydrous THF in a Petri dish the moment that each cell was assembled. The negative electrode was separated from the positive electrode by a Whatman borosilicate glass fiber sheet (separator) saturated with 0.2 M $Mg(TFSI)_2$ in THF solution, which was used as the

electrolyte. Electrochemical testing conditions are specified in the Results and Discussion section.

6.2.4 Materials Characterization

Powder X-ray diffraction (PXRD) patterns were collected at room temperature on a Phillips PANalytical X'Pert PRO diffractometer with Cu Kα radiation (λ = 1.54046 Å) for determination of the unit cell parameters. Phase analyses of $Mg_xMo_{2.5+y}VO_{9+\delta}$ were performed in a sealed sample holder to avoid any contact with air. Extraction of the peak positions, pattern indexing, and profile refinements were carried out using GSAS.

6.3 Results and Discussion

6.3.1 Description of $Mo_{2.5+y}VO_{9+\delta}$

The detailed discussion of the synthesis has been given previously.[94] The framework of $Mo_{2.5+y}VO_{9+\delta}$ can be described as a layered structure where each layer is made from corner-sharing MO_6 octahedra and pentagonal [(Mo)Mo_5O_{27}] units, which are assembled from a MoO_7 pentagonal bipyramid and five edge-sharing MoO_6 octahedra. The layers are joined together by corner-sharing to form the three-dimensional microporous framework with three-, six-, and seven-membered ring tunnels with orthorhombic symmetry, *Pba*2 (a = 21.0505(3) Å, b = 26.3766(5) Å, and c = 4.0144(1) Å). The size of the empty channels available for insertion of guest species from the space-filling model is approximately 3 Å in diameter for six-membered ring channels,

and 5 Å for seven-membered ring channels (Figure 6.1). According to the previous analyses, the amount of oxygen, *z*, in $Mo_{2.5+y}VO_z$ was determined to be 9.93 and the Mo:V ratio of this compound was 2.48:1 per formula unit.[94] $Mo_{2.5+y}VO_{9+\delta}$ crystals are rod-like with the size of up to 200 nm in diameter and tens of micrometers in length. The large open channels that can accommodate diffusion of small guest species, such as Li^+ and Mg^{2+} ions, are along the crystallographic *c* direction, which is also along the length of the crystal.[94]

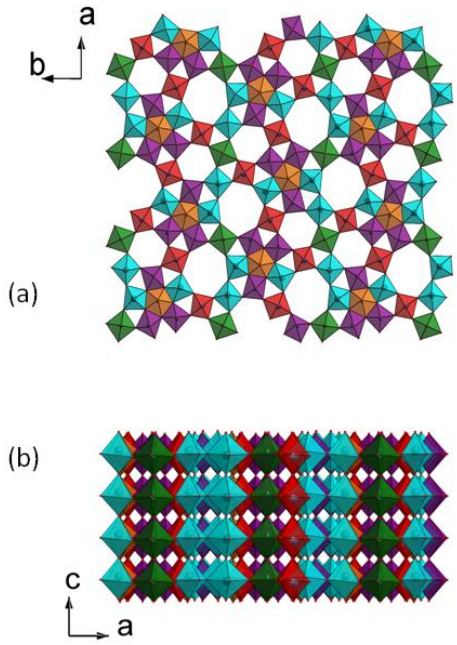

Figure 6.1 (a) Structure of $Mo_{2.5+y}VO_{9+\delta}$ viewed along the *c*-axis: MO_6 octahedra and MO_7 pentagonal bipyramids (M = Mo and V cations predicted theoretically with different oxidation states and occupancies: green, Mo^{5+}/V^{4+}; red, Mo^{6+}/V^{5+}; blue, Mo^{6+}/Mo^{5+}; orange, Mo^{5+}; and purple, Mo^{6+}). (b) Projection of the framework along the *b*-axis showing layer stacking.

6.3.2 Electrochemical Behavior of $Mo_{2.5+y}VO_{9+\delta}$

In order to investigate the electrochemical properties, $Mo_{2.5+y}VO_{9+\delta}$ or $Mo_{2.48}VO_{9.93}$ was used as an intercalation electrode material.

For galvanostatic cycling at room temperature, electrodes composed of $Mo_{2.48}VO_{9.93}$ were discharged and charged in a magnesium cell with metallic Mg as the negative electrode, at a rate of 1 Mg in 15 h or *C*/15 (20 mA/g) with an open circuit voltage (OCV) of ~2.1 V.[54,99] The first electrochemical cycle obtained from a coin cell is shown in Figure 6.2. The profile shows that 1 Mg^{2+} ion per formula unit can be reversibly inserted into and removed from $Mo_{2.48}VO_{9.93}$ between 2.0 and 1.15 V, with a pronounced plateau at 1.2 V; the total capacity corresponds to 114 mAh/g. Due to the fact that molybdenum and vanadium ions ($Mo^{5+/6+}$ or $V^{4+/5+}$) in $Mo_{2.5+y}VO_{9+\delta}$ have mixed occupation of crystallographic sites and the local oxygen environments are uncertain, it is difficult to indicate the redox couples and the processes taking place during the first discharge. Presumably, all of the metal ions (Mo^{5+}, Mo^{6+}, V^{4+}, and V^{5+}) actively participate in the electrochemical magnesium intercalation, where the metal ions are reduced as Mg^{2+} is inserted into the structure and oxidized during deintercalation. The second discharge is quite different from the first, having a significantly less IR drop and a smooth curve without any distinct plateaus (red curve in Figure 6.2). This profile behavior is similar to those previously reported for mixed molybdenum-vanadium oxides cycled in lithium cells, where plateaus were observed only upon reduction during the first discharge.

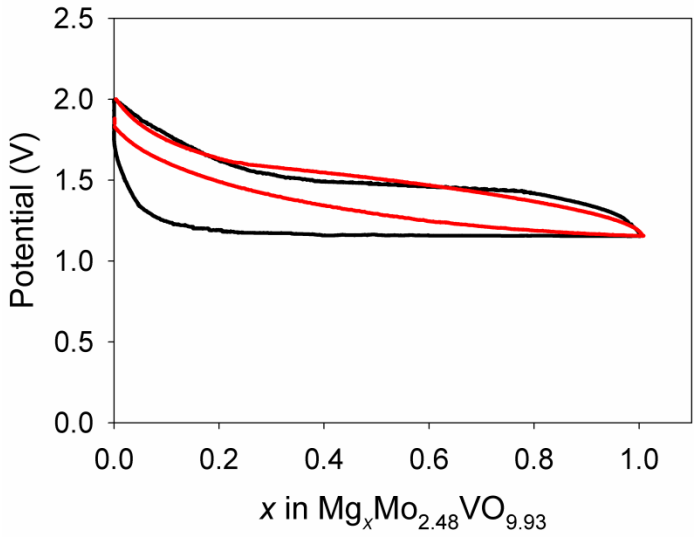

Figure 6.2 Electrochemical discharge-charge profile of a Mg/$Mo_{2.48}VO_{9.93}$ coin cell between 2.0 and 1.15 V at a rate of *C*/15 (20 mA/g): black, 1st cycle; red, 2nd cycle.

The discharge voltage profiles of $Mo_{2.48}VO_{9.93}$ at various current densities ranging from 20 mA/g to 60 mA/g are shown in Figure 6.3. As the discharge rate increases, the discharge potential decreases due to kinetic effects. With a cutoff voltage of 1.0 V, the cells gave a discharge capacity ranging from 120 mAh/g (at 60 mA/g) up to 240 mAh/g (at 20 mA/g corresponding to ~2.1 Mg per formula unit), depending on the cycling rate. It is noteworthy that at a high discharge rate of 60 mA/g, a discharge capacity of 120 mAh/g can be obtained. The good rate capability and capacity of the electrodes can be attributed to the open three-dimensional porous framework structure of $Mo_{2.48}VO_{9.93}$ with large empty tunnels of up to 5 Å in diameter. As a result, Mg^{2+} with an effective ionic radius of 0.72 Å can rapidly diffuse into the channels, and the framework can accommodate a large amount of Mg^{2+}. Moreover, the small size of ground $Mo_{2.48}VO_{9.93}$

rod-like crystals provides large contact area between the active material and the magnesium electrolyte, resulting in short diffusion paths for Mg^{2+} ions thereby enhancing the rate capability.

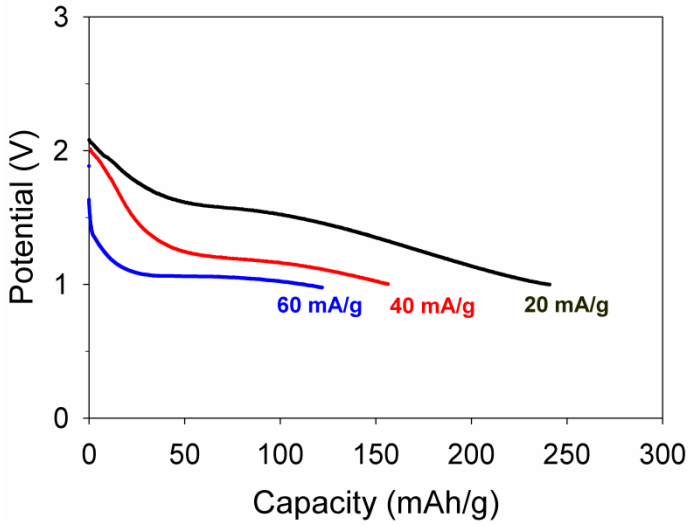

Figure 6.3 Rate performance of $Mg/Mo_{2.48}VO_{9.93}$ cells at various discharge rates: 60 mA/g, 40 mA/g, and 20 mA/g.

Capacity retention data for galvanostatic cycling of $Mg/Mo_{2.48}VO_{9.93}$ cells ($Mg_xMo_{2.48}VO_{9.93}$, $x = 1$) at various current densities ranging from 20 mA/g to 60 mA/g, are shown in Figure 6.4. At 20 mA/g, the reversible specific capacity vs cycle number shows a slight capacity drop during initial cell cycles followed by stable capacity retention of ~110 mAh/g. The irreversible capacity loss during the first few cycles may correspond to some of Mg^{2+} ions becoming trapped in the small three-membered ring channels of the framework. Once the system has equilibrated, the cell can cycle

reversibly without further capacity loss. It is worth noting that when the Mg cells are cycled at higher rates (40 mA/g and 60 mA/g) with a cutoff voltage at 1.0 V, there is a significant capacity decline right after 10 cycles. The irreversible capacity drop is probably due to kinetic effects which could be attributed to ionic (slow solid state diffusion of Mg^{2+} ions in the host lattice) and electronic transport limitations at high current densities.

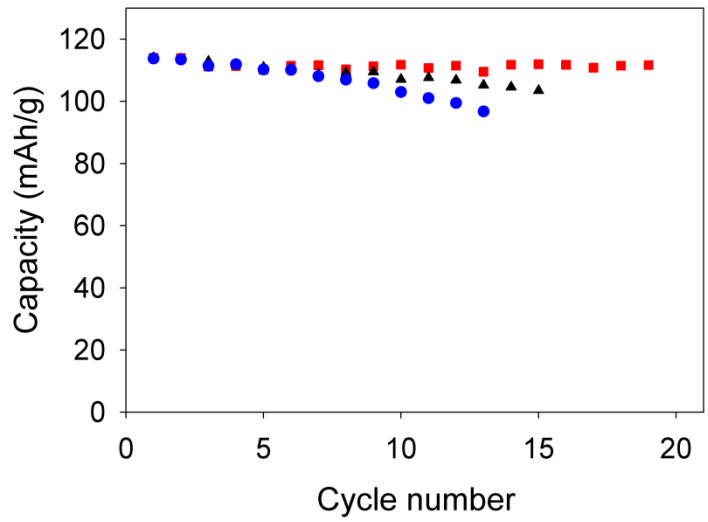

Figure 6.4 Capacity retention data for galvanostatic cycling of $Mg/Mo_{2.48}VO_{9.93}$ cells ($Mg_xMo_{2.48}VO_{9.93}$, x = 1) at various current densities: red squares, 20 mA/g; black triangles, 40 mA/g; blue circles, 60 mA/g.

6.3.3 Chemical Redox Intercalation of $Mo_{2.48}VO_{9.93}$ using a Reducing Agent

To examine the structural evolution of $Mo_{2.48}VO_{9.93}$ upon magnesium intercalation, X-ray diffraction data were obtained for chemically reduced $Mo_{2.48}VO_{9.93}$ ($Mg_xMo_{2.48}VO_{9.93}$, x = 0.1 to x = 2). $(C_4H_9)_2Mg$ can be used as a reducing agent to prepare $Mg_xMo_{2.48}VO_{9.93}$ from $Mo_{2.48}VO_{9.93}$ according to the reaction: $Mo_{2.48}VO_{9.93} + x(C_4H_9)_2Mg \rightarrow Mg_xMo_{2.48}VO_{9.93} + xC_8H_{18}$.[14] The x value was indicated by titration of the filtrate which had been hydrolyzed, with a standardized aqueous HCl solution to determine the amount of $(C_4H_9)_2Mg$ left over from the reaction. Because heptane was used as the reaction medium during the chemical insertion, the product $Mg_xMo_{2.48}VO_{9.93}$ was then equilibrated in the electrolyte solution containing Mg^{2+} ions (0.2 M $Mg(TFSI)_2$ in THF) by stirring for 48 h at room temperature under inert atmosphere, to ensure compositional homogeneity among the particles. PXRD measurements were performed on $Mg_xMo_{2.48}VO_{9.93}$ using a sealed sample holder (under Kapton) loaded in the glovebox. The X-ray diffraction patterns of $0.1 \leq x \leq 2$ in $Mg_xMo_{2.48}VO_{9.93}$ (x values determined by the titration) are shown in Figure 6.5. The unit cell parameters of $Mg_xMo_{2.48}VO_{9.93}$ determined by profile fitting using GSAS are summarized as a function of the degree of Mg insertion in Figure 6.6. The Le Bail refinement of the pristine $Mo_{2.48}VO_{9.93}$ (that was stirred in heptane and dried in argon) is shown in Figure 6.7 for comparison with $Mg_xMo_{2.48}VO_{9.93}$ (x = 1.5).

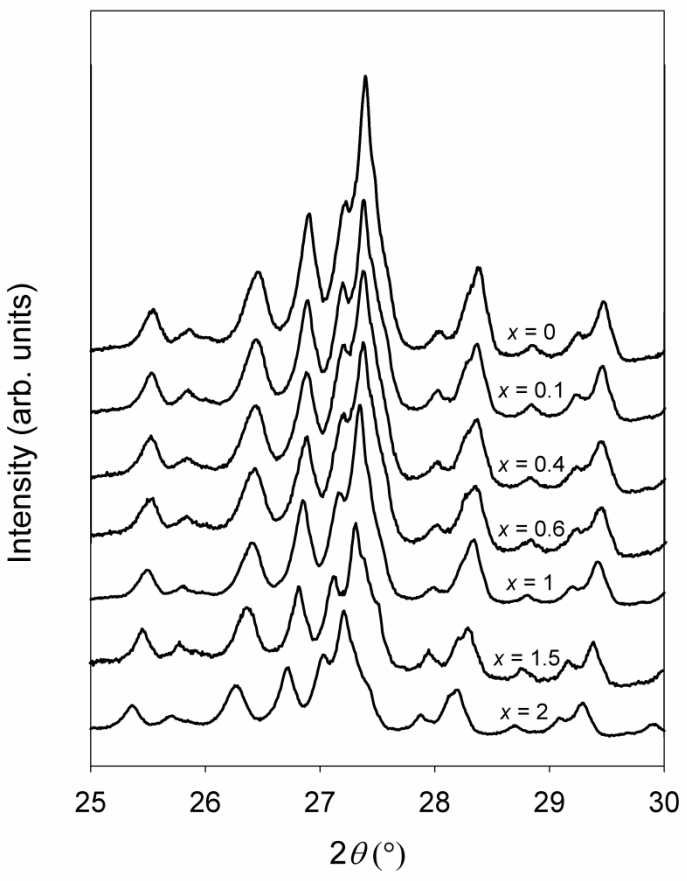

Figure 6.5 PXRD patterns of chemically prepared $Mg_xMo_{2.48}VO_{9.93}$, illustrating the changes occurring in the range of $x = 0 \rightarrow 2$, selected 2θ range (25−30°).

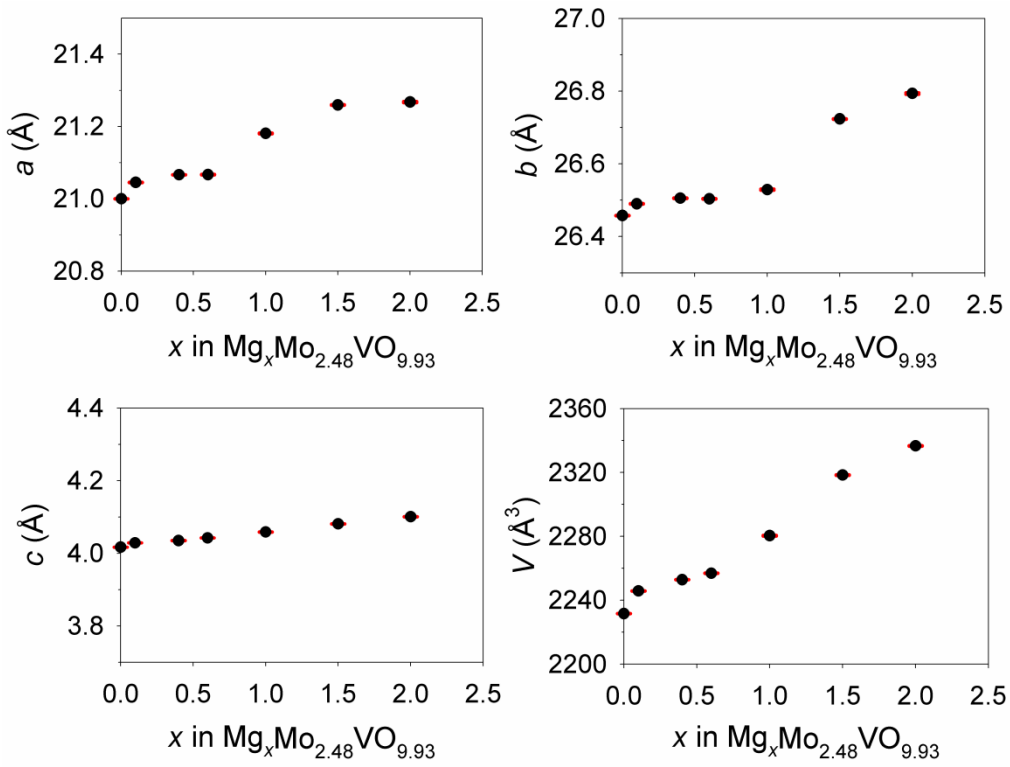

Figure 6.6 Lattice parameters and unit cell volume of chemically prepared $Mg_xMo_{2.48}VO_{9.93}$ refined by profile fitting (error bars in red).

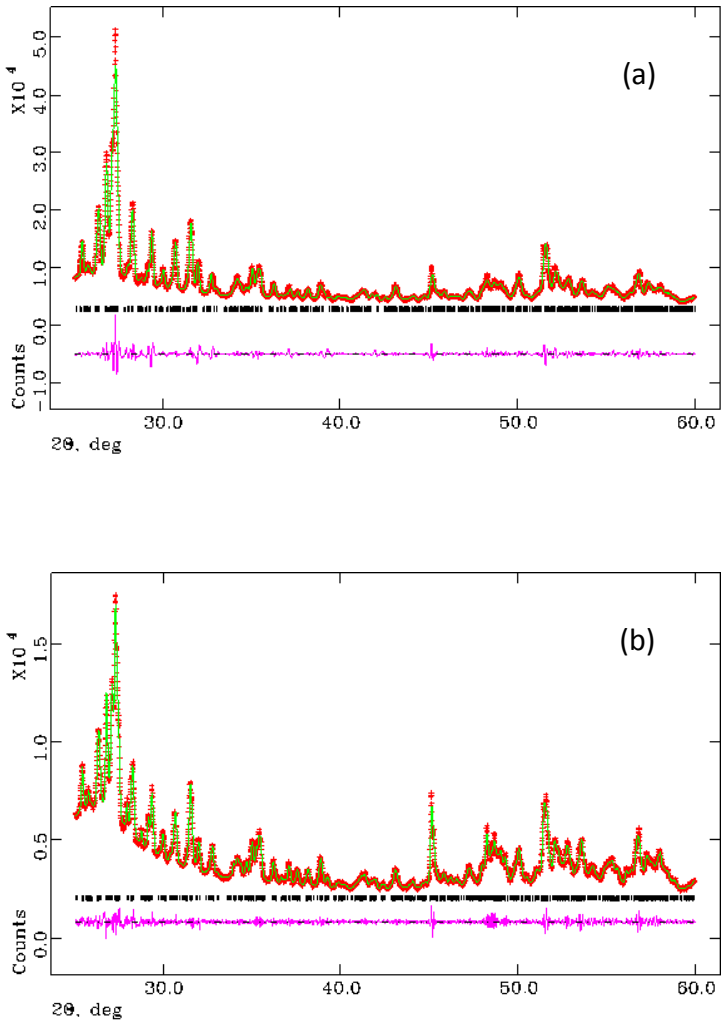

Figure 6.7 (a) Le Bail refinement of pristine $Mo_{2.48}VO_{9.93}$. (b) The refinement of $Mg_{1.5}Mo_{2.48}VO_{9.93}$ (prepared by the reduction of $Mo_{2.48}VO_{9.93}$ using $(C_4H_9)_2Mg$) in *Pba*2, wR_p = 3.65%: lattice parameters a = 21.2595(8) Å, b = 26.7235(8) Å, and c = 4.0807(2) Å. (The measured data are shown in orange, the calculated data are shown in green, and the difference is shown in pink. Bragg reflections are shown by vertical tick marks.)

The lattice parameters of chemically prepared $Mg_xMo_{2.48}VO_{9.93}$, $0 \leq x \leq 2$, compounds are consistent with the voltage profiles shown in Figure 6.2. Starting from the pristine $Mo_{2.48}VO_{9.93}$, the electrochemical insertion of Mg^{2+} ions into crystalline $Mo_{2.48}VO_{9.93}$ takes place through a two-phase equilibrium identified by the voltage plateau at 1.2 V on the discharge curve. From $x = 0$ to ca. 0.2, a gradual decrease of cell potential is observed which corresponds to a single-phase solid solution, as confirmed by the PXRD patterns; the unit cell volume slightly increases in this region. For $x = 0.2$ to ca. 1, the phase $Mg_xMo_{2.48}VO_{9.93}$ ($x = 0{-}0.2$) is in equilibrium with the second solid solution phase that is formed when $1 \leq x \leq 2$ as shown in Figure 6.3 (the voltage profile at 20 mA/g). A distinct change in unit cell parameters is observed at $x = 1$. The profile refinements indicate that $Mg_xMo_{2.48}VO_{9.93}$ ($1 \leq x \leq 2$) has a similar structure to the pristine compound, and the orthorhombic *Pba*2 structure is maintained throughout the intercalation; the *a* and *b* lattice parameters significantly increase while the *c* lattice parameters only increase very slightly for $1 \leq x \leq 2$ (Figure 6.6). It is worth noting that the second solid solution phase ($Mg_xMo_{2.48}VO_{9.93}$, $1 \leq x \leq 2$) as evident from the distinct change in the unit cell parameters observed at $x \geq 1$, is in agreement with the solid solution phase formed during lithium intercalation of $Mo_{2.48}VO_{9.93}$, which is in the range of $2 \leq x \leq 4$ in $Li_xMo_{2.48}VO_{9.93}$.[94] However, no obvious phase transition is observed in the X-ray diffraction data for magnesium insertion, unlike the case of the lithiated compound $Li_xMo_{2.48}VO_{9.93}$, where an apparent transition can be seen for $2 \leq x \leq 4$.

The lattice parameters of $Mg_xMo_{2.48}VO_{9.93}$ (x = 2) show that the unit cell volume of $Mg_2Mo_{2.48}VO_{9.93}$ is only ~5% larger than that of the parent compound due to the guest insertion. Overall, there is a clear trend in the lattice parameters as x in $Mg_xMo_{2.48}VO_{9.93}$ increases: the a and b lattice parameters significantly increase, while the c lattice parameters which correspond to the layer stacking direction remain relatively constant. During charge, deintercalation of magnesium occurs, and the phase transition results in solid-solution-like electrochemical behavior with sloping voltage profile over the range of $x = 1 \rightarrow x = 0$ (Figure 6.2). As indicated by the electrochemical profiles, some structural reorganization does occur during the intercalation and deintercalation, which is also confirmed by PXRD data, but nevertheless magnesium insertion into $Mo_{2.48}VO_{9.93}$ is reversible.

The ability of $Mo_{2.5+y}VO_{9+\delta}$ to act as a Mg insertion cathode material may be due to: (1) the unique nature of $Mo_{2.5+y}VO_{9+\delta}$ framework where molybdenum and vanadium ions ($Mo^{5+/6+}$ or $V^{4+/5+}$) have mixed occupation of crystallographic sites and variation of local oxygen environments, leading to excellent redox activities as evidenced in the outstanding catalytic properties previously reported.[85,86] This feature presumably helps with the redistribution of the divalent cation charge and maintenance of local electroneutrality by the electron delocalized $Mo_{2.5+y}VO_{9+\delta}$ framework.; (2) the large open tunnels along the crystallographic c-axis of the $Mo_{2.5+y}VO_{9+\delta}$ structure which readily serve as solid state diffusion channels for the strongly polarized Mg^{2+} cations, and account for the magnesium storage capacity with small unit cell volume expansion, reducing lattice strain and helping with intercalation reversibility; (3) the good electronic

conductivity of $Mo_{2.5+y}VO_{9+\delta}$. As reported previously, the compound could be used as an electrode material in lithium cells without conducting additives, and the same specific capacity as those with carbon additives still could be delivered.[94]

6.4 Conclusions

The mixed molybdenum-vanadium oxide, $Mo_{2.5+y}VO_{9+\delta}$, behaves as a rechargeable intercalation electrode material not only in Li-based batteries (previously reported) but also in magnesium rechargeable batteries. $Mo_{2.48}VO_{9.93}$ can be reversibly cycled in an electrochemical cell with magnesium as the counter electrode at rates up to 60 mA/g with good specific capacity (x = 1 in $Mg_xMo_{2.48}VO_{9.93}$). The structural changes associated with the electrochemical magnesiation have been characterized through ex-situ X-ray diffraction of phases prepared by a chemical route using $(C_4H_9)_2Mg$. At x = 2 in $Mg_xMo_{2.48}VO_{9.93}$, the unit cell volume is only 5% larger than that of the parent compound. The oxide $Mo_{2.5+y}VO_{9+\delta}$ can be used as an electrode material to electrochemically intercalate Mg^{2+} ions reversibly in magnesium cells, despite the fact that oxides have higher ionicity compared to sulfides (such as the Chevrel phases that can provide fast and reversible Mg insertion), thus leading to stronger interactions between the Mg^{2+} guest and ions of the host, and lowering the cation mobility. By further understanding of the mechanism of the reactions involved, the electrochemical properties of this mixed molybdenum-vanadium oxide may be further improved, and this may pave the way for other oxide-based materials for the use in Mg rechargeable batteries.

6.5 References

[1] Armand, M.; Tarascon, J.-M. *Nature* **2008**, *451*, 652−657.

[2] Dunn, B.; Kamath, H.; Tarascon, J.-M. *Science* **2011**, *334*, 928−935.

[3] Tarascon, J.-M.; Armand, M. *Nature* **2001**, *414*, 359−367.

[4] Liu, C.; Li, F.; Ma, L.-P.; Cheng, H.-M. *Adv. Mater*. **2010**, *22*, E28−E62.

[5] Marom, R.; Amalraj, S. F.; Leifer, N.; Jacob, D.; Aurbach, D. *J. Mater. Chem*. **2011**, *21*, 9938−9954.

[6] Shterenberg, I.; Salama, M.; Gofer, Y.; Levi, E.; Aurbach, D. *MRS Bulletin* **2014**, *39*, 453−460.

[7] Ling, C.; Banerjee, D.; Song, W.; Zhang, M.; Matsui, M. *J. Mater. Chem*. **2012**, *22*, 13517−13523.

[8] Gershinsky, G.; Yoo, H. D.; Gofer, Y.; Aurbach, D. *Langmuir* **2013**, *29*, 10964−10972.

[9] Aurbach, D.; Weissman, I.; Gofer, Y.; Levi, E. *Chem. Rec*. **2003**, *3*, 61−73.

[10] Yoo, H. D.; Shterenberg, I.; Gofer, Y.; Gershinsky, G.; Pour, N.; Aurbach, D. *Energy Environ. Sci.* **2013**, *6*, 2265−2279.

[11] Cheng, Y.; Liu, T.; Shao, Y.; Engelhard, M. H.; Liu, J.; Li, G. *J. Mater. Chem. A* **2014**, *2*, 2473−2477.

[12] Besenhard, J. O.; Winter, M. *ChemPhysChem* **2002**, *3*, 155−159.

[13] Novák, P.; Imhof, R.; Hass, O. *Electrochim. Acta* **1999**, *45*, 351−367.

[14] Gregory, T. D.; Hoffman, R. J.; Winterton, R. C. *J. Electrochem. Soc.* **1990**, *137*, 775−780.

[15] Lu, Z.; Schechter, A.; Moshkovich, M.; Aurbach, D. *J. Electroanal. Chem*. **1999**, *466*, 203−217.

[16] Levi, E.; Gofer, Y.; Aurbach, D. *Chem*. *Mater.* **2010**, *22*, 860−868.

[17] Gofer, Y.; Turgeman, R.; Cohen, H.; Aurbach, D. *Langmuir* **2003**, *19*, 2344−2348.

[18] Aurbach, D.; Schechter, A.; Moshkovich, M.; Cohen, Y. *J. Electrochem. Soc.* **2001**, *148*, A1004−A1014.

[19] Levi, E.; Lancry, E.; Gofer, Y.; Aurbach, D. *J. Solid State Electrochem*. **2006**, *10*, 176−184.

[20] Muldoon, J.; Bucur, C. B.; Oliver, A. G.; Sugimoto, T.; Matsui, M.; Kim, H. S.; Allred, G. D.; Zajicek, J.; Kotani, Y. *Energy Environ. Sci.* **2012**, *5*, 5941−5950.

[21] Aurbach, D.; Suresh, G. S.; Levi, E.; Mitelman, A.; Mizrahi, O.; Chusid, O.; Brunelli, M. *Adv. Mater*. **2007**, *19*, 4260−4267.

[22] Aurbach, D.; Lu, Z.; Schechter, A.; Gofer, Y.; Gizbar, H.; Turgeman, R.; Cohen, Y.; Moshkovich, M.; Levi, E. *Nature* **2000**, *407*, 724−727.

[23] Mohtadi, R.; Matsui, M.; Arthur, T. S.; Hwang, S.-J. *Angew. Chem., Int. Ed*. **2012**, *51*, 9780−9783.

[24] Ha, S.-Y.; Lee, Y.-W.; Woo, S. W.; Koo, B.; Kim, J.-S.; Cho, J.; Lee, K. T.; Choi, N.-S. *ACS Appl. Mater. Interfaces* **2014**, *6*, 4063−4073.

[25] Zhu, J.; Guo, Y.; Yang, J.; NuLi, Y.; Zhang, F.; Wang, J.; Hirano, S. *J. Power Sources* **2014**, *248*, 690−694.

[26] Higashi, S.; Miwa, K.; Aoki, M.; Takeshi, K. *Chem. Commun*. **2014**, *50*, 1320−1322.

[27] Liu, T.; Shao, Y.; Li, G.; Gu, M.; Hu, J.; Xu, S.; Nie, Z.; Chen, X.; Wang, C.; Liu, J. *J. Mater. Chem. A* **2014**, *2*, 3430−3438.

[28] Doe, R. E.; Han, R.; Hwang, J.; Gmitter, A. J.; Shterenberg, I.; Yoo, H. D.; Pour, N.; Aurbach, D. *Chem. Commun*. **2014**, *50*, 243−245.

[29] Aubrey, M. L.; Ameloot, R.; Wiers, B. M.; Long, J. R. *Energy Environ. Sci*. **2014**, *7*, 667−671.

[30] Liao, C.; Guo, B.; Jiang, D.; Custelcean, R.; Mahurin, S. M.; Sun, X.-G.; Dai, S. *J. Mater. Chem. A* **2014**, *2*, 581−584.

[31] Levi, E.; Levi, M. D.; Chasid, O.; Aurbach, D. *J. Electroceram*. **2009**, *22*, 13−19.

[32] Mitelman, A.; Levi, E.; Lancri, E.; Aurbach, D. *ECS Trans*. **2007**, *3*, 109−115.

[33] Gershinsky, G.; Haik, O.; Salitra, G.; Grinblat, J.; Levi, E.; Nessim, G. D.; Zinigrad, E.; Aurbach, D. *J. Solid State Chem*. **2012**, *188*, 50−58.

[34] Mitelman, A.; Levi, M. D.; Lancry, E.; Levi, E.; Aurbach, D. *Chem. Commun*. **2007**, 4212−4214.

[35] Suresh, G. S.; Levi, M. D.; Aurbach, D. *Electrochim. Acta* **2008**, *53*, 3889−3896.

[36] Levi, M. D.; Lancri, E.; Levi, E.; Gizbar, H.; Gofer, Y.; Aurbach, D. *Solid State Ionics* **2005**, *176*, 1695−1699.

[37] Ichitsubo, T.; Adachi, T.; Yagi, S.; Doi, T. *J. Mater. Chem*. **2011**, *21*, 11764−11772.

[38] Giraudet, J.; Claves, D.; Guérin, K.; Dubois, M.; Houdayer, A.; Masin, F.; Hamwi, A. *J. Power Sources* **2007**, *173*, 592−598.

[39] Ling, C.; Mizuno, F. *Chem. Mater*. **2013**, *25*, 3062−3071.

[40] Makino, K.; Katayama, Y.; Miura, T.; Kishi, T. *J. Power Sources* **2002**, *112*, 85−89.

[41] NuLi, Y.; Guo, Z.; Liu, H.; Yang, J. *Electrochem. Commun.* **2007**, *9*, 1913−1917.

[42] Amir, N.; Vestfrid, Y.; Chusid, O.; Gofer, Y.; Aurbach, D. *J. Power Sources* **2007**, *174*, 1234−1240.

[43] Huang, Z.-D.; Masese, T.; Orikasa, Y.; Mori, T.; Minato, T.; Tassel, C.; Kobayashi, Y.; Kageyama, H.; Uchimoto, Y. *J. Mater. Chem. A* **2014**, *2*, 11578−11582.

[44] Li, X.-L.; Li, Y.-D. *J. Phys. Chem. B* **2004**, *108*, 13893−13900.

[45] Liang, Y.; Feng, R.; Yang, S.; Ma, H.; Liang, J.; Chen, J. *Adv. Mater.* **2011**, *23*, 640−643.

[46] Liu, B.; Luo, T.; Mu, G.; Wang, X.; Chen, D.; Shen, G. *ACS Nano* **2013**, *7*, 8051−8058.

[47] Yang, S.; Li, D.; Zhang, T.; Tao, Z.; Chen, J. *J. Phys. Chem. C* **2012**, *116*, 1307−1312.

[48] Tao, Z.-L.; Xu, L.-N.; Gou, X.-L.; Chen, J.; Yuan, H.-T. *Chem. Commun.* **2004**, 2080−2081.

[49] Liu, Y.; Jiao, L.; Wu, Q.; Zhao, Y.; Cao, K.; Liu, H.; Wang, Y.; Yuan, H. *Nanoscale* **2013**, *5*, 9562−9567.

[50] NuLi, Y.; Yang, J.; Li, Y.; Wang, J. *Chem. Commun.* **2010**, *46*, 3794−3796.

[51] NuLi, Y.; Zheng, Y.; Wang, F.; Yang, J.; Minett, A. I.; Wang, J.; Chen, J. *Electrochem. Commun.* **2011**, *13*, 1143−1146.

[52] NuLi, Y.; Yang, J.; Wang, J.; Li, Y. *J. Phys. Chem. C* **2009**, *113*, 12594−12597.

[53] Li, Y.; NuLi, Y.; Yang, J.; Yilinuer, T.; Wang, J. *Chinese Sci. Bull.* **2011**, *56*, 386−390.

[54] NuLi, Y.; Zheng, Y.; Wang, Y.; Yang, J.; Wang, J. *J. Mater. Chem.* **2011**, *21*, 12437−12443.

[55] Zheng, Y.; NuLi, Y.; Chen, Q.; Wang, Y.; Yang, J.; Wang, J. *Electrochim. Acta* **2012**, *66*, 75−81.

[56] Singh, N.; Arthur, T. S.; Ling, C.; Matsui, M.; Mizuno, F. *Chem. Commun.* **2013**, *49*, 149−151.

[57] Wang, Z.; Su, Q.; Shi, J.; Deng, H.; Yin, G. Q.; Guan, J.; Wu, M. P.; Zhou, Y. L.; Lou, H. L.; Fu, Y. Q. *ACS Appl. Mater. Interfaces* **2014**, *6*, 6786−6789.

[58] Sivashanmugam, A.; Prem Kumar, T.; Renganathan, N. G.; Gopukumar, S. *J. Appl. Electrochem.* **2004**, *34*, 1135−1139.

[59] Malyi, O. I.; Tan, T. L.; Manzhos, S. *J. Power Sources* **2013**, *233*, 341−345.

[60] Shao, Y.; Gu, M.; Li, X.; Nie, Z.; Zuo, P.; Li, G.; Liu, T.; Xiao, J.; Cheng, Y.; Wang, C.; Zhang, J.-G.; Liu, J. *Nano Lett.* **2014**, *14*, 255−260.

[61] Arthur, T. S.; Singh, N.; Matsui, M. *Electrochem. Commun.* **2012**, *16*, 103−106.

[62] Perween, M.; Gupta, R.; Rebary, B.; Kulshrestha, V.; Srivastava, D. N. *Phys. Chem. Chem. Phys.* **2013**, *15*, 17758−17762.

[63] Vatsala Rani, J.; Bhavana Rushi, S.; Kanakaiah, V.; Palaniappan, S. *J. Electrochem. Soc.* **2011**, *158*, A1031−A1035.

[64] Kim, H. S.; Arthur, T. S.; Allred, G. D.; Zajicek, J.; Newman, J. G.; Rodnyansky, A. E.; Oliver, A. G.; Boggess, W. C.; Muldoon, J. *Nat. Commun.* **2011**, *2*, 427−432.

[65] Bradwell, D. J.; Kim, H.; Sirk, A. H. C.; Sadoway, D. R. *J. Am. Chem. Soc.* **2012**, *134*, 1895−1897.

[66] Liu, Y.; Jiao, L.; Wu, Q.; Du, J.; Zhao, Y.; Si, Y.; Wang, Y.; Yuan, H. *J. Mater. Chem. A* **2013**, *1*, 5822−5826.

[67] Doe, R. E.; Mueller, T. K.; Ceder, G.; Barker, J.; Persson, K. A. U.S. Patent 2012/0219856, 2012.

[68] Rasul, S.; Suzuki, S.; Yamaguchi, S.; Miyayama, M. *Electrochim. Acta* **2013**, *110*, 247−252.

[69] Zhang, R.; Yu, X.; Nam, K.-W.; Ling, C.; Arthur, T. S.; Song, W.; Knapp, A. M.; Ehrlich, S. N.; Yang, X.-Q.; Matsui, M. *Electrochem. Commun.* **2012**, *23*, 110−113.

[70] Novák, P.; Desilvestro, J. *J. Electrochem. Soc.* **1993**, *140*, 140−144.

[71] Chernova, N. A.; Roppolo, M.; Dillon, A. C.; Whittingham, M. S. *J. Mater. Chem.* **2009**, *19*, 2526−2552.

[72] Delmas, C.; Cognac-Auradou, H.; Cocciantelli, J. M.; Ménétrier, M.; Doumerc, J. P. *Solid State Ionics* **1994**, *69*, 257−264.

[73] Murphy, D. W.; Christian, P. A. *Science* **1979**, *205*, 651−656.

[74] Yu, L.; Zhang, X. *J. Colloid Interface Sci.* **2004**, *278*, 160−165.

[75] Le, D. B.; Passerini, S.; Coustier, F.; Guo, J.; Soderstrom, T.; Owens, B. B.; Smyrl, W. H. *Chem. Mater.* **1998**, *10*, 682−684.

[76] Novák, P.; Scheifele, W.; Joho, F.; Hass, O. *J. Electrochem. Soc.* **1995**, *142*, 2544−2550.

[77] Amatucci, G. G.; Badway, F.; Singhal, A.; Beaudoin, B.; Skandan, G.; Bowmer, T.; Plitz, I.; Pereira, N.; Chapman, T.; Jaworski, R. *J. Electrochem. Soc.* **2001**, *148*, A940−A950.

[78] Imamura, D.; Miyayama, M. *Solid State Ionics* **2003**, *161*, 173−180.

[79] Imamura, D.; Miyayama, M.; Hibino, M.; Kudo, T. *J. Electrochem. Soc.* **2003**, *150*, A753−A758.

[80] Jiao, L.; Yuan, H.; Wang, Y.; Cao, J.; Wang, Y. *Electrochem. Commun.* **2005**, *7*, 431−436.

[81] Fiordiponti, P.; Pasquali, M.; Pistoia, G.; Rodante, F. *J. Power Sources* **1982**, *7*, 133−143.

[82] Robb, F. Y.; Glaunsinger, W. S. *J. Solid State Chem.* **1979**, *30*, 171−181.

[83] Uchiyama, M.; Slane, S.; Plichta, E.; Salomon, M. *J. Electrochem. Soc*. **1989**, *136*, 36−42.

[84] Jiao, L.-F.; Yuan, H.-T.; Si, Y.-C.; Wang, Y.-J.; Wang, Y.-M. *Electrochem. Commun.* **2006**, *8*, 1041−1044.

[85] Sadakane, M.; Ohmura, S.; Kodato, K.; Fujisawa, T.; Kato, K.; Shimidzu, K.; Murayama, T.; Ueda, W. *Chem. Commun*. **2011**, *47*, 10812−10814.

[86] Sadakane, M.; Kodato, K.; Kuranishi, T.; Nodasaka, Y.; Sugawara, K.; Sakaguchi, N.; Nagai, T.; Matsui, Y.; Ueda, W. *Angew. Chem., Int. Ed*. **2008**, *47*, 2493−2496.

[87] Holmberg, J.; Grasseli, R. K.; Andersson, A. *Appl. Catal. A* **2004**, *270*, 121−134.

[88] Vitry, A.; Morikawa, Y.; Dubois, J. L.; Ueda, W. *Appl. Catal. A* **2003**, *251*, 411−424.

[89] Watanabe, N.; Ueda, W. *Ind. Eng. Chem. Res*. **2006**, *45*, 607−614.

[90] Ishikawa, S.; Murayama, T.; Ohmura, S.; Sadakane, M.; Ueda, W. *Chem. Mater*. **2013**, *25*, 2211−2219.

[91] Pyrz, W. D.; Blom, D. A.; Shiju, N. R.; Guliants, V. V.; Vogt, T.; Buttrey, D. J. *J. Phys. Chem. C* **2008**, *112*, 10043−10049.

[92] Murayama, H.; Vitry, D.; Ueda, W.; Fuchs, G.; Anne, M.; Dubois, J. L. *Appl. Catal. A* **2007**, *318*, 137−142.

[93] Li, X.; Buttrey, D. J.; Blom, D. A.; Vogt, T. *Top. Catal*. **2011**, *54*, 614−626.

[94] Kaveevivitchai, W.; Jacobson, A. J. *Chem. Mater*. **2013**, *25*, 2708−2715.

[95] Bruce, P. G.; Krok, F.; Nowinski, J.; Gibson, V. C.; Tavakkoli, K. *J. Mater. Chem.* **1991**, *1*, 705−706.

[96] Bruce, P. G.; Krok, F.; Lightfoot, P.; Nowinski, J. L. *Solid State Ionics* **1992**, *53*, 351−355.

[97] Shimamura, O.; Yoshimoto, N.; Matsumoto, M.; Egashia, M.; Morita, M. *J. Power Sources* **2011**, *196*, 1586−1588.

[98] Tran, T. T.; Lamanna, W. M.; Obrovac, M. N. *J. Electrochem. Soc*. **2012**, *12*, A2005−A2009.

[99] Sathiya, M.; Ramesha, K.; Rousse, G.; Foix, D.; Gonbeau, D.; Prakash, A. S.; Doublet, M. L.; Hemalatha, K.; Tarascon, J.-M. *Chem. Mater*. **2013**, *25*, 1121−1131.

Chapter 7

Conclusions

In recent years, remarkable research progress has been made on solid state compounds, particularly regarding redox chemistry, which involves the transfer of electrons, and their electrical properties. This is due to the direct relation to the electronic conductivity of materials in our daily life and applications in electrochemical energy storage.[1–10] As the world is now facing environmental issues and an energy crisis, energy storage becomes more important today than ever. Alternative renewable energy sources and sustainable electric vehicles require large-scale energy storage systems.[11–15] As new solid compounds are continually discovered and novel promising properties are explored, the advances in the field are likely to continue to grow. This dissertation is focused on the exploitation of porous features of solid state compounds in particular, metal-organic frameworks (MOFs) and a microporous mixed transition metal oxide, with the ultimate goal to explore their potential electrochemical properties for applications in lithium and magnesium rechargeable batteries.

We describe in Chapter 2 an example of vapor-phase redox intercalation using vanadium benzenedicarboxylate, $[V^{IV}(O)(bdc)]$ (**2**), as the host and an electroactive organic compound, hydroquinone, as the guest under ambient and inert conditions. In ambient atmosphere, a quinhydrone charge-transfer complex formed inside the channels of **2** with the reduction of V^{IV} to V^{III}, $[V^{III}(OH)(bdc)]\cdot\{(O\text{-}C_6H_4\text{-}O)(HO\text{-}C_6H_4\text{-}OH)\}_{0.76}\cdot(H_2O)_{0.48}$ (**3**). Under anhydrous conditions, the framework of **2** itself was found

to be functionalized by *p*-semiquinone radical anion, a radical species formed by thermal decomposition of hydroquinone, as V^{IV} was reduced to V^{III}, $[V^{III}(O\text{-}C_6H_4\text{-}O)(bdc)]$ (**4**), with water as the byproduct. The single crystal products were either intercalated or functionalized by the guest organic molecule depending on the reaction temperatures and especially on the presence/absence of atmospheric moisture. Compound **2** is found to be stable and able to maintain its structure, even though changes in the redox state of the metal ions are involved, which is usually not the case for many reported MOFs.[16,17] This feature of the vanadium-based MOF is significant, as it may be able to undergo intercalation with other redox guest species. The redox properties of other vanadium systems may be examined in future studies.

A particular problem encountered during the synthesis was the crystal quality of **3** and **4**, especially for single crystal X-ray diffraction. This is mainly due to the activation process used on the as-synthesized solid, $[V^{IV}(O)(bdc)](H_2bdc)_{0.71}$ (**1**), to form the empty framework of **2**, which involved heating the crystals at high temperatures for an extended period of time. If a synthetic route that directly yields an empty structure of **2** can be developed, it will significantly improve the quality of the product after a post-synthetic modification, and open up a wide range of possibilities for functional guest intercalation.

One way to fine tune the properties of MOFs is to incorporate functional guest molecules inside the pores of the network.[18] In this research, we demonstrate a proof-of-concept that by incorporating the quinhydrone in **3**, an intermolecular proton-electron transfer reaction of the quinhydrone can occur together with the conductivity

along the ···OH −V− OH −V−··· chain of the host framework, which affects the charge transport properties and leads to interesting electrical properties of the material. This has been confirmed by conductivity measurements, even though it is not the scope of this dissertation.

In addition to the structural flexibility of **2** in response to the loading of the guest species, structural deformations as a function of temperature of the pristine phase **2** are also discussed in comparison with those of the functionalized product **4**. They show the opposite trends. This is possibly due to a combination of the oxidation state of the metal ions and the effect of the additional functional group. The understanding of this phenomenon could be useful in applications, such as advanced adsorbents and sensors.[19–22]

Due to the structural stability during the redox processes observed, the same vanadium MOF, [V(O)(bdc)] (**2**), was used in solid state electrochemical reaction with lithium (Chapter 3). V(O)(bdc) as the cathode material can be reversibly cycled in Li batteries with good rate capability and specific capacity. This is in contrast to the isostructural Fe-based compound (MIL-53) and deserves attention.[23] More investigation should be performed in order to further understand the mechanism involved and improve the electrochemical capacity. The cell performances and electrochemical profiles at various current conditions are discussed. Structural evolution associated with the electrochemical lithiation has been characterized.

During the electrochemical intercalation of lithium into a host structure, which involves Li^+ ion insertion and a transfer of charge-compensating electrons, the addition of electrons into the electronic band of the host generates strong electron-electron repulsions within the transition metal (TM) 3d orbitals, resulting in the destabilization in energy. To compensate for this, the system may either undergo a phase transition by stabilizing the transition metal into a different local environment (coordination geometry), or adopt a TM→O back-donation mechanism to release the extra charge toward the surrounding ligands.[24–26] The electrochemical capacity of V(O)(bdc) may be improved by using the second approach. The 1,4-benzenedicarboxylate (bdc) is a π-acceptor ligand.[24] An appropriate ligand functionalization, which is possible as evidenced by many MOF reports,[27] may be able to strengthen the inorganic-organic interactions and stabilize the V–O bonds, thus increasing the TM→O back-donation mechanism.[26] Host frameworks based on other transition metal ions may be worth investigating, as this may lead to interesting electrochemical properties due to the nature of the metal. The capacity may also be increased by taking advantage of the large open channels in V(O)(bdc) and inserting electrochemically active organic molecules into the pores.

In Chapter 4, we show that another metal-organic framework based on iron cations and formate organic linkers, $[NH_2(CH_3)_2][Fe^{III}Fe^{II}(HCOO)_6]$ (**FeFOR**), is also capable of acting as cathode material in secondary lithium batteries. The electrochemical performances suggest that **FeFOR** reacts reversibly with Li. A possible mechanism of the electrochemical reaction of **FeFOR** with Li is proposed, and believed to take place with a combination of intercalation and conversion processes with LiHCOO being the matrix

involved, unlike the case of V(O)(bdc) in Chapter 3. A thorough investigation of the reaction mechanism and phase transformation should be made in order to fully understand cathodic reaction of **FeFOR**.

A porous mixed transition metal oxide based on molybdenum and vanadium with large open 1D channels, $Mo_{2.5+y}VO_{9+\delta}$, was prepared, characterized, and used as an intercalation positive electrode material in lithium batteries (Chapter 5). $Mo_{2.5+y}VO_{9+\delta}$ has good electronic conductivity and can be reversibly cycled in an electrochemical cell with lithium as the counter electrode, at high current rates with excellent specific capacity of up to $x = 6$ in $Li_xMo_{2.5+y}VO_{9+\delta}$ with only 2% increase in unit cell volume. The electrochemical profiles show good rechargeability with and without conducting additives. The structural changes associated with Li-ion insertion by a chemical route are described, and the chemical deintercalation of lithium is also included to demonstrate the reversibility. The unique features of this oxide compound in terms of mixed occupation of crystallographic sites (Mo and V cations) and variation of local oxygen environments, together with the large open channels are believed to be responsible for the superior electrochemical properties. In the context of future work, modification of the basic framework in terms of composition and structure could lead to an improved electrochemical performance. A mechanistic study may also be useful in order to understand the reactions involved during Li insertion.

We show in Chapter 6 that the mixed Mo-V oxide, $Mo_{2.5+y}VO_{9+\delta}$, is able to reversibly undergo not only lithium insertion in Li-based batteries, but also magnesium intercalation with promising applications in Mg rechargeable batteries. $Mo_{2.5+y}VO_{9+\delta}$ can be reversibly cycled with magnesium as the counter electrode with good specific capacity. The effect of varying current densities on the discharge profiles is included along with the cyclability data. Unit cell dimensions of magnesiated phases prepared by a chemical reaction using a reducing agent were determined, and analyzed in comparison with the lithiated Mo-V compound. Despite the stronger interactions between the Mg^{2+} guest and ions of the host (compared to Li^{+} ions), which lower the cation mobility, the oxide can be used as intercalation electrode with good rate capability.[28–30] Presumably, this is due to the ability of the compound to effectively redistribute the divalent cation charge, and maintain local electroneutrality by electron delocalization within the $Mo_{2.5+y}VO_{9+\delta}$ framework, and especially the large open tunnels of this oxide which readily serve as solid state diffusion channels for the strongly polarized Mg^{2+} cations. If this is the case, designing an oxide compound with even larger channels together with mixed redox active transition metal ions may be a good strategy to overcome the limitations of multivalent cation diffusion, and this may pave the way for other oxide-based materials for the use as insertion electrodes in Mg rechargeable batteries.

The interest in using porous solid state compounds, the metal-organic frameworks and the microporous mixed transition metal oxide, in this research relies on an expected increase of the kinetics of the electroactive cation diffusion, which is one of the major limitations of dense electrodes. This has been well-proven through the electrochemical

investigations described above in both lithium and magnesium rechargeable batteries. Tuning the morphology or texture of an electrode material may well be another possibility to obtain porous and high-surface-area composite electrodes in order to enhance electrochemical capacities.

References

[1] Givaja, G.; Amo-Ochoa, P.; Gómez-García, C. J.; Zamora, F. *Chem. Soc. Rev.* **2012**, *41*, 115−147.

[2] Hendon, C. H.; Tiana, D.; Walsh, A. *Phys. Chem. Chem. Phys*. **2012**, *14*, 13120−13132.

[3] Li, S.-L.; Xu, Q. *Energy Environ. Sci.* **2013**, *6*, 1656−1683.

[4] Morozan, A.; Jaouen, F. *Energy Environ. Sci.* **2012**, *5*, 9269−9290.

[5] Allendorf, M. D.; Schwartzberg, A.; Stavila, V.; Talin, A. A. *Chem. Eur. J.* **2011**, *17*, 11372−11388.

[6] Choi, N.-S.; Chen, Z.; Freunberger, S. A.; Ji, X.; Sun, Y.-K.; Amine, K.; Yushin, G.; Nazar, L. F.; Cho, J.; Bruce, P. G. *Angew. Chem., Int. Ed.* **2012**, *51*, 9994−10024.

[7] Jeong, G.; Kim, Y.-U.; Kim, H.; Kim, Y.-J.; Sohn, H.-J. *Energy Environ. Sci.* **2011**, *4*, 1986−2002.

[8] Melot, B. C.; Tarascon, J.-M. *Acc. Chem. Res.* **2013**, *46*, 1226−1238.

[9] Dunn, B.; Kamath, H.; Tarascon, J.-M. *Science* **2011**, *334*, 928−935.

[10] Liu, C.; Li, F.; Ma, L.-P.; Cheng, H.-M. *Adv. Mater.* **2010**, *22*, E28−E62.

[11] Yuan, L.-X.; Wang, Z.-H.; Zhang, W.-X.; Hu, X.-L.; Chen, J.-T.; Huang, Y.-H.; Goodenough, J. B. *Energy Environ. Sci.* **2011**, *4*, 269−284.

[12] Wang, Y.; He, P.; Zhou, H. *Energy Environ. Sci.* **2011**, *4*, 805−817.

[13] Armand, M.; Tarascon, J.-M. *Nature* **2008**, *451*, 652−657.

[14] Wagner, F. T.; Lakshmanan, B.; Mathias, M. F. *J. Phys. Chem. Lett.* **2010**, *1*, 2204−2219.

[15] Poizot, P.; Dolhem, F. *Energy Environ. Sci.* **2003**, *4*, 2003−2019.

[16] Yanai, N.; Uemura, T.; Ohba, M.; Kadowaki, Y.; Maesato, M.; Takenaka, M.; Nishitsuji, S.; Hasegawa, H.; Kitagawa, S. *Angew. Chem., Int. Ed.* **2008**, *47*, 9883–9886.

[17] Meilikhov, M.; Yusenko, K.; Fischer, R. A. *J. Am. Chem. Soc*. **2009**, *131*, 9644–9645.

[18] Kim, H.; Chun, H.; Kim, G.-H.; Lee, H.-S.; Kim, K. *Chem. Commun*. **2006**, 2759–2761.

[19] Beauvais, L. G.; Shores, M. P.; Long, J. R. *J. Am. Chem. Soc*. **2000**, *122*, 2763–2772.

[20] Kepert, C. J. *Chem. Commun*. **2006**, 695–700.

[21] Albrecht, M.; Lutz, M.; Spek, A. L.; Koten, G. V. *Nature* **2000**, *406*, 970–974.

[22] Real, J. A.; Andrés, E.; Munoz, M. C.; Julve, M.; Granier, T.; Bousseksou, A.; Varret, F. *Science* **1995**, *268*, 265–267.

[23] Férey, G.; Millange, F.; Morcrette, M.; Serre, C.; Doublet, M. L.; Grenèche, J.-M.; Tarascon, J.-M. *Angew. Chem., Int. Ed.* **2007**, *46*, 3259−3263.

[24] Combelles, C.; Yahia, M. B.; Pedesseau, L.; Doublet, M.-L. *J. Power Sources* **2011**, *196*, 3426−3432.

[25] Combelles, C.; Doublet, M.-L. *Ionics* **2008**, *14*, 279−283.

[26] Combelles, C.; Yahia, M. B.; Pedesseau, L.; Doublet, M.-L. *J. Phys. Chem. C* **2010**, *114*, 9518−9527.

[27] Eddaoudi, M.; Kim, J.; Rosi, N.; Vodak, D.; Wachter, J.; O'Keeffe, M.; Yaghi, O. M. *Science* **2002**, 295, 469−472.

[28] Shterenberg, I.; Salama, M.; Gofer, Y.; Levi, E.; Aurbach, D. *MRS Bulletin* **2014**, *39*, 453−460.

[29] Levi, E.; Gofer, Y.; Aurbach, D. *Chem. Mater.* **2010**, *22*, 860−868.

[30] Levi, E.; Levi, M. D.; Chasid, O.; Aurbach, D. *J. Electroceram.* **2009**, *22*, 13−19.